PERMANENT MAGNET MACHINE TOPOLOGIES FOR HIGH SPEED FLYWHEELS

By: Gomezyani Mwaba

Thesis submitted to the Department of Electrical Engineering, University of Cape Town, in complete fulfilment of the requirements for the degree of Master of Science.

23 October 2009

DECLARATION

This dissertation is submitted to the Department of Electrical Engineering, University of Cape Town, in complete fulfilment of the requirements for the degree of Master of Science. It has not been submitted before for any degree or examination at this or any other university. The author confirms that this thesis is based on his own work. Portions of this work have been published in peer-reviewed journals and at refereed international conferences. The author confirms that he was the primary researcher in all instances where work described in this thesis was published under joint authorship.

"I know the meaning of plagiarism and declare that all the work in the document, save for that which is properly acknowledged, is my own".

_____

G. MWABA
23 October 2009

ACKNOWLEDGMENTS

First and foremost I would like to thank God and his son Jesus Christ for mercies and opportunities accorded to me in all facets of my life. I am grateful for the promise that a child of God needs only call to receive your blessings. I attest to many times during this journey that my call was answered. Thank you Lord.

Without family I am nothing. Their efforts and selflessness are truly not unappreciated. From the inspiration that is my father, David Brian Mwaba and the pillar that is my mother, Lasidah Mwaba to the support network my siblings continuously form around me, I am who I am through all of you. You provide a reason and help me achieve: to you profuse thanks.

Special Thanks go to my beloved fiancé Miss Mwanza Namwila. Your patience and kindness has seen me through the time I spent writing this thesis.

Thanks are due especially to my supervisor Dr. Azeem Khan. Your guidance and insight into this research work was indispensable. My thanks are also extended to Professor Pillay and Dr Marubini Manyage in this regard. I would like to add special mention to Richard Okou, Mr. Chris Wosniak, Mr Phillip Titus and my colleagues in the AMES group at the University of Cape Town.

I would also like to extend warm thanks to my house mates Daniel Minja and Teza Chila. Your support during the time I was writing this thesis has been humbling and I sincerely thank you.

To mention everyone who helped me would be impossible for I had the blessing of a lot of assistance. To all those I did not mention - I appreciate all the help

Many thanks.

Table of Contents

1 Introduction 1

1.1 Background 1

1.2 Literature Review 2

1.2.1 Development of flywheels 3

1.2.2 Induction Machines for High Speed Flywheels 4

1.2.3 Permanent Magnet Machines in High Speed applications 8

1.3 Research Questions and Objectives 13

1.4 Scope and Limitations 13

1.5 Structure 14

2 Comparison of PM Machine Topologies for High Speed Flywheels 15

2.1 Radial Flux Surface Mounted PM Machine 15

2.2 Halbach array machine 16

2.3 Double Rotor Single Stator Radial Flux PM Machines 20

2.4 Axial Flux PM Machines (AFPM) 22

3 Analytical and Numeric Modeling of PM machines for High Speed Flywheel 27

3.1 System Requirements and Overall System Topology 27

3.2 Analytical Model of a Radial Flux Halbach Array PM Machine 29

3.2.1 Flux Density 30

3.2.2 Excitation Voltage 32

3.2.3 Electromagnetic torque 33

3.2.4 Armature Resistance 33

3.3 Analytical Model of Axial Flux Brushless Machines 34

3.3.1 Excitation Voltage 34

3.3.2 Developed Torque 35
3.4 Radial flux Halbach Array Machine Loss Modeling 36
3.4.1 Copper losses 36
3.4.2 Windage losses 36
3.4.3 Winding eddy current loss 37
3.4.4 Friction losses 37
3.5 Axial flux PM Machine Loss Modeling 38
3.5.1 Copper losses 38
3.5.2 Windage losses 38
3.5.3 Winding eddy current loss 38
3.5.4 Friction losses 39
3.6 Thermal Modelling of High Speed PM Machines 39
3.6.1 Heat transfer by conduction 40
3.6.2 Heat transfer by convection 41
3.6.3 Heat transfer by radiation 41
3.6.4 Lumped parameter thermal network model 42
3.6.5 Calculation of thermal parameters 43
3.7 Finite Element Analysis 45
3.7.1 Finite element theory 46
3.7.2 Modeling of an axial flux machine 46
3.7.3 Air gap flux density 47
3.7.4 Flux linkage 48
3.7.5 Back EMF 48
3.7.6 Thermal modeling 49
4 Sizing and Detailed Design of Axial Flux BLDC Machine 51

4.1 Radial Flux Machine Sizing 52
4.2 Axial Flux Machine Sizing 53
4.3 Rotor Sizing 53
4.4 Stator Sizing 56
5 Prototyping of Axial Flux Machine 60
5.1 Construction of Rotor Disks 61
5.2 Stator Winding 63
5.3 Machining of the Shaft 67
5.4 Machine Containment Unit 68
5.5 Machine Assembly 70
6 Measurements and Testing of Axial Flux Machine 72
6.1 Machine Functionality Testing 73
6.1.1 Arrangement of stator coils 73
6.1.2 Open Circuit Voltage 75
6.1.3 Rotational losses 77
6.1.4 Output power 78
6.1.5 Efficiency 79
6.1.6 Temperature tests 80
6.2 Integrated System Functionality Testing 81
7 Conclusions and Recommendations 84
7.1 Conclusions 84
7.2 Recommendations 85
References 87
Appendix A 90

List of Figures

Figure 1.1: Main components of flywheel energy system. 3

Figure 1.2: Illustration of three phase induction machine. 5

Figure 1.3: Illustration of a surface mount radial flux PM machine [19]. 10

Figure 1.4: Illustration of axial flux machine [19]. 10

Figure 1.5: Interior magnet PM machine. 11

Figure 1.6: Buried rotor magnet PM machine. 12

Figure 2.1: Inner rotor radial flux machine [1]. 16

Figure 2.2: Magnetisation of segments. 17

Figure 2.3: Illustration of machine-flywheel integration. 17

Figure 2.4: Magnetic properties of the Halbach array 18

Figure 2.5: Magnetic properties of discrete magnet Halbach array. 19

Figure 2.6: Rotor and stator of a double rotor single stator radio flux machine. 21

Figure 2.7: Multiple disk axial flux machine [30]. 22

Figure 2.8: AFPM rotor disks. 23

Figure 2.9: Back emf and current waveforms of a brushless dc motor. 24

Figure 2.10: BLDC and BLAC performance comparisons relative to rated speed. 26

Figure 3.1: The system for which the flywheel energy storage is being designed. 27

Figure 3.2: Illustration of Halbach array machine 29

Figure 3.3: Flux density plots along contours at 1mm and 2mm from inner periphery. 32

Figure 3.4:Illustration of load line method. 35

Figure 3.5: Geometry of coreless axial flux machine for thermal modeling 42

Figure 3.6: Modeling of axial flux machine in 2D package. 47

Figure 3.7: Plot of airgap flux density from FEA package. 47

Figure 3.8: Plot of flux linkage from FEA package 48

Figure 3.9: Plot of back emf from FEA package. 49

Figure 3.10: Plot of temperature from FEA package and lumped parameter model. 50

Figure 4.1: Relationship of axial and radial flux machine dimensions. 51

Figure 4.2: Variation of shaft diameter with speed. 55

Figure 5.1: Polished rotor disks with retaining rings fitted. 61

Figure 5.2: Rotor disks with magnet retaining rings and epoxy. 63

Figure 5.3: Stator coils placed on spacers. 64

Figure 5.4: (a) square basin mould with spacers. (b) coils placed with thermocouples fitted (c) cast coreless stators (d) stators of 150W and 500W machines 66

Figure 5.5: Fabrication process and finished shaft of 150W machine. 67

Figure 5.6: (a) Main components of containment unit with flywheel in situ. (b) Cylindrical chamber with drilled access holes. (c) Cylindrical chamber with stator mounting 69

Figure 5.7: Assembly of 150W machine, with various designed components. 70

Figure 5.8: Complete system assembly. 71

Figure 6.1: Laboratory test setup for flywheel. 73

Figure 6.2: Arrangement of coils in one phase. 74

Figure 6.3: Equivalent phase resistance. 74

Figure 6.4: Open circuit voltage of individual coils. 75

Figure 6.5: Open circuit voltage of two phases of the machine. 76

Figure 6.6: Open circuit phase voltage Vs speed. 76

Figure 6.7: Open circuit line-line voltage Vs speed 77

Figure 6.8: Rotational loss versus speed. 78

Figure 6.9: Output power versus shaft speed 78

Figure 6.10: Efficiency versus load at different shaft speeds. 80

Figure 6.11: Temperature rise at rated current. 80

Figure 6.12: Variation of speed with time over a charge-discharge cycle. 81

Figure 6.13: Variation back emf with speed during the charge period. 82

Figure 6.14: Variation back emf with speed during the charge period. 82

Chapter 1

1 Introduction

1.1 Background

As renewable sources of energy such as solar and wind energy continue to penetrate the power industry, they are likely to become the more viable option to power rural areas. This is because extending existing electricity infrastructure to these areas would be expensive. However these forms of energy are intermittent and are therefore not always available when needed. Energy storage thus forms an integral part of such systems.

Several energy storage technologies have been developed in the recent decades. However, these technologies are associated with several problems. Lead acid batteries and wet cells are amongst the most widely used energy storage technologies. These technologies offer the advantage of being highly modular. They are also mature technologies with proven performance and excellent dynamic response. On the other hand, these technologies are characterised by high maintenance costs and short life spans. Their energy storage capacity deteriorates with the number of charge/discharge cycles and they are also significantly affected by temperature. For large installations, these technologies tend to have large foot prints thus occupying a considerable amount of space. Amongst increasing environmental concerns, there has been keen interest to move away from lead acid batteries and wet cells and develop environmentally friendly energy storage technologies. One such technology is the flywheel energy storage system. This technology offers the advantage of minimal environmental impact. The energy storage capacity of the flywheel is independent from the number of charge/discharge cycles. Flywheel energy storage systems also offer considerable space savings compared to lead acid batteries of similar capacity. They also have a longer life span and maintenance costs are minimal. The disadvantage of this technology is that it has high initial cost compared to lead acid batteries and wet cells. Flywheel energy storage systems are also characterised by shorter run times.

Flywheel technology is envisaged to provide a solution for energy storage for rural applications. Most existing flywheels are low speed and have been used for power applications where energy is drawn in very short periods of time. Their dependence on mass to store energy has made them bulky and less desirable for energy storage. It thus desired to design a high speed flywheel that

can be used for energy storage applications where the energy is drawn over relatively long periods of time. The advantage of high speed flywheels is the increased energy density since the stored energy is proportional to the square of its rotational speed. However these high speeds can only be achieved with careful selection and design of the motor/generator used to accelerate the flywheel. The design of high speed machines is a challenging task because there are several difficulties that the designer needs to overcome. These include:

- Increasing losses with speed
- High centrifugal forces
- Cooling of the machine

Permanent magnet machines are particularly advantageous for high speed applications since the excitation is provided by permanent magnets therefore eliminating excitation losses thus making the machine more efficient. This dissertation presents a systems approach to the sizing and design of a high speed permanent magnet machine for a high speed flywheel.

1.2 Literature Review

Flywheel energy storage systems are electro-mechanical batteries that store kinetic energy in a rotating mass. The amount of kinetic energy stored is a function of angular speed and the inertia of the flywheel, and is governed by equation 1.1.

$$KE = \frac{1}{2} J \omega^2 \qquad \textbf{(1.1)}$$

Where;

J is the flywheel moment of inertia in kg.m^2 and

ω is the angular speed in rad/s.

The three main components of the flywheel energy storage system are the flywheel, motor/generator and power electronic converter/inverter. Energy is transferred in and out of the flywheel using a machine that can operate as a motor or generator. In motor mode, electrical energy is supplied to the stator windings which develop a torque to spin the flywheel thereby causing it to gain kinetic energy. In generator mode, the kinetic energy of the flywheel is

converted to electrical energy. The rotating flywheel applies a torque to the rotor of the machine thus inducing voltages in the stator windings. The power electronic converter/inverter regulates the flow of power in and out of the machine and hence the flywheel energy storage system. Figure 1.1 illustrates the main components of the flywheel energy storage system.

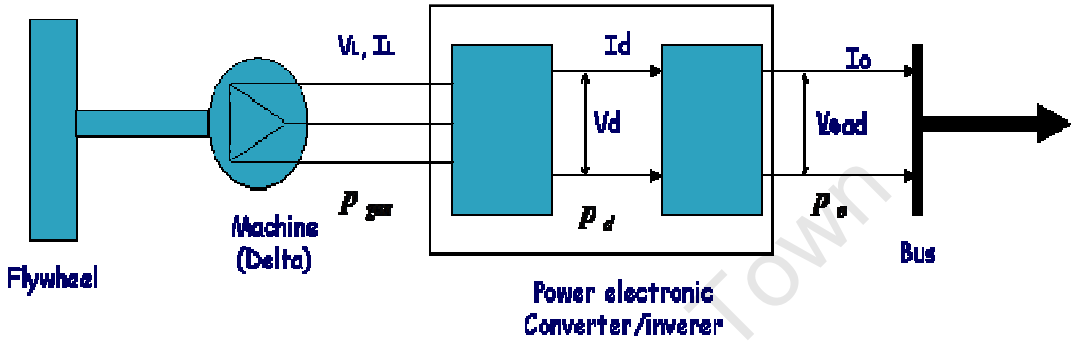

Figure 1.1: Main components of flywheel energy system.

1.2.1 Development of flywheels

Flywheel technology has been around for several hundred years. However, with advancements in other technologies such as electro-chemical batteries, flywheels became a less desirable choice for energy storage. This was because electrochemical batteries were highly modular as opposed flywheels that were bulky and very mechanical. Recent improvements in various technologies such as power electronics, magnetic bearings, composite materials and rare earth permanent magnets have resulted renewed interest in flywheel technology. Very high speeds can be achieved resulting in smaller and more compact flywheel systems. Flywheels are now considered a more competitive choice in renewable energy storage applications [1].

Dr. Stodola made the first significant break through in his seminal book where shapes and rotational stresses of flywheels were analysed [2]. Following this was the development of strong light-weight composite materials that saw flywheel technology being proposed by NASA as a primary source of energy in electric vehicles [3]. Today, all sub-components of the flywheel system can be designed to an equal level of complexity and integrated to form one system where electrical energy is fed in and retrieved on demand. Flywheels offer several advantages over other energy storage systems. In particular, the flywheel's energy storage capacity does not

deteriorate with the number of charge-discharge cycles. Power/energy densities of flywheels are considerably greater than those of other forms of energy storage, reaching over 5kW/kg [4]. Huge space savings can thus be realised by using flywheels as opposed to most electrochemical batteries. In addition, flywheels are also environmentally friendly since they do not produce toxic waste at the end of their life cycle.

The power industry made extensive use of traditional flywheels for power quality applications to ride through utility power interruptions. These first generation flywheels were made of steel and the amount of stored energy depended on the rotor inertia. These were simple low speed systems with simple controls to regulate power flow in and out of the flywheel energy storage system. In particular, as the amount of energy drawn was increased, the rotational speed of the flywheel decreased until the frequency was no longer acceptable. On the basis of their high inertia, they could only sustain large power demands for very short periods of time and were thus termed "power devices" [5]. Flywheels today are being designed to operate as energy devices that can sustain large power demand over long periods of time ranging from hours to days. This is achieved by designing for high speed operation. As can be seen from equation 1, the amount of energy stored by the flywheel is directly proportional to its inertia and the square of its angular speed. Doubling the rotational speed results in quadrupling the energy stored. Until recently, high speed operation was limited by absence of strong materials that could withstand the high stresses associated with the high speeds. This limitation has however been overcome with the development of strong light-weight composite materials. High speed flywheels can now be designed to be strong and compact which has resulted in a reduction of standby electric losses by as much as 90% as compared to their steel counterparts [6].

1.2.2 Induction Machines for High Speed Flywheels

The motor/generator used for high speed flywheels must be capable of reaching very high speeds typically in the range 10 000 – 100 000rpm. At such speeds, mechanical integrity and loss minimisation are very important considerations in the choice of machine and topology. Brushless machines are normally preferred in high speed applications due to their robustness. Induction and permanent magnet machines are common choices because of the absence of brushes, commutator segments and slip rings.

Induction machines are very widely used in industry. The application of these machines varies from small house hold appliances to large industrial pumps. For example they are used in blenders, refrigerators and washing machines etc where single phase machines are adequate. They are also used in pumps, compressors, paper mills and so forth where huge three phase machines are suitable. Although this machine topology can be used in both modes of operation i.e. as a motor or generator, the latter is seldom the case. In this machine topology, both the rotor and stator windings curry alternating currents. The stator winding is connected to the mains supply, directly or via a converter, while the rotor winding carries induced currents. Depending on the form of the rotor windings, induction machines can either be classified as squirrel cage or wound rotor induction machine. In squirrel cage machines, the rotor winding consists of copper or aluminium bars that are shorted at both ends. In a wound rotor machine, the rotor winding is distributed and takes the same form as the stator winding. Single and two phase induction machines and their applications are discussed in [7]. However, only three phase induction machines are discussed in this thesis, since it is the mostly widely used. Figure 1.2 illustrates the construction of a three phase induction machine.

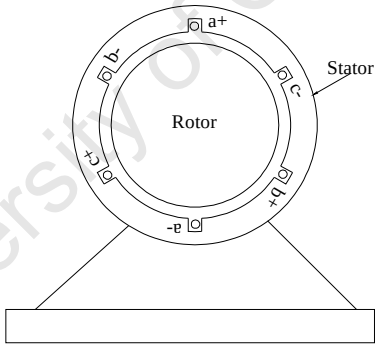

Figure 1.2: Illustration of three phase induction machine.

In three phase induction machines, an ac supply is connected to the stator windings that are displaced 120 electrical degrees in space. The result of the stator currents flowing through the phase windings is the establishment of a pulsating mmf along the axis of each of the phases. The net effect of the pulsating mmfs is a rotating mmf with constant magnitude as shown graphically and analytically in [8]. The rotating field in turn induces voltages and hence currents in the rotor windings. Similarly a rotating mmf is established due to the rotor winding currents. The interaction between the rotor and stator mmfs leads to the production of torque, thus causing the machine to rotate.

A major limitation in using induction motors for high speed applications is the weakness of its rotor structure. Induction machine rotors are normally laminated to reduce core losses. However, this makes the rotor weak and unable to withstand the large centrifugal forces due to the high speeds. Induction machines with solid rotor structures are investigated in [9]. The solid rotor is employed to counteract the centrifugal forces. However, careful dimensioning with respect to rotor diameter and length is necessary. This should be done in order to ensure that the operating frequency of the machine is below the critical frequency, and also to keep the tensile stresses below the maximum value that the rotor material can withstand. The maximum diameter of the rotor can be determined using equation 1.2 [10].

$$\sigma = k\rho\omega^2 r^2 \tag{1.2}$$

Where;

σ is the maximum tensile strength of the rotor material

k is the safety factor

ρ is density of the material

ω is the angular speed of the rotor

r is the radius of the rotor

Mechanically, the maximum length L of the rotor is limited by the critical frequency and is governed by equation 1.3 [10]

$$L^2 = n^2 \frac{\pi^2}{k\omega}\sqrt{\frac{EI}{\rho A}} \tag{1.3}$$

Where;

n is critical speed

k is the ratio of the critical angular speed to the nominal speed

E is the young modulus of the rotor material

I is the modulus of inertia

A is the cross sectional area of the rotor

A comparative study of induction machines with different rotor structures is carried out in [11]. Although solid rotor structures show superior mechanical properties to withstand large centrifugal forces, their electromagnetic performance is very poor. They operate at a poor slip

and have large core losses. Several methods of improving the electromagnetic properties are discussed in [11]. These include having a solid rotor coated with conducting material, a slit rotor with end rings and a slit rotor without end rings. However, implementation of these methods compromises the maximum tensile strength that the rotor can withstand.

In a study of thermal limitations and losses in induction machines, Saari [12] shows that a large part of the total losses is due to windage and friction losses. Depending on the design of the rotor structure, core losses can also form a significant part of the total losses. Windage losses are due to the flow of the gases on the rotating rotor surface and are proportional to the cube of the rotor speed. These losses can become very large in high speed applications such as high speed flywheel energy systems. Windage losses can be determined with reasonable accuracy using equation 1.4 [13].

$$P_w = \pi C_d \rho R^4 \omega^3 L \qquad \textbf{(1.4)}$$

Where

C_d is the drag coefficient

ρ is the density of the gas surrounding the rotor

R is the radius of the rotor

L is the axial length of the rotor

Windage losses can be minimised by operation with a vacuum. However, this is often an impractical solution since maintaining a vacuum requires auxiliary equipment such as pumps. In addition, vacuums exacerbate thermal effects since heat removal is limited to radiation alone. A more practical solution is to operate the machine in an enclosure with a helium-air mixture gas. With a 50% percent helium-air mixture, windage losses are reported to be reduced by 43% [14].

Friction losses in induction machines occur in the bearings. The choice of bearings for high speed applications has a huge impact on the amount of friction losses suffered by induction machines. The friction losses in a machine are dependant on the bearing coefficient, the mass of the rotor shaft and the rotational speed. These losses can be modelled using equation 1.5 [15].

$$P_f = 0.06 k_b (m_r + m_{sh}) n \qquad \textbf{(1.5)}$$

Where

K_b is the bearing coefficient

m_r is the mass of the rotor

m_{sh} is the mass of the shaft

n is the speed of the machine

Although bearings specifically designed for high speed applications exist, their performance in applications such as high speed flywheel applications is seldom satisfactory. An alternative is the use of magnetic bearings where there is no physical contact. The design of magnetic bearing systems for high speed applications is discussed in [16 -18].

Minimisation of no load losses such as friction, windage and core losses in flywheel systems is an important consideration because these losses determine the rundown time or rate of self-discharge of the flywheel energy storage system.

1.2.3 Permanent Magnet Machines in High Speed applications

Although PM machines have been used for many years as replacements for wound field excitation machines, they were, until recently, limited to low power applications. This was due to the low energy density of the available PM materials. The development of rare-earth materials such as NdFeB (Neodymium Iron Born) has resulted in the manufacture of high energy density magnets. Major advancements have also been made in the temperature characteristics of modern rare-earth PM materials. This, coupled with developments in power electronics, has given rise to a new generation of PM machines capable of delivering high power.

PM machines have distinct advantages that make them the dominant choice in high speed applications. The advantages of PM machines include:

- Higher efficiency (since excitation losses are absent)
- More compact structure
- Absence of commutator and brushes (less maintenance)
- Simpler construction

The main disadvantages of PM machines include:

- Demagnetising effect of the armature mmf
- The negative temperature coefficient of the remanence flux density of PMs

- High cost of PMs
- Complexity of controls circuitry

Several PM machine topologies exist which are usually classified as either axial or radial flux machines. The main components of the PM machines across the different topologies include a stator, rotor and magnets.

The stators of brushless PM machines normally consist of the stator laminations and the armature winding. The stator laminations are stamped from thin sheets of soft magnetic steel which are stacked together to form the stator core that completes the magnetic circuit. However, the presence of the stator core introduces core losses in the machine. In certain instances, the stator core is eliminated, especially in high speed applications where loss minimisation is critical. Such machines without stator cores are referred to as coreless machines. The stator winding is generally a three phase winding similar to that of induction machines. Each phase is distributed over several slots in cored machines or over the stator perimeter in coreless machines and is referred to as a distributed winding. In other PM machines, the phase windings are concentrated over a pole and these are referred to as concentrated windings.

Field excitation in PM machines is provided by the PMs mounted on the rotor. The absence of a field winding eliminates I^2R losses associated, thus making the machine more efficient. There are a number of methods used to mount PMs on the rotor, which result in varying characteristics of the machine. The first method is mounting the magnets on the surface of the rotor and these machines are thus referred to as surface mounted PM machines. In radial flux machines, the magnets are radially magnetised and the stator core provides the return path for the flux. Figure 1.3 illustrates the construction of a radial flux surface mounted PM machine.

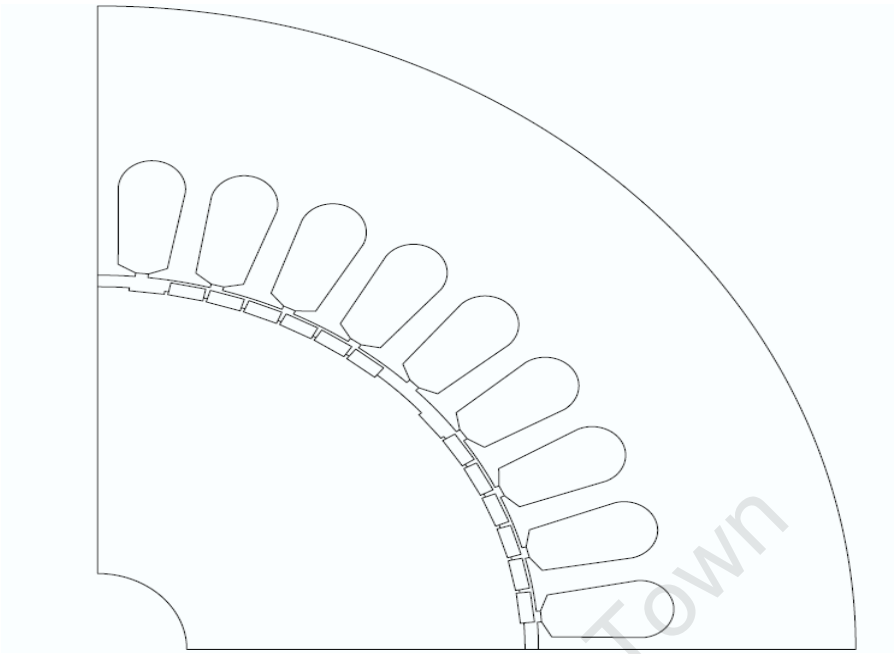

Figure 1.3: Illustration of a surface mount radial flux PM machine [19].

In axial flux machines, the magnets are magnetised in the axial direction and the flux path is normally confined to the rotor disks on which the magnets are mounted. Figure 1.4 shows an illustration of the axial flux PM machine.

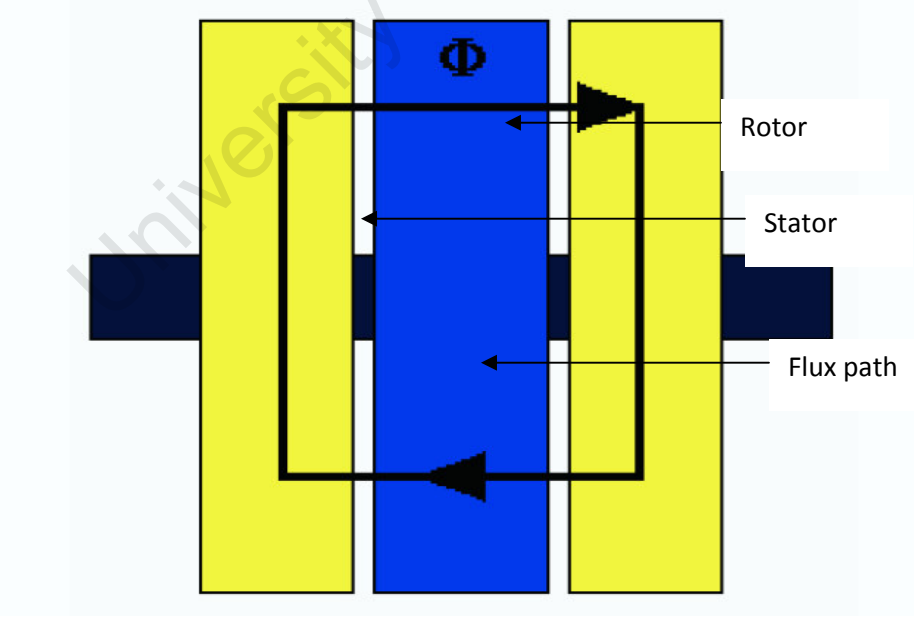

Figure 1.4: Illustration of axial flux machine [19].

Like in the radial flux machines, the PMs are fixed onto the rotor structure using adhesives and are exposed to the airgap. Rare earth PM Materials have approximately the same permeability as air. They therefore form part of the airgap magnetically and physically, and are consequently not protected from the demagnetisation effect due to the armature current. The exposure of the magnets makes them prone to damage mechanically, and the use of adhesives to fix them onto the rotor limits their use in high speed applications.

Another variation of the PM machine is the interior magnet rotor machine. The PMs are radially magnetised and are embedded in the rotor structure. Figure 1.5 shows the structure of an interior magnet rotor machine.

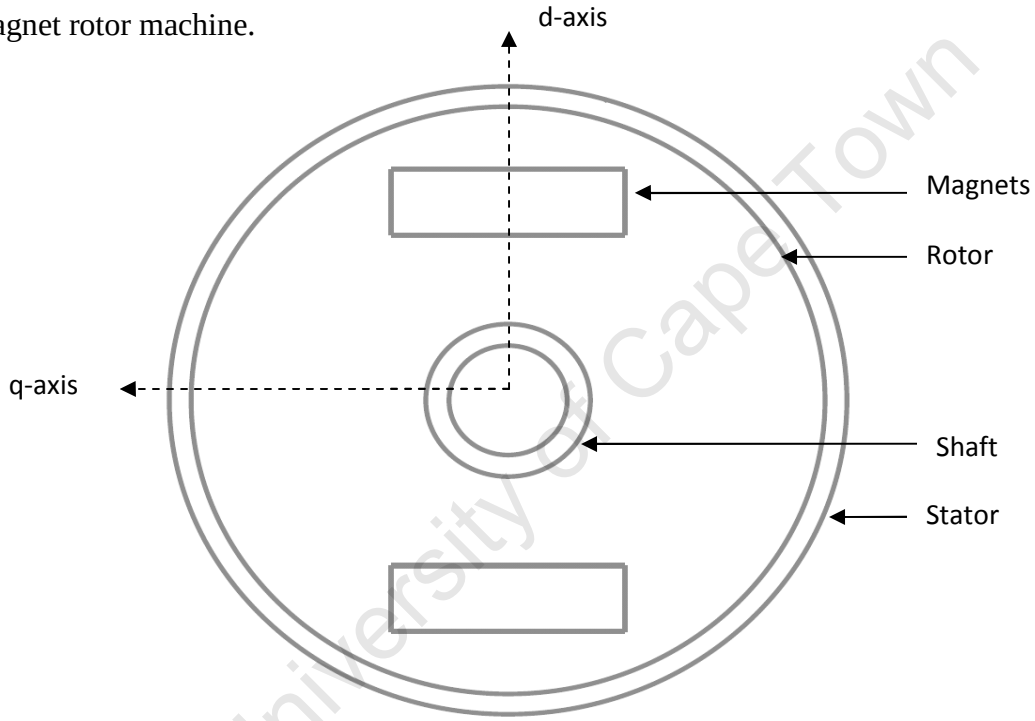

Figure 1.5: Interior magnet PM machine.

This type of PM machine is mechanically robust and can withstand high speeds. The magnets are less prone to damage since they are protected by the rotor structure surrounding them. They are also less exposed to the demagnetising effect of the armature current. Having the magnets located in the rotor structure significantly alters the electromagnetic properties of the machine. As can be seen from figure 1.5, magnetic flux along the d-axis of the machine experiences two additional airgaps since the permeability of the rare earth material is equal to that of air. A larger reluctance is thus experienced along the d-axis than the q-axis, hence introducing saliency into the rotor magnetic circuit. Although this type of machine is mechanically suitable for high speed

applications, the construction of the rotor is significantly more complex than that of surface mounted PM machines. They also produce more acoustic noise due to the quality of the torque wave form produced [21]. Although interior magnet axial flux machines exist, they are seldom comprehensively discussed in literature.

A third variation of PM machines is the buried magnet rotor machine. The PMs are magnetised in a circumferential direction and are embedded in slots formed by adjacent mild steel pole shoes. By combining and concentrating the flux, the two adjacent PMs are able to supply a large flux to the pole shoes. A non-ferromagnetic material is fitted between the ferromagnetic shaft and the pole shoes to minimise leakage through the steel shaft and ensure that most of the flux reaches the airgap. Figure 1.6 illustrates the construction of the buried magnet rotor machine.

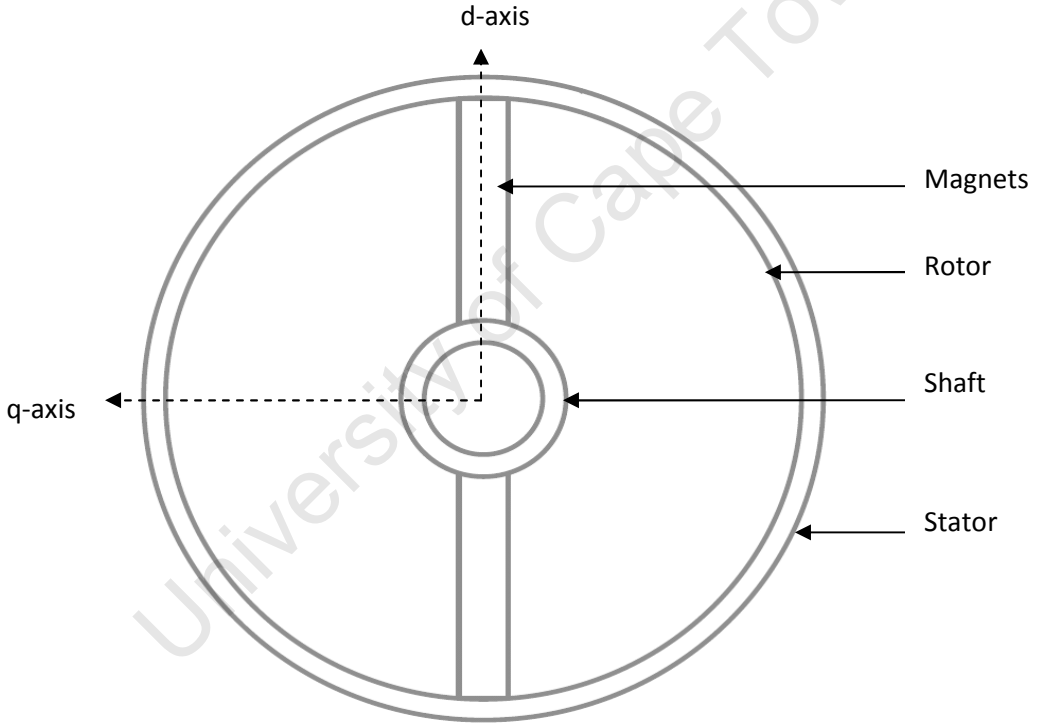

Figure 1.6: Buried rotor magnet PM machine.

The electromagnetic characteristics of the buried rotor machine are comparable to the interior magnet machine. The presence of the magnets inside the rotor introduces saliency in the magnetic circuit. Like the interior magnet rotor, it is mechanically robust. However the rotor construction is complex and the quality of its torque waveform causes acoustic noise in the machine [21].

1.3 Research Questions and Objectives

The main objective of this dissertation is to design and develop a permanent magnet machine for a high speed flywheel energy storage system.

This objective is achieved through detailed consideration of the following research questions associated with this dissertation:

- What PM machine topologies are suitable for high speed applications?
- Which PM machine topology is the best for low power, high speed flywheel applications with respect to cost, power/torque density, efficiency, ease of prototyping and control strategy?
- How can the machine be designed to give low back emf and sufficient torque to accelerate the flywheel to high speeds?
- What are the major losses associated with the design?
- What are the thermal implications associated with operating the machine in a vacuum?

The secondary objectives of this dissertation include:

- To analytically model the machine and the losses associated with it.
- To develop a thermal model for the machine.
- To design a machine with high structural integrity to withstand the high speeds.
- To minimise losses, thus increasing efficiency.

1.4 Scope and Limitations

Although this dissertation discusses a number of permanent magnet machine topologies, the design and prototyping is limited to an axial flux brushless dc machine. Two machines are designed and tested. The first machine is tested at low speed in order to ascertain the functionality of the design. The second machine is tested at high speed, fully integrated with the high speed flywheel.

Although the machine and flywheel rotor are designed to reach a maximum speed of 25, 000rpm, actual testing was carried out at lower speeds due to safety concerns.

1.5 Structure

The sizing of the machine is based on the requirements of the system and is discussed in chapter 2. The electromagnetic designs for three PM machine topologies are formulated in chapter 3. The models developed in chapter 3 are used to compare the performance of the three topologies. Thermal and loss models of the machine topologies are presented in chapter4. The design, prototyping and testing of an axial flux brushless dc machine is presented in chapter 5. The integration of the machine with a composite flywheel is discussed in chapter 6. Conclusions and recommendations are then presented in chapter 7.

Chapter 2

2 Comparison of PM Machine Topologies for High Speed Flywheels

This chapter discusses several PM machine topologies for use in high speed flywheel applications. Four PM machine topologies are compared in order to determine the most suitable topology for use in a high speed flywheel. These topologies include: an outer rotor radial flux Halbach array machine, a radial flux surface mounted machine, an axial flux machine and a double rotor single stator radial flux machine.

For the purpose of designing high speed flywheels, the criteria considered to be important are; efficiency, power density, torque density, ease of construction and maintenance and mechanical strength.

2.1 Radial Flux Surface Mounted PM Machine

Radial flux machines are extensively used for industrial applications and are commonly referred to as the "reference solution" [5]. Radial flux PM machine topologies have been used in applications ranging from ship propulsion to wind generators. Several variations of this topology can be realised depending on the structure of the stator windings, slots and magnet arrangement. The radial flux machine discussed in this thesis has an outer slotted stator and an internal rotor. The stator core is made from silicon steel to provide a magnetic flux path for the rotor magnets and stator mmf. The core is made of laminations that are stacked in order to reduce eddy current losses. The radially magnetised magnets can either be mounted on the surface of the rotor or buried in the rotor structure. Buried magnet rotors are preferred for high speed applications since they provide better magnet retention to withstand centrifugal forces. However, the construction of the rotor is quite complex. Buried magnets also suffer a lot of leakage flux due to the surrounding ferromagnetic material. Surface mounted PM machines are preferred due to their simple construction. Figure 2.1 illustrates the construction of a surface mounted radial flux machine.

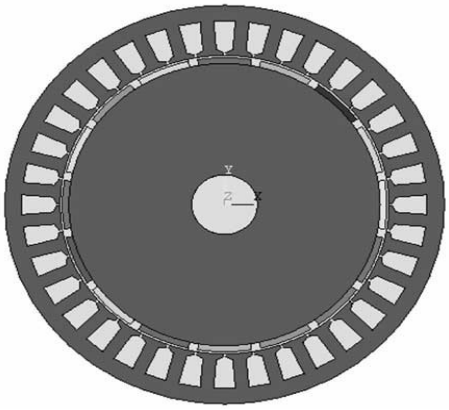

Figure 2.1: Inner rotor radial flux machine [1].

The main advantage of using this type of machine in high speed flywheel applications is that the flywheel and machine can be totally decoupled thus making fault diagnosis and assembly easy. However, studies carried out in [1], [2], and [5] show that the radial flux topology is not the best option where torque and power density are important factors. One of the major objectives in high speed flywheel design is to minimise the total system volume. It is therefore desirable to use machines with inherently high torque and power density values. A further disadvantage of the radial flux topology is its long end windings. This leads to an increase in the amount of copper thus leading to high specific copper losses. Other significant losses associated with this topology are core losses due to the presence of a stator core. The slots on the stator core also introduce cogging torque which increases the acoustic noise of the machine. Values of cogging torque for radial flux surface mounted PM machines are typically around 20% although this will vary slightly depending on the actual design [6]. The presence of core losses and cogging torque make the radial flux PM machine undesirable especially for high speed applications where high efficiency, power and torque densities are key objectives.

2.2 Halbach array machine

This machine topology is based on the work of Dr Klaus Halbach in 1979. He proposed a non-intuitive method of arranging permanent magnets to produce a uniform airgap flux density. In this machine topology, the rotor is made up of arc-shaped magnets magnetised in different directions to form a uniform multi-pole structure that is self screening. All the flux is therefore confined to the inside of the array and virtually no flux exists on the outside. The angle of magnetisation for the magnets is calculated using equation 2.1 [24].

$$\theta_m = (1+p)\theta_i \quad \textbf{(2.1)}$$

Where,

θ_m - angle of magnetisation,

p - number of pole pairs

θ_i - angle of the line through the centre of the ith magnet as shown in figure 2.1

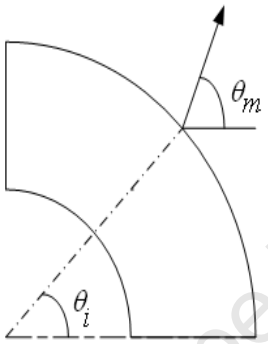

Figure 2.2: Magnetisation of segments.

Being an outer rotor machine, this topology is particularly desirable as it can be conveniently placed inside the flywheel which can, in turn, be mounted on magnetic bearings as illustrated in figure 2.3.

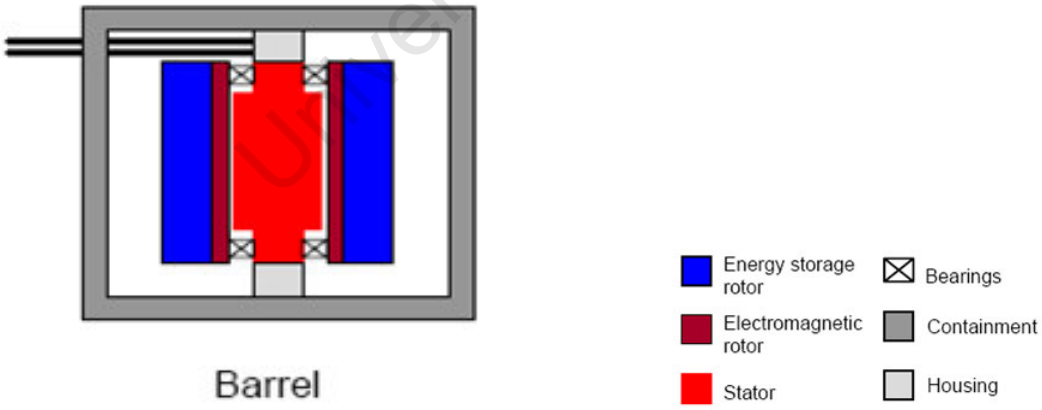

Figure 2.3: Illustration of machine-flywheel integration.

Another advantage of this machine type is that it has a coreless stator. Cogging torque and core losses are therefore totally eliminated thus resulting in a considerably more efficient machine.

Also, the uniform flux within the array makes it possible to have a near perfect sinusoidal air gap flux density waveform therefore reducing winding losses due to harmonics [3]. Figures 2.4a and 2.4b illustrate the self screening property of the Halbach array and the sinusoidal flux density waveform respectively.

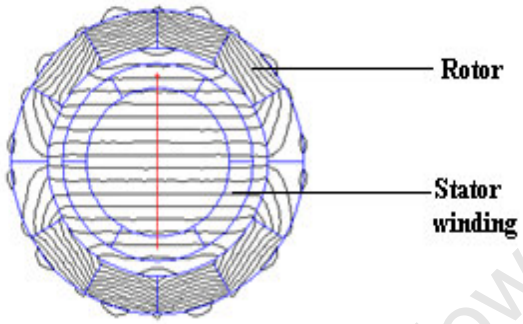

(a) Illustration of self screening property.

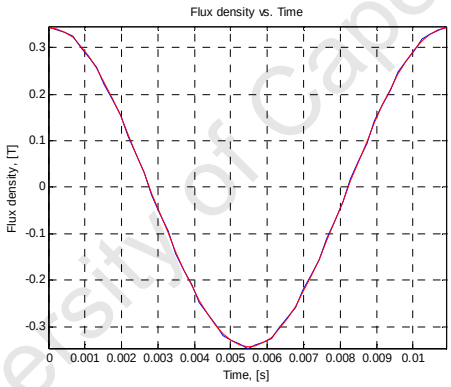

(b) Airgap flux density vs time.

Figure 2.4: Magnetic properties of the Halbach array

The main disadvantage of using arc-shaped magnets is that each segment has to be magnetised in it's own unique direction. The cost is thus raised since special magnets have to be ordered from manufacturers. A second variation of the halbach array machine topology uses square-shaped magnets. The magnets are physically orientated such that their magnetisation directions are given by equation 2.1. Figure 2.5a illustrates the square-shaped Halbach array.

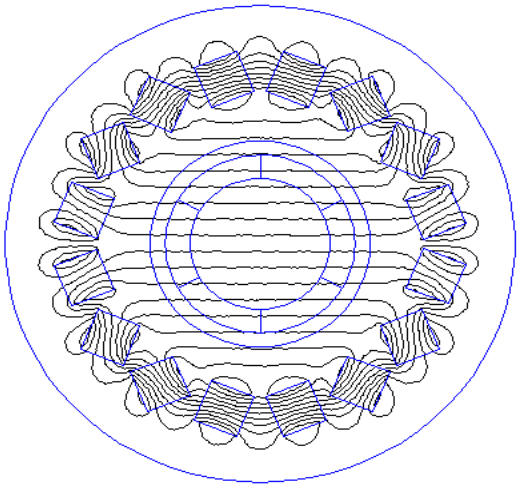

(a) Halbach array with square-shaped magnets.

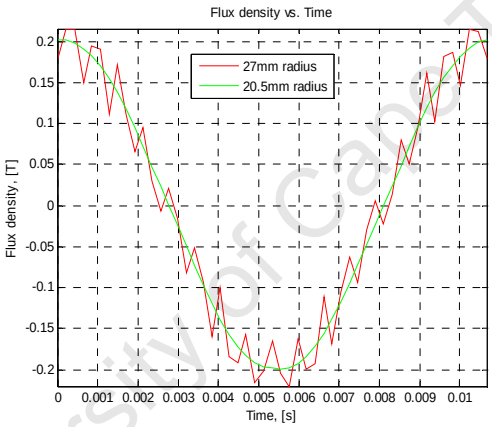

(b) Airgap flux density vs time.

Figure 2.5: Magnetic properties of discrete magnet Halbach array.

Using square-shaped PMs offers a number of advantages. Firstly the the magnets can be magnetised easily and in bulk. Secondly, standard off-shelf magnets can be obtained instead of ordering special magnets. This gives a further advantage of savings with respect to time and cost, thus making construction cheaper. The square-shaped Halbach array machine also has a number of disadvantages. There is increased ripple in the airgap flux density waveform as shown in figure 2.5b. The machine size is also increased since the magnets cannot fit as tightly together as in the arc-shaped halbach array machine. The minimum radius at which the magnets should be placed in order to ensure adequate inter-magnet clearance is given by equation 2.2.

$$r = \frac{d}{2\sin(\frac{\pi}{M})} + \frac{cM}{2\pi} \tag{2.2}$$

Where,

d is the diagonal of square magnet

M is the number of magnets

c is the clearance specified by designer

The increased size leads to decreased magnetic flux density for the same volume of magnets. To achieve similar flux densities as in the arc-shaped Halbach array machine, larger magnets are needed. However this increases the cost of the machine. The power/torque density of the machine is also decresed.

The Halbach array machine topology can result in very high efficiencies if the amount of copper in the stator is kept low. Large magnet volumes are thus required to give high flux densities which in turn raise the cost. Halbach array machines give low power and torque densities when compared to the other machine topologies,. The major drawback in integrating Halbach array machines with high speed flywheels is that fault diagnosis and assembly is a cumbersome task. This is due to limited access to the machine since it is placed inside the flywheel. Heat evacuation is also a big challenge especially if the flywheel is to be operated in a vacuum. Several methods for heat evacuation are suggested in literature such as the use of heat pipes [4]. However this complicates the system design even further.

2.3 Double Rotor Single Stator Radial Flux PM Machines

This machine is briefly described as having two machines nested inside one another [6]. The double rotor single stator machine topology has two rotor surfaces and a stator placed in between. The stator and rotor are placed on two different frames with the former on one end and the latter on the other. Figures 2.6a and 2.6b show the rotor and stator structures respectively for a double rotor single stator PM machine.

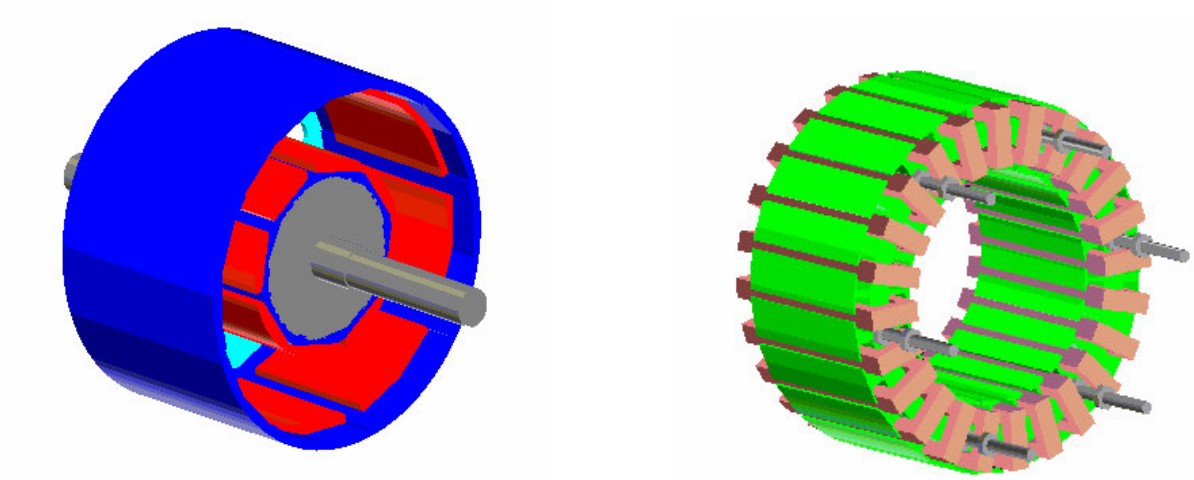

(a) Rotor structure. **(b)** Stator structure.

Figure 2.6: Rotor and stator of a double rotor single stator radio flux machine.

Depending on the magnet and winding configuration, this machine topology can be classified as either a toroidally wound or a lap wound machine. In the toroidally wound machine, the stator winding is wound toroidally on a stator core and the axial part of the winding is used for torque production. The outer magnets are magnetised radially inwards and the inner magnets are magnetised radially outwards or vice versa. The flux is thus driven in circumferential direction through the stator core. In the lap wound configuration, the winding is distributed on the stator core with the axial part being used for torque production. Both the inner and outer magnets are magnetised in the same direction. The magnetic flux is thus driven in a radial direction. The toroidally wound machine gives lower copper losses compared to the lap wound machine due to shorter end windings. The former is thus preferred in applications where high efficiencies are required such as in high speed flywheels.

The main advantage of this machine topology in high speed flywheel applications is that it can be totally decoupled from the flywheel. At the same time this machine topology gives high power/torque densities. An efficiency of 96% is reported in [7] for a toroidally wound double rotor single stator machine. As in the surface mounted radial flux machine, the double rotor single stator machine also suffers cogging torque and this is one of its major disadvantages in high speed applications. However, techniques such as slot opening shifting, varying PM angular width and varying slot angular width can be used to reduce cogging torque by as much as 50% [8]. Another disadvantage of the double rotor single stator topology is that optimisation is more

complex than other topologies. Because of the two air gaps of different radius, it has two electric loadings that need to be optimised.

2.4 Axial Flux PM Machines (AFPM)

Axial flux machines have the magnetic flux driven parallel to the shaft of the machine. Numerous variations of this machine topology can be achieved depending on the magnet configuration and stator-rotor configuration. Some of the variations include; multiple disks, double sided and single sided axial flux machines. The multiple disk axial flux machine has multiple rotors and stators as shown in figure 2.7.

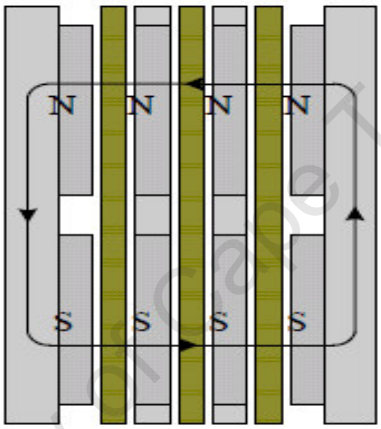

Figure 2.7: Multiple disk axial flux machine [30].

The multiple disk axial flux machine is mainly used for high power applications. For an application such as a high speed, low power flywheel, this machine would be an over design. A further disadvantage is that the total volume of the flywheel system is not minimised. The single sided axial flux machine has the simplest construction. It has one stator and one rotor disk. However, there are very strong attractive forces between the stator and rotor making it undesirable in high speed flywheel applications where balancing and mechanical integrity are important considerations. The double sided axial flux machine is the optimal machine to eliminate attractive force between the rotor and stator and to minimise total flywheel system volume.

Other variations can be obtained depending on whether the magnets are surface mounted or buried. In this thesis the double sided surface mounted axial flux PM machine is discussed. The machine has two rotor disks and an internal coreless stator placed between the two disks. It has

arc shaped magnets mounted in an N-S configuration on the rotor surfaces. Figure 2.8 shows the rotor disks of an axial flux machine.

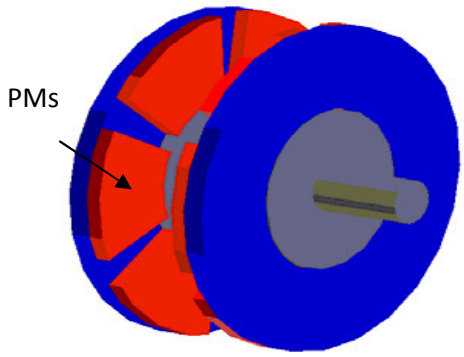

Figure 2.8: AFPM rotor disks.

Axial flux machines have a number of advantages over conventional radial flux machines especially in applications such as high speed flywheel applications. Firstly they have higher power/torque densities. Secondly axial flux PM machines have a more compact construction with a flat profile. Axial flux machines also give higher efficiencies. However, they have a more complicated construction because they have multiple air gaps.

The performance of the double sided axial flux machine is very similar to that of the double rotor single stator radial flux machine with respect to power density, torque density and efficiency [22]. This is due to their similarity in construction with both machines having two air gaps. The two topologies, however, differ in certain aspects such as cost, optimisation and ease of construction. The double rotor axial flux topology tends to require more magnets than the double rotor radial flux and is thus more expensive [2]. The latter also has a higher power loss per unit air gap area suggesting that it would need good cooling conditions [6].

From the comparisons made, the axial flux topology is favoured for the high speed flywheel application because it offers a good trade-off between space minimisation and torque/power output. Their flat profile makes it possible to minimise the total volume of the containment of the flywheel.

The axial flux machine can further be categorised as brushless dc (BLDC) or brushless ac (BLAC) depending on how the stator windings are configured and excited. Brushless dc machines have a trapezoidal distribution of flux in the airgap, concentrated stator windings and

they are excited by square current waveforms as shown in figure 2.9. The main advantage of BLDC machines is the production of an average torque with quasi-square wave currents flowing through the windings of a 3 phase machine. Also, the BLDC machine has a relatively high power density. However, a disadvantage of such machines is the need for rotor position sensing techniques by means of optical sensors or Hall Effect sensors. This in turn limits the drive and also affects its reliability and robustness. Rotor position can however be sensed by sensorless techniques, but this would be complex for high speed applications due to the high bandwidth control that would be required.

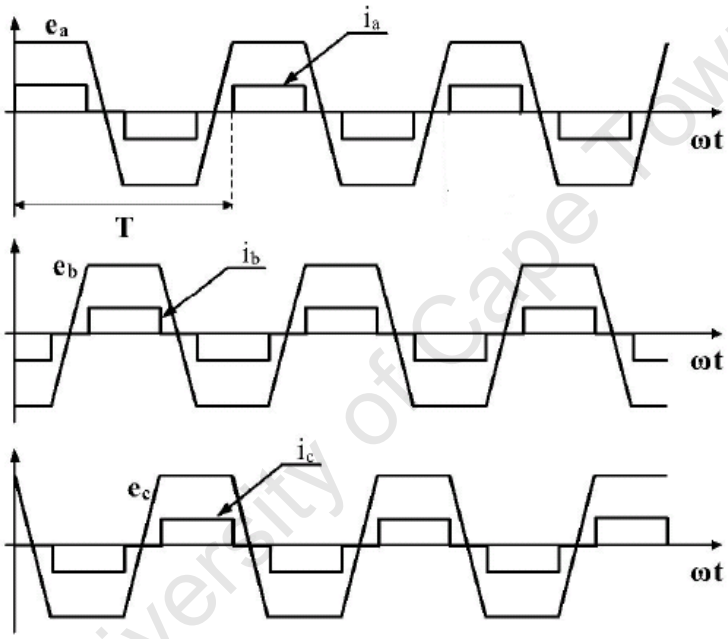

Figure 2.9: Back emf and current waveforms of a brushless dc motor.

Brushless ac machines have a sinusoidal flux density distribution in the airgap. The stator windings are normally distributed in order to obtain a sinusoidal back emf waveform. Excitation and torque production is achieved by injecting a sinusoidal current waveform into the stator winding. Brushless ac machines are normally preferred because there is no need for rotor position sensing.

A comparison of performance based on analytical equations given in chapter 3 of this thesis was performed. Both the BLDC and BLAC axial flux machines are designed to meet the requirements of the high speed flywheel in with respect to flux density, back emf and torque. The

comparison of the two variations of axial flux machines is based on torque/power density and mass of magnets used in the design. Figure 2.10(a-c) shows the performance of the two designs relative to the rated speed of the high speed machine.

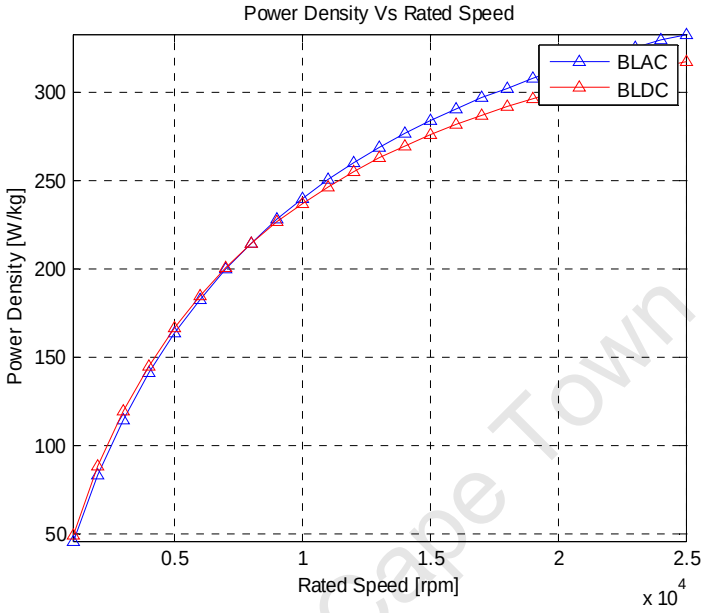

(a) Power density of BLDC and BLAC axial flux PM machine relative to rated speed.

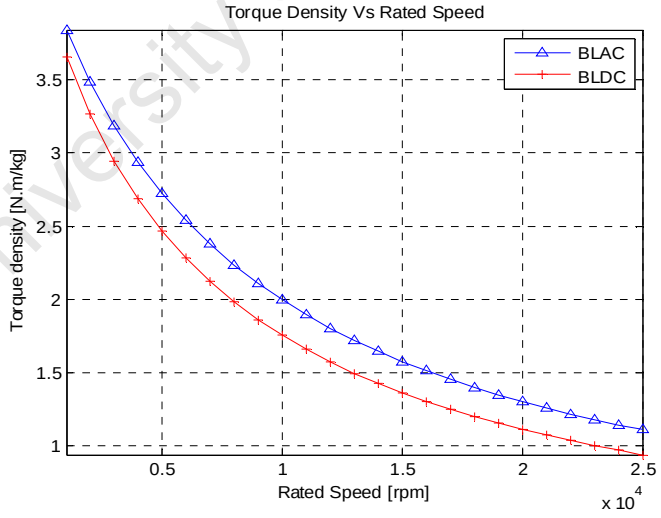

(b) Torque density of BLDC and BLAC axial flux PM machine relative to rated speed.

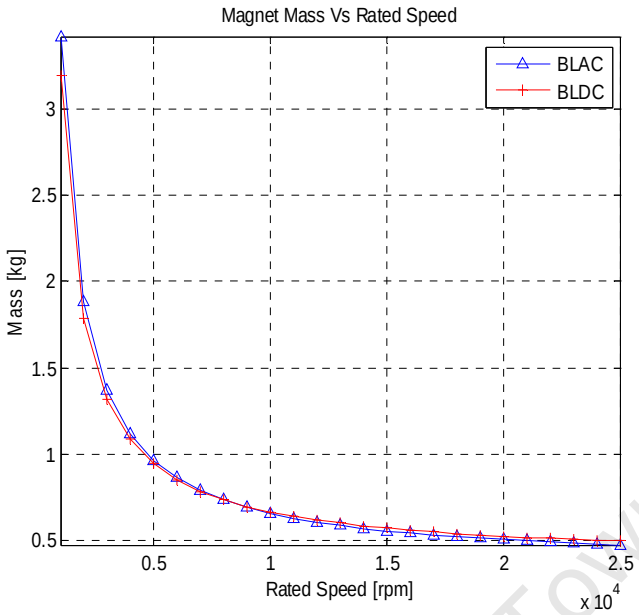

(c) Magnet mass of BLDC and BLAC axial flux PM machine relative to rated speed.

Figure 2.10: BLDC and BLAC performance comparisons relative to rated speed.

It can be seen from the figures that the BLAC design performs better than the BLDC design. Investigations carried out in [27] show that the BLAC is also more efficient that the BLDC. However, the differences in performance between the two are not significant. The choice between the two variations is thus normally influenced by further consideration of acoustic noise and simplicity of the control technique. In this thesis, the BLDC is chosen for design due to the simplicity of the drive.

Chapter 3

3 Analytical and Numeric Modeling of PM machines for High Speed Flywheel

This chapter presents the detailed analytical equations used for the consideration of three PM machines for integration with a high speed flywheel. These machines include; a radial flux Halbach array machine, axial flux brushless ac machine and an axial flux brushless dc machine. The final design of the machine for integration with the high speed flywheel is based on the requirements of the overall system including maximum power demand of the loads, bus voltage, energy storage requirement and speed of the flywheel. The system requirements and overall system topology for the flywheel system are discussed in section 3.1.

3.1 System Requirements and Overall System Topology

The flywheel is being designed as an energy storage component for a photo-voltaic (PV) system as shown in figure 3.1. This energy storage device will supply power to the load when the PV supply is unable to meet the demand. It will also store energy when excess power is available from the PV supply.

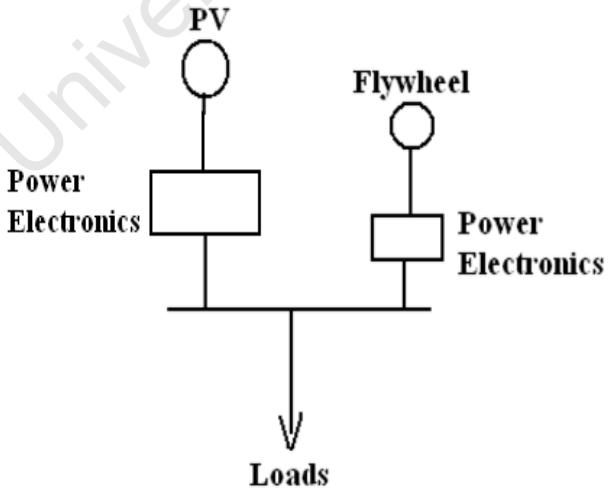

Figure 3.1: The system for which the flywheel energy storage is being designed.

It is assumed that the PV will supply useful power for 4 hours of the day. During this period, the flywheel energy storage should charge fully i.e. reach the rated rotational speed of 25000rpm. During the night when the PV can no longer meet the load demand, power is supplied from the flywheel energy storage system. The flywheel is sized and designed to store 600Wh of energy at rated speed.

All components of the system are referenced to the bus. The load in the system is a rural household with an estimated peak demand of 100W-150W to power lighting, a radio and a small black and white television set. From the system shown in figure 3.1, requirements such energy, power rating etc can be obtained and thus enable the machine to be sized.

Energy Requirement

The energy to be stored in the flywheel can be determined by integrating the household load profile over a defined period. In this case, the flywheel energy storage should sustain peak demand for 4 hours.

The energy obtained from the method above is only the load requirement. However, compensation needs to be made for self discharge of the flywheel energy storage. In order to avoid start up transients, the flywheel energy storage will not be discharged to zero speed. Therefore the flywheel should be sized to ensure that the required energy is supplied between the maximum and minimum speeds.

Power Rating

The power rating of the flywheel machine should be able to sustain the peak demand of the load (100W-150W). This rating should also take the losses into consideration i.e. the charging and discharging losses. The main charging/discharging losses include copper, windage and friction losses.

Voltage Rating

The voltage rating of the machine should be related to the bus voltage. This voltage should be achieved by the flywheel system the lowest speed determined by the depth of discharge of the

flywheel. The power electronic converter of the machine will be used to control the voltage swings over the entire speed range of the flywheel.

Specification for Flywheel

Based on the aforementioned requirements, the specifications for the flywheel energy system are as shown in table 3.1.

Table 3.1: The initial specifications of the flywheel energy storage system.

Energy [Wh]	600
Speed [rpm]	25000
Power [W]	100
DC Voltage [V]	12

3.2 Analytical Model of a Radial Flux Halbach Array PM Machine

In this section, the analytical model of a three phase outer rotor radial flux Halbach array machine is formulated. The machine considered is a two pole machine with a coreless stator. A coreless stator is preferred for high speed applications in order to eliminate core losses that are frequency dependant thus making the machine more efficient. The machine is slot-less and has a three phase winding. Figure 3.2 illustrates the construction of a Halbach array machine.

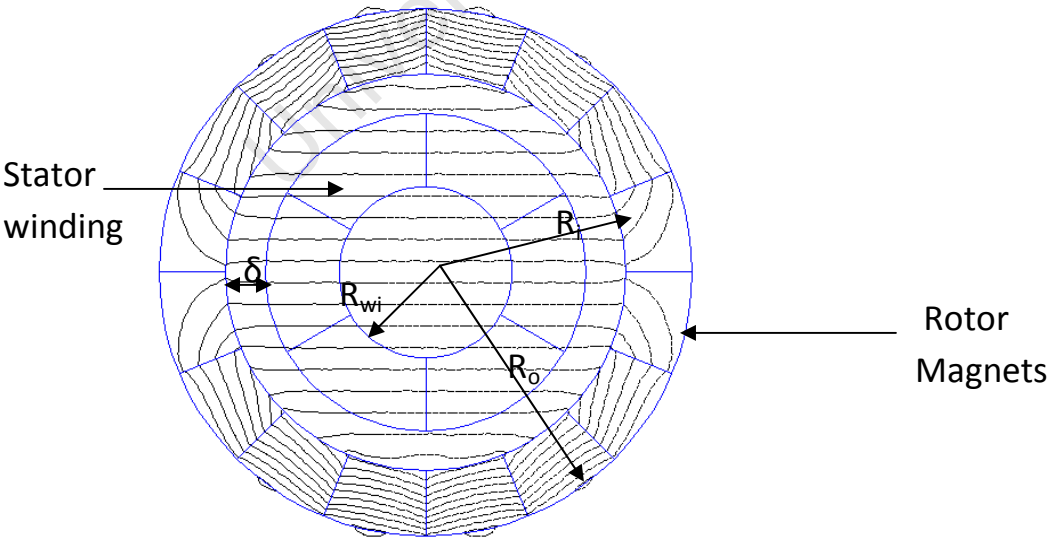

Figure 3.2: Illustration of Halbach array machine.

3.2.1 Flux Density

The peak flux density produced by the magnet arrangement in a Halbach array can be expressed as [31]:

$$B = B_r \ln(\frac{R_o}{Ri}) \frac{\sin(\frac{2\pi}{M})}{\frac{2\pi}{M}} \quad (3.1)$$

Where

B_r is the remanence flux density of the magnet segments

R_o and R_i are the outer and inner radius of the Halbach array respectively

M is the number of magnet segments.

The flux density waveform produced by the Halbach array becomes more uniform with increasing number of magnet segments. It can be seen from equation 3.1 that the peak flux density asymptotically approaches a constant value as the number of magnets segments tends to infinity. The magnitude of the flux density is determined by the remanent flux density of the PMs and the ratio of the inner to outer radius of the Halbach array. In machine design, the ratio of inner to outer radius that optimises voltage and torque production is 0.72. The outer rotor radius of a high speed machine can be determined by the maximum centrifugal forces that the rotor PMs and disks can withstand. This is dependant on the ultimate tensile strength and density of the material as well as the angular speed. The outer radius is thus determined by [32]:

$$R_o = \frac{1}{\omega}\sqrt{\frac{\sigma_u}{\rho}} \quad (3.2)$$

Where

σ_u is the ultimate tensile strength

ρ is the density of the material

ω is the rotational speed

When designing outer rotor machines it is desirable to place the stator windings as close as possible to the inner periphery of the magnets. This is in order to maximise torque and voltage production. However, for a finite number of discrete magnet segments, the ripple on the flux density waveform increases as you move closer to the inner periphery of the PMs thus increasing the torque ripple and eddy current losses in the stator winding. A trade-off between ripple and torque/voltage maximisation therefore has to be established. The effect of distance from inner periphery of the PMs on the flux density wave form is illustrated in figure 3.3. The plots show the normal components of the airgap flux density around contours which are 1mm and 2mm away from the inner periphery of the PMs.

The higher ripple is clearly evident in the flux density waveform closest to the inner periphery of the PMs.

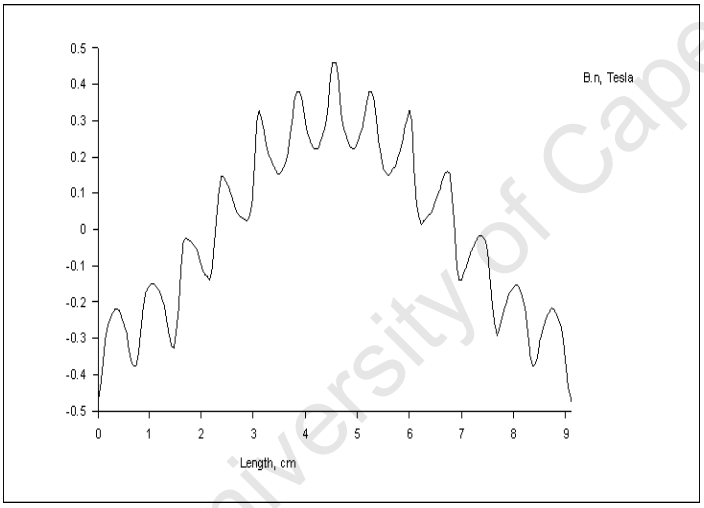

(a) Airgap flux density wave form along contour at 1mm from inner periphery.

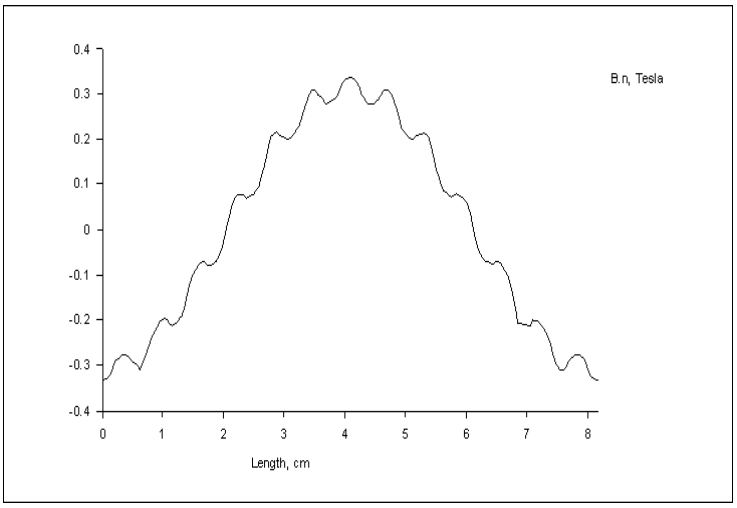

(b) Airgap flux density wave form along contour at 2mm from inner periphery.

Figure 3.3: Flux density plots along contours at 1mm and 2mm from inner periphery.

3.2.2 Excitation Voltage

The rms value of the fundamental component of the excitation voltage induced in a phase winding is given by equation 3.3 [33].

$$E = 4.44 f N_{ph} \Phi_p k_w \tag{3.3}$$

Where

f is the fundamental frequency

N_{ph} is the number of turns per phase

Φ_p is the average flux per pole

K_w is the winding factor

The average flux per pole can be expressed as

$$\Phi_p = 2B_{\max} L(R_i - \frac{\delta}{2}) \tag{3.4}$$

The number of turns per phase of the stator can be expressed as

$$N_{ph} = \frac{((R_i - \delta)^2 - R_{wi}^2)\pi \times k_f}{2m \times A_{cond}} \tag{3.5}$$

Where

R_i is the inner radius of the Halbach array

δ is the mechanical clearance between the Halbach array and the stator outer radius

R_{wi} is the inner radius of the stator

K_f is the fill factor

m is the number of phases

A_{cond} is the area of the conductor

3.2.3 Electromagnetic torque

The electromagnetic torque developed by the machine is obtained from the airgap power and the speed of the machine. It is also dependant on the load angle which is the angle between the magnetic field vector and the stator winding current vector. The model for the electromagnetic torque is given by [34]:

$$T = \frac{mEI}{\omega}\sin\delta \tag{3.6}$$

Where

E – rms back emf of the machine per phase

I – rms current per phase

ω – angular speed of the machine

δ – load angle

m is the number of phases

3.2.4 Armature Resistance

The stator per phase resistance is modelled by estimating the total length of the phase winding which can be expressed as [19]

$$l_{winding} = 2(l + l_{end})N_{ph} \tag{3.7}$$

Where

l – axial length of stator

l_{end} - length of end winding

The resistance of the phase winding can thus be represented as [19]

$$R_a = \frac{l_{winding}}{\rho A_{cond}} \tag{3.8}$$

3.3 Analytical Model of Axial Flux Brushless Machines

3.3.1 Excitation Voltage

References [35-37] give detail on the electromagnetic design of electrical machines. In [37] armature reaction is ignored in the model due to the large effective airgap which causes the stator mmf to experience a large reluctance.

The back emf of the machine is given by [37]:

$$E_{L-L} = k_e n \tag{3.9}$$

Where n is the speed and k_e is the armature constant given by [37]:

$$k_e = 8 p N_{ph} k_w \Phi \tag{3.10}$$

Using expressions 3.9 and 3.10, the required flux and flux density to produce a given voltage can be determined.

In sizing the magnets, adequate margin against demagnetisation is provided by choosing the permeance coefficient to be at least 6 [19]. An operating point is thus obtained from the magnet B-H curve using the load line method as illustrated in figure 3.4.

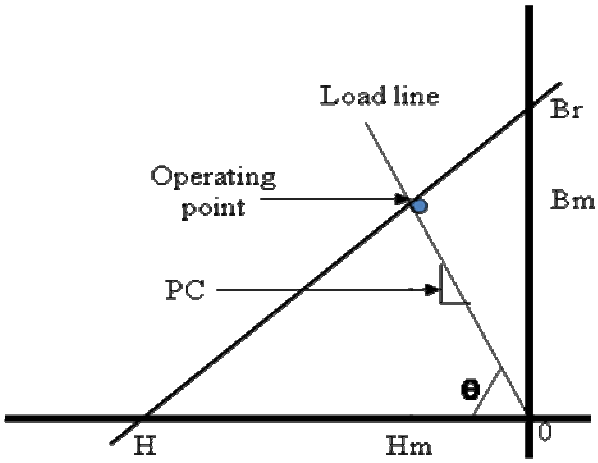

Figure 3.4: Illustration of load line method.

Assuming negligible fringing of the magnetic flux, the length of the magnets in the axial direction and the thickness of the back iron are given by [15]

$$l_m = \frac{A_g B_g}{2B_m} \tag{3.18}$$

$$l_y = \frac{A_m B_m}{2B_{\max} l_i} \tag{3.19}$$

Where A_m, A_g, B_m and B_g are the magnet area, airgap area, magnet flux density and airgap flux density respectively, and l_i is the length of the coils in the radial direction.

3.3.2 Developed Torque

The torque developed by the axial flux machine can be expressed as [37];

$$T_d = \frac{\pi}{2} k_D . k_w D_o^3 B_g A \tag{3.20}$$

Where

k_D is a function of the ratio of the outer to inner diameter of the stator

k_w is the winding factor

D_o is the outer diameter of the stator

B_g is the airgap flux density

A is the electric loading of the machine

3.4 Radial flux Halbach Array Machine Loss Modeling

Although the absence of a core totally eliminates core losses in Halbach array machines, other losses such as windage and copper losses are still present. These losses in Halbach array machines can be modeled as analytical equations and are discussed in this section.

3.4.1 Copper losses

Copper losses are incurred during load conditions and are expressed as.

$$P_{cu} = 3I^2R \tag{3.21}$$

Where

I is the rms current per phase

R is the stator resistance per phase

Temperature correction of the stator resistance is provided using equation 3.22 [12]

$$R_T = R_{20}[1 + 0.00393(T - T_{20})] \tag{3.22}$$

Where

R_{20} is the resistance at 20°C

T is the temperature of the resistance measurement

3.4.2 Windage losses

As the machine rotates, there are frictional forces between the rotor and the air surrounding it. These losses become more prominent as the speed of the machine increases. The derivation of the model for these losses is based on the fact that in gases, the shear stress is proportional to the rate of change of shear strain. Windage losses can be expressed as [38]:

$$P_w = 2(D - 2l_g)^3 l(\frac{60f}{p})^3 10^{-6} \tag{3.23}$$

Where

D is the rotor diameter

l_g is the air gap length

l is the axial length of the machine

f is the frequency

p is the number of poles

3.4.3 Winding eddy current loss

Due to the high speed of the machine, there is rapid variation of the flux within the stator windings causing eddy currents to develop. A finite element aided model is used to predict winding eddy current losses [39]. This incorporates the static equation with flux densities obtained from finite element simulations and is expressed as:

$$P_e = \frac{\pi^2 \sigma}{4\rho} f^2 d^2 m_{con} [B_{mx}^2 + B_{my}^2] \eta_d^2 \tag{3.24}$$

Where

σ is the conductivity of the winding material

ρ is the density of the winding material

f is the frequency

d is the diameter of the conductor

m_{con} is the mass of the conductor

B_{mx} and B_{my} are the peak x and y components of of the flux density

The harmonic factor η_d is expressed as [39]:

$$\eta_d = \sqrt{1 + \frac{(3B_x)^2 + (3B_y)^2}{B_{x1}^2 + B_{y1}^2} + \frac{(5B_x)^2 + (5B_y)^2}{B_{x1}^2 + B_{y1}^2} + ...} \tag{3.25}$$

3.4.4 Friction losses

These losses are part of the rotational losses and occur due to the friction in the bearings of the machine. Frictional losses can be expressed as [37]:

$$P_f = k_b m_r \frac{60 f}{p} 10^{-3} \tag{3.26}$$

Where

k_b is the bearing friction factor

m_r is the mass of the rotor

f is the frequency

3.5 Axial flux PM Machine Loss Modeling

Like Halbach array machines, axial flux PM machines also experience open circuit and load losses. The main losses of the axial flux machine are modelled in this section

3.5.1 Copper losses

Expressions 3.21 and 3.22 are used to calculate copper losses in axial flux PM machines.

3.5.2 Windage losses

As the machine rotates, there are frictional forces between the rotor and the air surrounding it. These losses become more prominent as the speed of the machine increases. The derivation of the model for these losses is based on the fact that in gases, the shear stress is proportional to the rate of change of shear strain. Windage losses can be expressed as [37]:

$$P_{wind} = \frac{1}{2} c_f \rho (2\pi n)^3 (R_{out}^5 - R_{in}^5) \tag{3.27}$$

Where

D is the rotor diameter

l_g is the air gap length

l is the axial length of the machine

f is the frequency

p is the number of poles

3.5.3 Winding eddy current loss

Similar to the radial flux Halbach array machine, axial flux PM machines also experience rapid variation of flux density within the stator windings. The rapid variation induces eddy currents in the windings which in turn lead to eddy current losses. Expressions 3.24 and 3.25 can be used to predict eddy current losses in the stator windings.

3.5.4 Friction losses

These losses are part of the rotational losses and occur due to the friction in the bearings of the machine. Frictional losses can be expressed as [37]:

$$P_{fr} = 0.006 k_b (m_r + m_{sh}) n \tag{3.28}$$

Where

k_b is the bearing friction factor

m_r is the mass of the rotor

m_{sh} is the mass of the shaft

n is the speed of the machine

3.6 Thermal Modelling of High Speed PM Machines

The capability of the various components of a machine to withstand operating temperatures is an important consideration when designing machines. this is more so when designing machines for high speed applications. This is because high speed machines are generally small and consequently have limited thermal surfaces for heat evacuation. This problem is further exacerbated in high speed flywheels where the machine and the flywheel are both placed in a sealed chamber for safety reasons. However, turbulence within the chamber can lead to increased windage losses and thus reduce the efficiency of the machine. Vacuum operation could provide a solution to the windage loss reduction. The direct result of the vacuum is that heat evacuation by convection is limited and this poses conflicting design challenges. In [13] a helium-air mixture is used in order to reduce windage and at the same time allow for heat evacuation via convection.

Prediction of the exact thermal behaviour of a machine is an extremely challenging task due to numerous variable factors that are difficult to predict. The thermal study of a machine is a 3D problem and is therefore complex to solve, as it require large amounts of computational capability. Various techniques such as finite element and numerical methods exist that enable designers to predict the order of magnitude of operational temperatures. However, the reduced accuracy associated with typical 2D solutions and the computational time makes them undesirable [27]. A “thermal circuit” method based on lumped parameter approach is used in [27], [37], [39], and has been shown to yield satisfactory results. The main challenge in using

this method lies in determining the coefficients of the various circuit parameters which often require empirical data.

Heat transfer in machines is a complex and nonlinear problem. Conduction, convection and radiation are the three ways in which heat is transferred in machines. Conduction takes place between machine parts that are in direct contact with each other such magnets and rotor disks. Convection takes place in parts that have air or other gasses present in-between. Radiation occurs in any environment and is mainly a property of the emissivity of the materials in the machine. In normal air cooled machines, radiation is considered insignificant. However this may not apply to high speed machines operated in a vacuum where convection is limited. The 3 heat transfer methods are discussed in this section. A lumped parameter model is also discussed together with the determination of its parameters for axial flux PM machines.

3.6.1 Heat transfer by conduction

Under steady state conditions, the process of heat transfer by conduction is governed by two thermal laws stated as [27]:

1. The divergence of a heat flux vector is equal to the heat source density in a region
2. The heat flux at any point in an isotropic region is proportional to the temperature gradient at that point.

These laws can be expressed mathematically as [27]

$$\nabla.\vec{\psi} = w \tag{3.29}$$

$$\vec{\Psi} = -k\nabla T \tag{3.30}$$

Where

$\vec{\psi}$ is the heat flux vector

w is the heat source density.

k is the thermal conductivity of the material

T is the temperature

In high speed flywheel machines, conduction takes place from the rotor disks through the shaft and support structure to thecontainment.

3.6.2 Heat transfer by convection

Under room temperature and atmospheric pressure, a considerable amount of the heat in machines is evacuated by convection. For axial flux PM machines, the heat transfer is mainly across the airgap region where heat is transferred from the stator windings to the rotor disks and the surrounding. The convection process in machines is influenced by a number of factors including: speed of rotation, roughness of rotating surfaces and the amount of air or liquid flow in the case of forced convection. Heat transfer by convection is governed by Newton's law which states that the heat transfer is directly proportional to the surface area and the temperature gradient. This law is expressed mathematically as [44]:

$$Q = \alpha A(T_s - T_a) \tag{3.31}$$

Where α is the convection heat transfer coefficient of convection heat transfer, A is the area of the emitting surface, T_a and T_s are the ambient and surface temperatures.

In high speed flywheels, a considerable amount of heat is generated in the stator winding. For coreless axial flux machines, the stator is not physically in contact with its surrounding. Most of the heat is thus evacuated by convection to the rotor disk and the surrounding containment.

3.6.3 Heat transfer by radiation

Radiation contributes very little to the heat transfer processes under room temperature and atmospheric pressure. However, in high speed applications where it is desirable to minimise losses by operating in a vacuum, radiation contributes significantly to the heat removal process. Heat transfer by radiation is governed by the black body radiation equation 3.32 [27].

$$Q = \varepsilon\sigma A(T_s^4 - T_a^4) \tag{3.32}$$

Where ε is the emissivity of the radiating surface, σ is the Boltzmann's constant. The emissivity is the ratio of deviation from perfect black body radiation.

In vacuum operated high speed flywheels, the heat generated in the stator windings of the machine can only be evacuated by radiation to the rotor disks and the surrounding containment since the is no fluid in to provide convection currents. Heat removal from the rotor disks can then take place by conduction through the rotor shaft to the containment.

3.6.4 Lumped parameter thermal network model

The two important parameters in developing a thermal network for a machine are the thermal conductivities and heat capacities of the materials in the machine. With known material volumes, specific values can be determined for the heat capacity and thermal conductance/resistance of the different machine components [40]. These thermal parameters are analogous to electrical parameters. The thermal resistances are treated as electrical resistors, thermal capacities as capacitors, heat sources as current sources and temperatures are taken as voltages. An electrical circuit can thus be formulated and used to analyse the thermal properties of a machine. However, this process requires the setting up of a simple geometry from which nodes and electrical elements can be extracted. Figure 3.4 shows such geometry for an axial flux brushless dc machine.

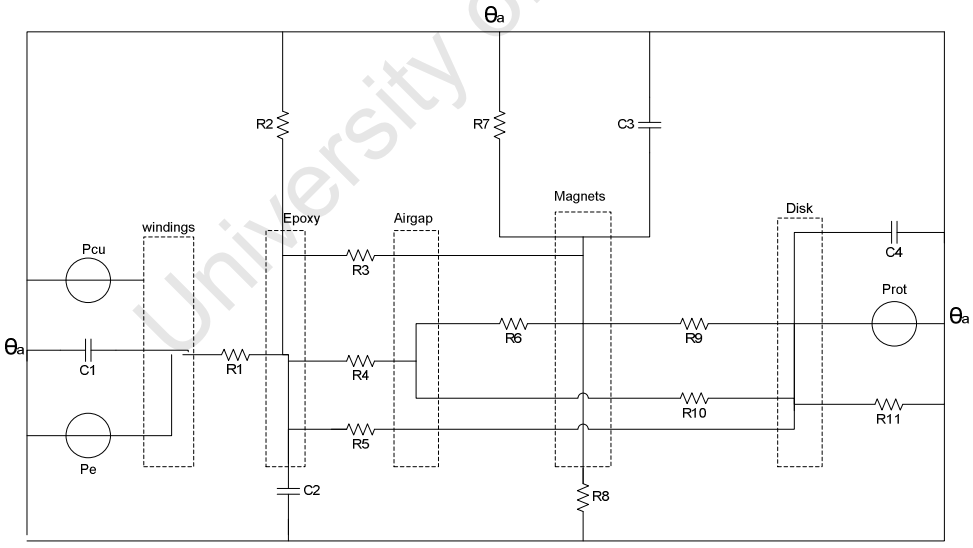

Figure 3.5: Geometry of coreless axial flux machine for thermal modeling.

In figure 3.5, each of the physical components of the machine is expressed as a node. These include: stator windings, the epoxy in which the stator windings are embedded, the airgap, rotor

magnets and rotor disk. The figure illustrates half of the actual BLDC machine and it is assumed the thermal behaviour of the machine between the aforementioned nodes is symmetrical.

3.6.5 Calculation of thermal parameters

The thermal circuit is analogous to an electrical circuit and parameters can be determined in a similar way. Heat sources are modeled as current sources and are represented by series components. Temperatures are modeled as voltage drops and are represented as across components. Equations linking electrical and thermal quantities are discussed in [40]. The analogy between thermal and electrical quantities is summarised in table 3.1.

Table 3.2: Equivalent thermal and electrical quantities.

	Thermal	**Electrical**
Through variable	Heat transfer rate, q (Watts)	Current, i (amps)
Across variable	Temperature, θ (˚C)	Voltage, v (volts)
Dissipation Element	Thermal resistance, Rth (˚C/Watt)	Electrical resistance, R (ohms)
Storage Element	Thermal capacitance, Cth (joules/˚C)	Electrical capacitance, C (farads)

Thermal resistances in the circuit are determined with respect to the thermal path from the simplified geometry. These thermal resistances in the thermal model of a machine comprise the following

- Thermal resistance of conductivity
- Thermal resistance of convection
- Thermal resistance of radiation

The thermal resistance of conduction can be approximated as [27].

$$R_{cond} = \frac{1}{k_{cond} A_{cond}} \tag{3.33}$$

Where k_{cond} is the specific thermal conductivity along a specified thermal path, A_{cond} is the area of the conducting material through which heat is transferred.

The thermal resistance of convection can be approximated as [27]

$$R_{conv} = \frac{1}{k_{conv} A_{conv}} \tag{3.34}$$

Where k_{conv} is the heat transfer coefficient along a specified thermal path, A_{conv} is the area of the convection material through which heat is transfer takes place in the fluid. The calculation of the heat transfer coefficient is slightly more complex as there are several variables involved. This coefficient is influenced by flow of coolant, ambient temperature, speed of rotation of the rotor etc.

The thermal resistance of radiation between two bodies is approximated as [44]

$$R_{rad} = \frac{\frac{1}{\varepsilon_1 A_1} + \frac{1}{A_1 F_1} + \frac{1-\varepsilon_2}{\varepsilon_2 A_2}}{\sigma[(\theta_1 + 273) + (\theta_2 + 273)+][(\theta_1 + 273)^2 + (\theta_2 + 273)^2]} \tag{3.35}$$

Where ε_1 and ε_2 are the emissivities of the first and second node respectively, A_1 and A_2 are the areas of the emitting surfaces, F is the shape factor of radiation and θ_i is the temperature of the respective emitting surfaces. The model takes into consideration that radiant heat transfer is bidirectional i.e. there will be reflected radiation when heat is transferred from one surface to the other by radiation.

The heat capacitance of materials in the machine is analogous to electrical capacitors and this heat retention property is modeled by parallel capacitors in the equivalent electrical circuit. The thermal capacitances are modeled as [12]

$$C = c_i \rho_i V_i \tag{3.36}$$

Where c_i, ρ_i and V_i are the specific heat capacity, the density and volume respectively for the respective part of the machine parts in the simplified machine geometry. Table 3.3 shows calculated thermal resistance and capacitance values for the designed axial flux BLDC machine.

Table 3.3: Calculated thermal parameters for designed axial flux BLDC machine

Parameter	Representation	Value
$P_{cu\,[W]}$	Copper losses	30.000
$P_{rot\,[W]}$	Rotational losses	20.000
$P_{e\,[W]}$	Eddy current losses	1.000
$C_{1\,[F]}$	Winding heat capacity	43.000
$C_{2\,[F]}$	Epoxy heat capacity	200.000
$C_{3\,[F]}$	Magnet heat capacity	92.000
$C_{4\,[F]}$	Rotor disk heat capacity	65.100
R 1	Conduction resistance winding/epoxy	0.375
R 2	Resistance of radiation to surrounding	3.700
R 3	Convection resistance epoxy/magnets	2.430
R 4	Convection resistance epoxy/airgap	1.820
R 5	Convection resistance epoxy/rotor disk	5.230
R 6	Convection resistance airgap/magnets	0.870
R 7	Radiation resistance magnets/surrounding	7.820
R 8	Convection resistance magnets/surrounding	0.930
R 9	Conduction resistance magnet/rotor disk	0.130
R 10	Convection resistance airgap/rotor disk	0.970
R 11	Convection resistance rotor disk/surrounding	1.120
Θ_a	Ambient temperature	30.000

3.7 Finite Element Analysis

Finite element analysis has become a very widely used tool in the design and analysis of machines. This has seen the development of several finite element analysis packages that have enabled non specialists to perform electromagnetic calculations. Using these user friendly packages, designers can set up models and accurately predict the performance of their designed machines. One of the major advantages of finite element analysis is that even complex geometries can be adequately modeled as opposed to analytical equations which will often assume certain geometrical simplifications. The modeling of an axial flux BLDC machine will be outlined in this section.

3.7.1 Finite element theory

Finite element analysis (FEA) aims to simplify partial differential equations that govern the distribution of electromagnetic flux. The relevant theory on electromagnetic field analysis is discussed in [43]. A simplification is performed by breaking down the geometry under consideration into small areas called finite elements. The relevant differential equations are then applied to each element and solutions are approximated using non-linear polynomials.

FEA in electrical machines is based on the conservation of energy. Solutions to field problems are determined by the minimisation of the energy function, given as [43].

$$F = \int_V [\int_0^B H.\vec{dB} - \int_0^A \vec{J}.\vec{dA}]dV \tag{3.37}$$

In the design of a machine, the designer will often want to determine the distribution and magnitude of the magnetic field density, the flux linkage of the windings, the back emf and the electromagnetic torque, the winding inductances, etc.

In this dissertation, a 2D FEA package is used for the design and analysis of an axial flux bldc machine. The package is a static field analysis program used to solve time invariant problems for magnetic and electric fields, called FEMM 4.2.

3.7.2 Modeling of an axial flux machine

The coreless axial flux BLDC machine is modeled as a 2D problem by representing it as a circumferential cross section through the average radius. This is done due to the fact that the flux density distribution is not even from the inner to the outer radius of the machine. The cross section is drawn in the package with the appropriate dimensions and parts. Each of the parts is then assigned material and magnetic properties. As there is no stator core, the windings are modeled as areas filled with the material of the windings. This winding area is calculated based on the practical fill factor. The rotation of the machine is simulated by displacing either the back iron incrementally and keeping the windings fixed or vice versa. It should however be ensured that the boundary conditions are defined adequately to ensure that flux patterns in the elements of the machine do not vary. Figure 3.6 illustrates the modeling of an axial flux machine as a 2 D problem for analysis.

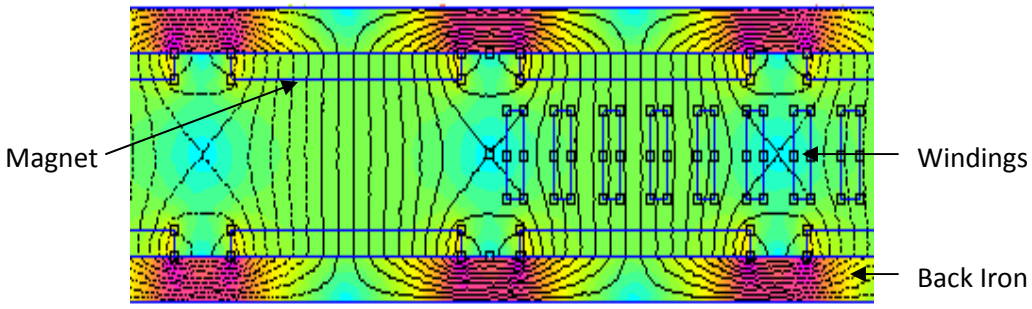

Figure 3.6: Modeling of axial flux machine in 2D package.

3.7.3 Air gap flux density

The airgap flux density magnitude and distribution are important design parameters. They determine aspects of the machine such as saturation of the back iron, losses as well as torque production capability of the machine. The flux density is obtained at a fixed point in the simulating environment as the rotation is simulated as discussed in section 3.7.2. Figure 3.7 shows plots obtained from the FEA package for the designed BLDC machine.

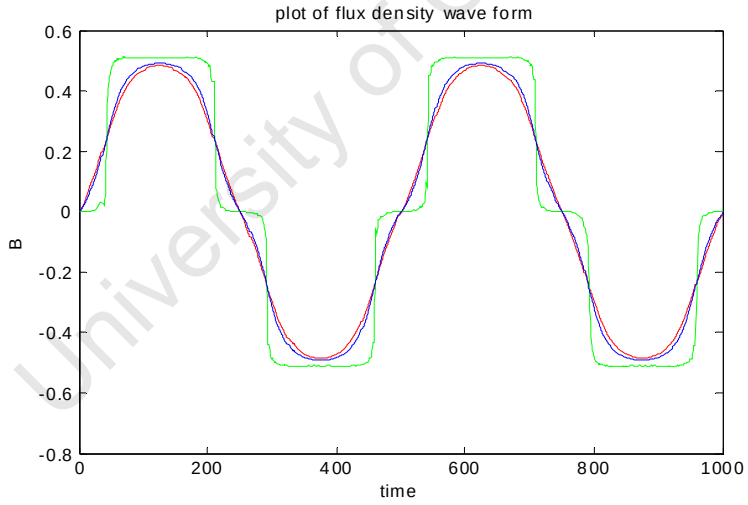

Figure 3.7: Plot of airgap flux density from FEA package.

It is observed from the results that the flux density distribution and magnitude varies as the fixed point of simulation is changed. Points placed closed to the magnet yielded a flat topped flux density wave form. The more the point is moved towards the centre i.e. mid way between the two opposite magnets, the more sinusoidal the wave form becomes. This is due to the fringing of

the magnetic flux towards the centre as can be seen from figure 3.6. the magnetic flux is concentrated at the magnets and fringes toward the centre.

3.7.4 Flux linkage

The flux linkage of the machine is not only dependant on the magnitude and distribution of the flux density of the machine and also depends on the geometry of the stator windings. However in a 2D FEA package, the sector shaped geometry of the stator windings can not be modeled. The stator windings are thus represented as a cross section through the average radius. The area crossed by the flux is thus square, averaging out the over estimate and under estimate towards the outer and inner radius respectively. Figure 3.8 shows the flux linkage obtained from the FEA package.

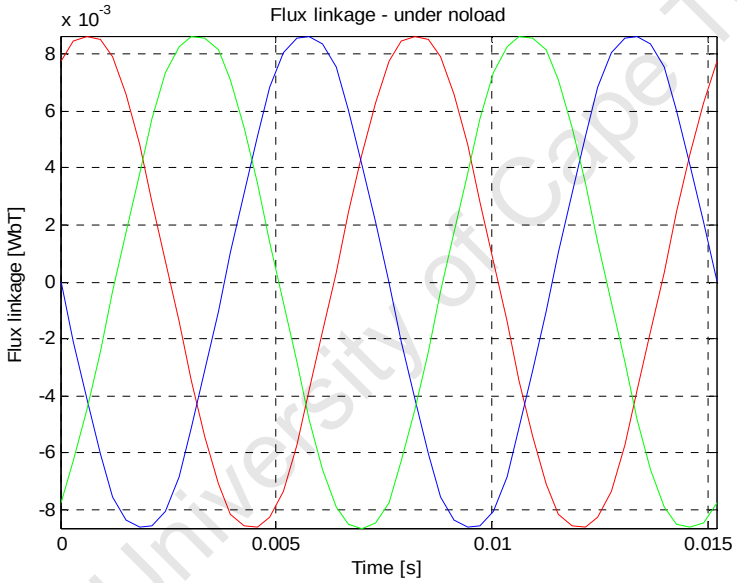

Figure 3.8: Plot of flux linkage from FEA package.

The flux linkage waveform is almost triangular as expected for a brushless dc machine. The deviation from a perfect triangular wave form can be attributed to the fringing effect in the airgap.

3.7.5 Back EMF

The back emf is determined by differentiating the flux linkage obtained from the simulation wrt time, according to equation 3.36 [37]

$$e(t) = \frac{d\psi(t)}{dt} \tag{3.38}$$

Where ψ is the flux linkage of the stator windings. Care must be taken, however to ensure that the time interval for differentiation matches the time steps for the rotation simulation and also the speed of the machine. Figure 3.9 shows the back emf waveform from the FEA package

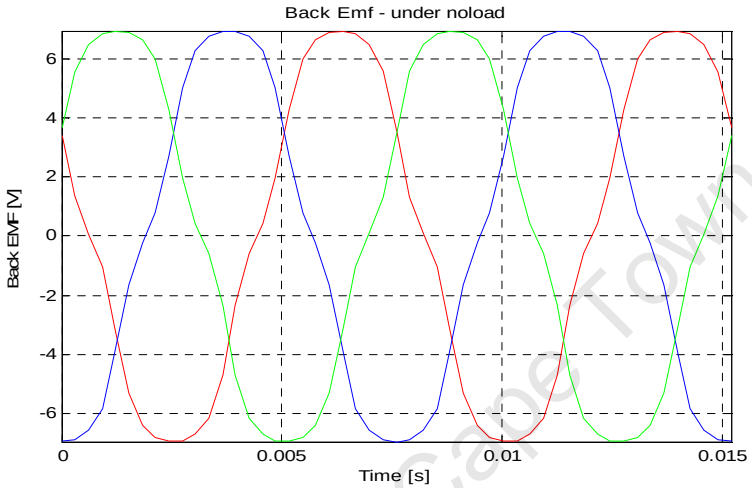

Figure 3.9: Plot of back emf from FEA package.

The implementation of equation 3.36 is thus a finite element assisted matlab function since flux linkage values are obtained from the FEA package.

The observed back emf waveform is characteristic of a brushless dc machine. However, the waveform is not perfectly flat topped and this is as a result of the fringing in the airgap.

3.7.6 Thermal modeling

The FEA package models steady state thermal conduction by ensuring that Gauss law is obeyed in the transfer of heat. Gauss law states that the total heat flux out of any body is equal to the heat generated within the volume of the body. This is analogous to electrostatic problems and can also be represented in differential form as [45]:

$$\nabla . F = q \tag{3.39}$$

Where q is the volume heat generated.

Similar to the electromagnetic problem, the parts of the model under consideration is assigned material properties. Furthermore, the power loss or heat generated in respective parts of the model must be fed as inputs. The input power loss or heat generated is based on estimates from analytical models. Machine designers will usually use power loss as inputs since fully understood models exist that can accurately predict losses in a machine. Heat flux density distribution and magnitudes can then be observed. In this study, stator winding heat generation is simulated since most of the heat is generated in the windings under load conditions. Figure 3.10 shows the stator winding temperature obtained from the FEA package and that obtained from the lumped parameter thermal model.

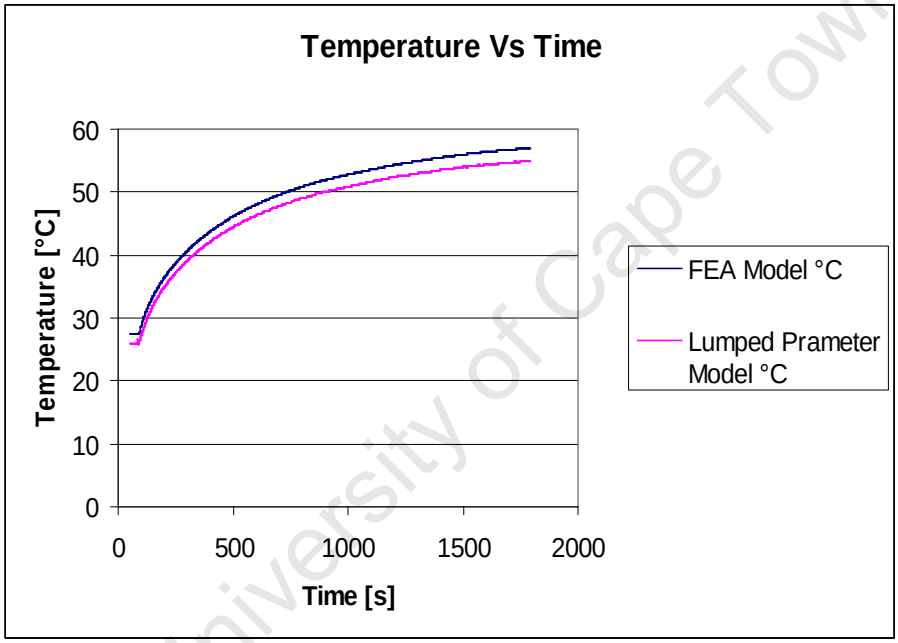

Figure 3.10: Plot of temperature from FEA package and lumped parameter model.

Although there is a slight difference in the magnitudes of temperature obtained, this is satisfactory as it gives the designer a reasonable estimate of the operating temperature.

Chapter 4

4 Sizing and Detailed Design of Axial Flux BLDC Machine

The sizing of the main dimensions of the designed brushless dc machine is determined in this chapter. The designed machine is a four pole double rotor single stator axial flux machine. The magnets are axially magnetised and surface mounted on two mild steel rotor disks. The stator is core less and consists of a three phase overlapping winding cast in epoxy for robustness. The stator is mounted between the two rotor disks.

The design and sizing of machines, especially high speed machines, should take into consideration both electromagnetic requirements and mechanical constraints. This is in addition to application constraints such as space, noise levels and thermal aspects. Often, this results in an iterative process due to the interdependency of mechanical and electromagnetic properties of machines.

Sizing equations for axial flux machine topologies are derived from those of conventional radial flux machine topologies. The relationship between the main dimensions of radial and axial flux machine topologies is illustrated in Figure 4.1 [19].

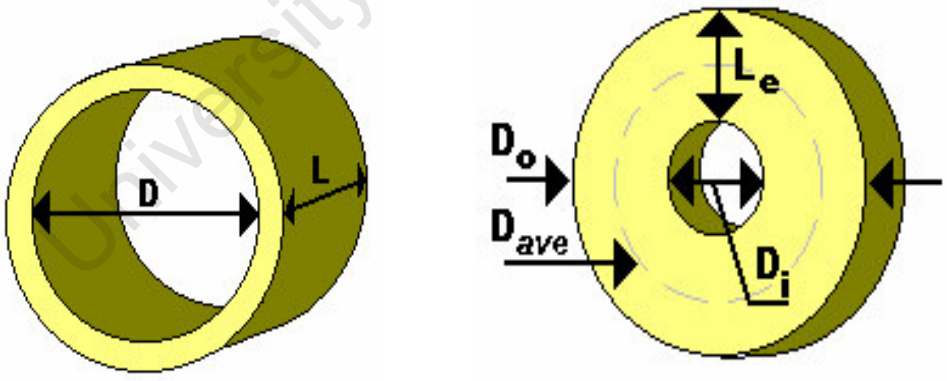

a) Radial flux topology b) Axial flux topology

Figure 4.1: Relationship of axial and radial flux machine dimensions.

A simple transformation can be used to facilitate the use of radial flux sizing equations to determine the dimensions of an axial flux machine in order to optimise power output. This transformation is expressed as [41], [42]:

$$D \Rightarrow D_{ave} = \frac{D_o + D_i}{2}$$

$$L \Rightarrow L_e = \frac{D_o - D_i}{2} \tag{4.1}$$

Where D and L are the diameter and axial length of the radial flux machine, whilst D_{ave}, D_o, D_i are the average, outer and inner airgap diameters respectively of the axial flux machine. L_e is the airgap length in the radial direction.

4.1 Radial Flux Machine Sizing

The output power and torque capability of a brushless dc machine can be expressed in terms of the main dimensions of the machine. This is given as [43]:

$$T = \frac{\pi^2}{4.\sqrt{2}} k_{w1}.B.A.D^2 L \tag{4.2}$$

$$P_{gen} = T\omega \tag{4.3}$$

Where *kw1* is the fundamental winding factor, ω is the speed in radians/sec, A and B are the electric and magnetic loading of the machine respectively. The magnetic loading is dependant on the magnetic material used, whilst the electric loading is usually chosen based on design experience.

Combining (4.2) and (4.3), the product D^2L can be expressed as:

$$D^2 L = \frac{4\sqrt{2} P_{gen}}{\pi^2 k_{w1}.A.B.\omega} \tag{4.4}$$

Equation 4.4 defines the airgap volume required for the specific power speed or torque rating required for the design. The aspect ratio coefficient (L/D) can then be determined after determining the product D^2L in (4.4).

4.2 Axial Flux Machine Sizing

Axial flux machines can be sized in a similar manner to radial flux machines with the aid of the transformation given by equation (4.1). In axial flux machine topologies, the ratio of the outer to the inner diameter of the machine, ($k_d = D_o/D_i$), determines the rated output power. Maximum power is developed by the axial flux machine if this ratio is set to 1.73 [19]. The equivalent airgap product i.e. D^2L in axial flux machine topologies is given as:

$$D_{ave}{}^2 L_e = \frac{1}{8}\left(1+\frac{1}{k_d}\right)\left(1-\frac{1}{k_d^2}\right)D_0^3 = K_D D_0^3 \tag{4.5}$$

From (4.5), a similar equation to (4.4) can be written for axial flux machines and is expressed as:

$$D_0^3 = \frac{4\sqrt{2}P_{gen}}{\pi^2 kw1 AB\omega K_D} \tag{4.6}$$

In this equation, the aspect ratio coefficient is already included and will yield maximum power density.

4.3 Rotor Sizing

An important aspect in designing machines for high speed flywheels is the mechanical integrity. The machine structure should be able to withstand the large mechanical stresses resulting from the high speed operation. Thus, careful consideration must be given to the forces that act on the individual components of the machine. The largest force is experienced in the rotor structure of the machine, since it is rotating and also houses the discrete permanent magnets. The main forces experienced by the rotor structure can be identified as follows:

1. Centrifugal forces on the rotor disks
2. Centrifugal forces on the individual permanent magnets
3. The attractive axial forces between the magnets

Mechanical constraints often dictate the dimensions and materials used in the design and construction of permanent magnet machines for high speed applications. Furthermore, the mechanical constraints will also affect the quality of workmanship and fabrication techniques.

The forces mentioned above will induce stresses within the rotor structure when the machine is in operation. These stresses increase with the speed of the machine and could cause the rotor material to irreversibly deform or fracture. It is therefore imperative that the rotor structure be dimensioned in such a way that these stresses are kept below the maximum permissible values. The structural integrity of the rotor can be assured by considering the material strength in the design.

The diameter of the circle on which the rotor magnet's outer periphery should lie can be determined using equation (4.7) [34].

$$\sigma_u = \rho\omega^2 r^2 \tag{4.7}$$

Where σ_u is the ultimate tensile strength, ρ is the density of the magnets, ω is the angular speed in radians/sec and r is the radius. Similarly, equation 4.7 is also used to determine the outer diameter of the rotor disks. **Error! Reference source not found.** shows the variation of the disk diameter with speed

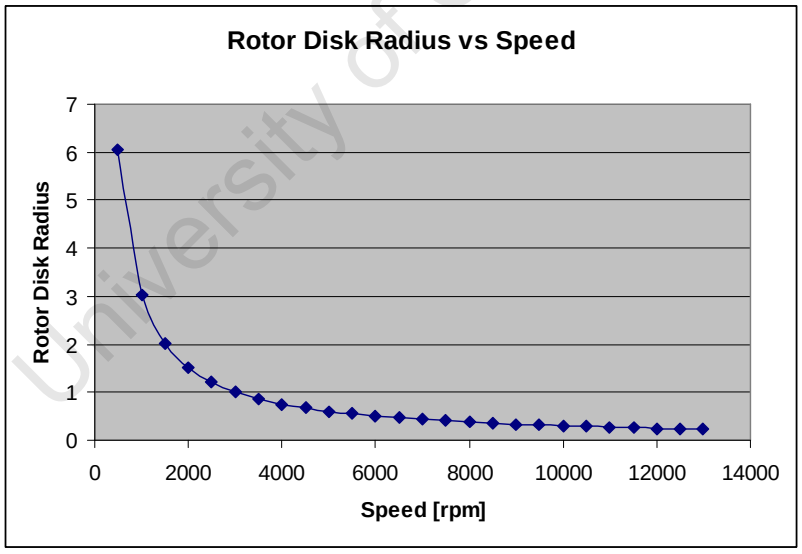

Figure 4.2: **Variation of rotor disk radius with speed.**

The maximum permissible diameter of the rotor shaft is determined by [7]:

$$D \leq \sqrt{\frac{8\sigma_u}{\rho\pi^2 n^2 (3+\nu_p)}} \tag{4.8}$$

Where σ_u is the ultimate tensile stress, ρ is the density, n is the rotational speed and ν_p is Poisson's number. Figure 4.2 shows the variation of the shaft diameter with speed obtained from equation (4.8).

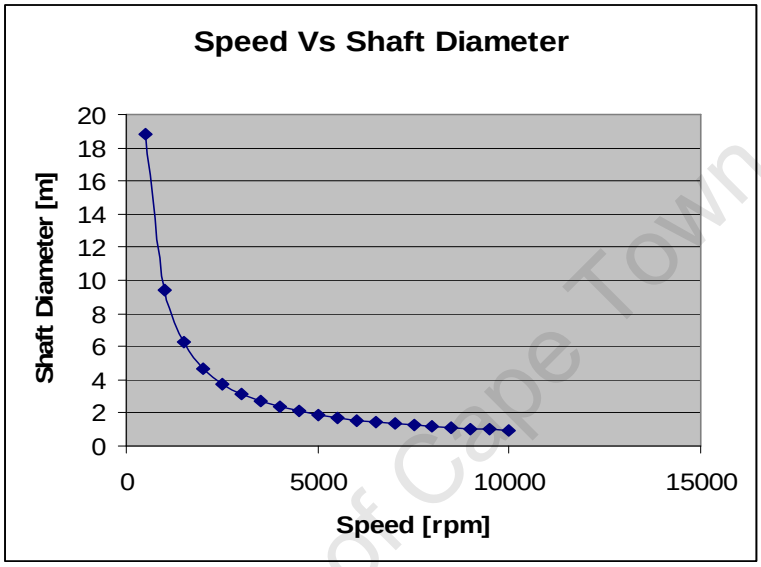

Figure 4.2: **Variation of shaft diameter with speed.**

It can be seen that the shaft diameter drops sharply with increase in speed. The shaft diameter determines the inner diameter of the flywheel which in turn affects the sizing of the flywheel.

In addition to stresses caused by high speeds, vibrations of the rotor structure can also cause deformation and result in failure. There exist resonant frequencies of these vibrations that compromise the structural integrity of the rotor structure and these are called critical frequencies. Ideally, it is desirable to have a vibration free system. However, unbalance and other asymmetrical issues which are difficult to eliminate will further excite these critical frequencies. The speeds at which they occur are referred to as critical speeds. The critical speed can be determined by [7]:

$$\omega \leq \sqrt{\frac{3ED^2}{\rho l_r^4}} \tag{4.9}$$

Where E is the Young's modulus and l_r is the length of shaft. It can be seen from equation 4.9 that increasing the outer diameter improves the critical speed. However this is contradictory to the stress minimisation requirements. There is thus a trade-off that should be established in order to adequately address the mechanical issues associated with high speed machines.

4.4 Stator Sizing

The design of a coreless stator is a less complicated task than that of a cored stator. Several parameters are ignored such as tooth saturation, core losses and attraction forces between the stator core and the rotor magnets. The major considerations in designing the stator are the coil pitch, the conductor size, mechanical integrity and cooling. The stator should be adequately secured to avoid interference with the rotating parts at high speeds. This is particularly important for high speed flywheel applications where all components are enclosed in a containment unit, which has significant turbulence at high speeds.

The inner and outer diameter of the stator is selected to maximise flux linkage and is kept to the ratio of 1.73 in order to maximise power density [19].

References [4-9] discuss machine design. A low electric loading of 1000A/m is chosen for the machine in order to minimise thermal effects. The number of turns of the machine can thus be determined by:

$$A = \frac{2mN_{ph}I_{rms}}{\pi D} \tag{4.10}$$

Where A is the electric loading, m is the number of phases, N_{ph} is the number of turns per phase, D is the average diameter of the stator and I is the rms current. In order to determine the conductor size, a current density is chosen. The diameter of the conductor is thus given by:

$$D_{cond} = \sqrt{\frac{8mN_{ph}I_{rms}}{A\pi^2 D}} \tag{4.11}$$

The stator winding is constructed on a dummy core that is later removed to obtain a coreless winding. The design of the stator is therefore very similar to machines with cores. The number of slots per pole is chosen and the slot pitch is given by:

$$\tau_{slot} = \frac{\pi D_i}{n_{slot}} \tag{4.12}$$

Where D_{ave} is the inner diameter of the stator and n_{slot} is the total number of slots. The slot width is determined by:

$$w_{slot} = h\tau_{slot} \tag{4.13}$$

Where h is the slot width/pitch ratio and is chosen in the range 0.5 to 0.6. The slot area and slot depth are determined by

$$A_{slot} = \frac{A_{cond} N_{ph}}{N_c k_f} \tag{4.14}$$

$$h_{slot} = \frac{A_{slot}}{w_{slot}} \tag{4.15}$$

Where A_{cond} is the conductor area, N_{ph} is the number of phases N_c is the number of coils per phase and k_f is the slot fill factor.

Using the equations discussed above, two axial flux brushless dc machines were sized and constructed. The first machine has a power rating of 150W and a rated voltage of 12V. The second machine has a power rating of 500W and a rated voltage of 50V. Tables 4.1(a) and (b) summarise the design values.

Table 4.1a: Design values for 150W machine.

Design Parameter	Value
Number of poles	4
Inner/Outer diameter	80mm/46mm
Axial length of stator	23mm
Mechanical airgap	2mm
Electric loading	10000A/m
Current density	4A/mm
Gauge of conductor	18AWG
Number of turns/phase	32
Magnetic loading	0.47T
thickness of magnets	8.5mm
Remanent flux density	1.2T
Thickness of back iron	9mm

Table 4.1b: Design values for 500W machine

Design Parameter	Value
Number of poles	4
Inner/Outer diameter	150mm/80mm
Axial length of stator	26mm
Mechanical airgap	2mm
Electric loading	15000A/m
Current density	$6A/mm^2$
Gauge of conductor	17AWG
Number of turns/phase	32
Magnetic loading	0.7T
thickness of magnets	10mm
Remanent flux density	1.35T
Thickness of back iron	10mm

The 500W machine was an enhancement of the 150W. The enhancement was necessary to overcome the excessive stiffness of the bearings that were made use of in the prototyping of the BLDC machine. In order to ensure that currents were kept low, thus minimising thermal effect, the rated voltage of the machine was also increased.

The purpose of the 150w machine was:

- To validate electromagnetic design procedure
- To validate thermal model and effect
- To validate mechanical integrity/balancing issues
- To test and asses machine performance without the flywheel in generator mode.

The purpose of the 500W machine was:

- To integrate the machine with the flywheel
- To ensure adequate acceleration torque for the flywheel
- To assess the capability of the machine to withstand thermal effects whilst in the containment unit

Chapter 5

5 Prototyping of Axial Flux Machine

As discussed at the end of chapter 4, two prototypes were constructed. This chapter presents details on the prototyping procedure. The prototyped machines are axial flux brushless dc machines with coreless stators. The physical dimensions of the two machines differ according to their power ratings and slightly different prototyping techniques were employed in order to handle the different volumes of material.

The main components were prototyped at the University of Cape Town in order to minimise the cost. Careful dimensioning was performed and materials selected based on strength in order to withstand the large centrifugal forces at high speeds, as well as their electromagnetic properties, in order to realise the desired electrical performance. The design process has been discussed in the previous chapter. The main components in the design include: the magnets, the rotor disks, the stator windings, the stator epoxy casting and the mounting base. The initial machine design did not take into consideration the mounting configuration in an enclosure and was therefore less complicated to assemble. However, the second machine considers the entire flywheel system with the machine mounted in a containment that is airtight. During the design and prototyping process, careful attention was paid to the following:

a) Mechanical integrity
b) Thermal effects
c) Financial cost

The construction process included the following main steps:

a) Laser cutting of rotor disks and retaining rings
b) Positioning and retention of magnets on disks
c) Construction of stator windings and positioning in mould
d) Fabrication stator casting for winding
e) Manufacture of shaft
f) Mounting of base

The materials used for the respective parts are the same for both machines. Additional materials such as water cooling ducts were inserted in the stator of the larger machine to provide adequate cooling since it was enclosed in a containment unit.

5.1 Construction of Rotor Disks

The rotor disks were laser cut from 300WA mild steel. Although most machines are manufactured from higher grade steels such as “M” grade steels, 300WA steel was used due to its availability and cost. The 300WA steel has adequate mechanical properties capable of withstanding upto 300% of the predicted forces at the rated speed of the flywheel. The inner and outer diameters are carefully cut out using a laser cutting tool. The two disks are then polished in order to ensure that the surface of the magnets form flush contact with the disks. Figure 5.1 shows the rotor disks of the 150W machine.

Figure 5.1: Polished rotor disks with retaining rings fitted.

The disks are fitted with retaining rings made from stainless steel 306. These rings fit around the outer diameter of the magnets and are carefully chosen to be non-magnetic in order to avoid interference with the magnetic path. Stainless steel 306 also has adequate mechanical properties to withstand radial forces exerted by the magnets at the rated speed.

The magnets are positioned using fabricated Perspex spacers. These ensure that the magnets are placed at exactly 90 degrees from each other, since there are 4 poles. A thin layer of glue is provided on the surface where the magnets are placed. When the magnets are in position, the spacers are removed. Further retention of the magnets is provided by pouring epoxy mixed with an appropriate hardener into the spaces between the magnets. A stopper is placed at the inner diameter of the disk to ensure that no epoxy flows into the central hole of the disk. The properties of the epoxy are also checked to ensure that no fracturing will occur at the rated speeds. The epoxy used has a thermal rating in excess of 180 degrees Celsius. This is well within the designed and predicted limits of thermal operation of the machine. Figure 5.2 shows the rotor disks for both machines with the retaining rings, magnets and epoxy.

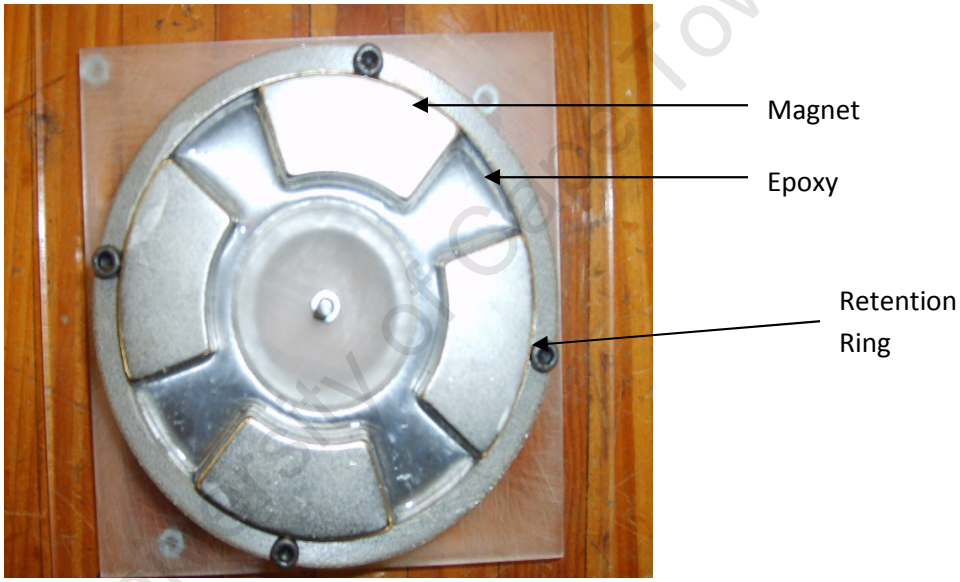

(a) Rotor disk of 150W machine.

(b) Rotor disk of 500W machine

Figure 5.2: Rotor disks with magnet retaining rings and epoxy.

The prototyping technique is the same for the rotor disks of both machines. However, the rotor disk for the 500W machine has an extra inner retaining ring to provide support for the keyed spacers that fit onto the shaft of the machine. The spacers are used to separate the rotor disks and thereby to withstand the attractive force between the PMs.

5.2 Stator Winding

The stator winding of the 150W machine is formed from two layers of magnet wire with 0.8mm diameter. The use of two layers of conductors for the phase windings ensures that current densities are kept to the designed values whilst maintaining flexibility since the machine is relatively small. A double layer winding also ensures that the eddy current losses within the conductor are kept to a minimum. The layering is achieved by placing two stator windings in parallel.

The stator of the 500W machine is a single layer winding made from 1.2mm diameter class H magnet wire. The prototyping technique is similar to that of the smaller machine's stator winding. However, water cooling ducts are placed along side the windings in order to evacuate heat generated when in operation in the vacuum chamber. The ducts are made from a silicon compound with a high melting point and relatively high thermal conductivity. These properties

ensure that the ducts don't melt and at the same time be able to conduct heat away from the windings.

A stator mould was fabricated by laser cutting Perspex pieces to form a square basin. Firmly held screws were then used as spacers for the coils in the stator as shown in figure 5.3.

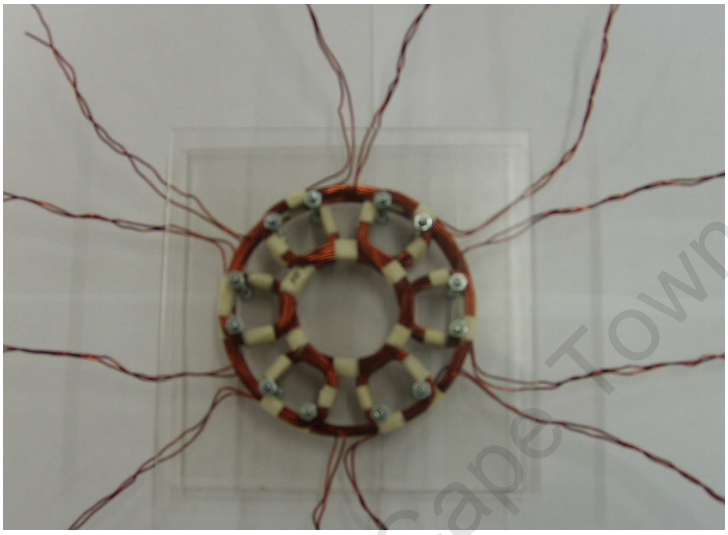

Figure 5.3: Stator coils placed on spacers.

The spacers were placed such that they hold the three phase windings at exactly 120 degrees from each other. The screws are also used to place a cover on top of the windings that keeps the windings compact and thus giving the stator a fixed thickness as per it's design specification. Three thermocouples were fitted at different points on the three phases. One is placed on the inner diameter of the one phase, the other on the outer diameter of the next phase and the third placed in the radial section of the third winding. Care was taken to pour the epoxy layer by layer. This is because the temperature of the epoxy increases when mixed with the hardener and should thus be allowed to cool in thin layers to prevent cracks developing in the stator casting. Figure 5.4 shows the different stages of the stator prototyping.

(a) Square basin mould with spacers and cap.

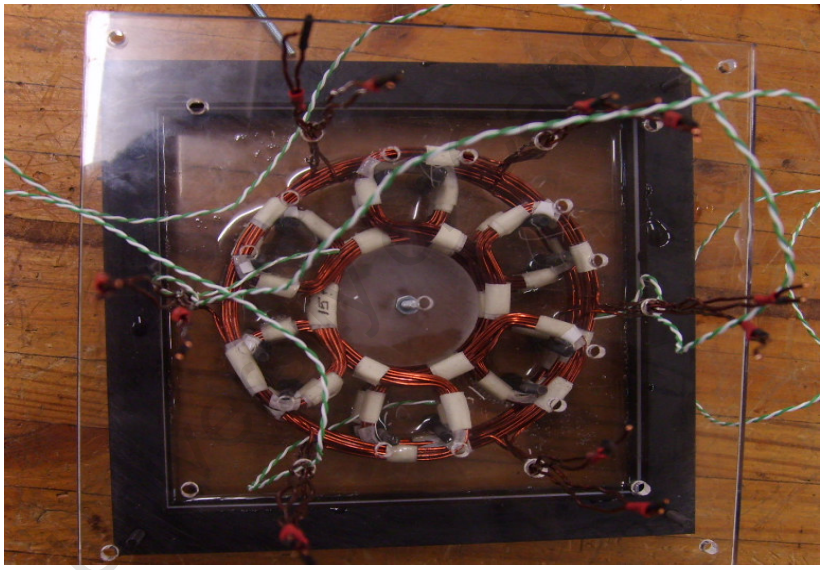

(b) Coils placed with thermocouples fitted.

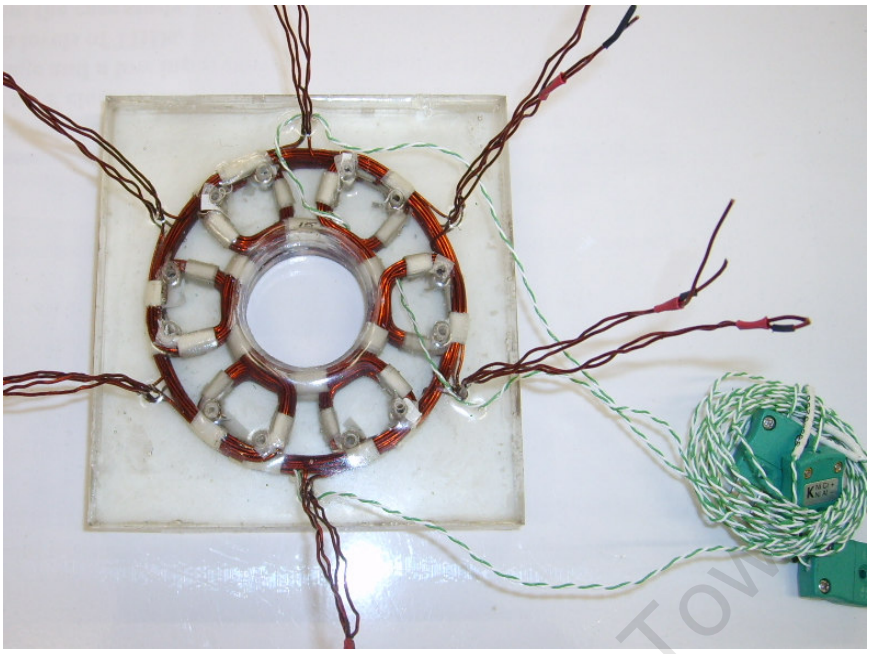

(c) Cast core less stator.

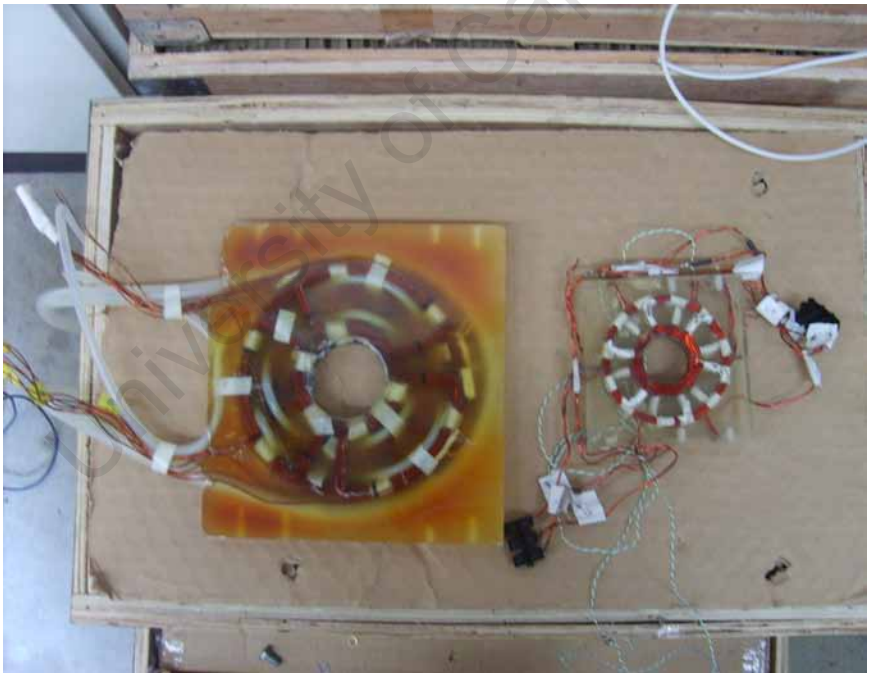

(d) Stators of both machines.

Figure 5.4: (a) square basin mould with spacers. (b) coils placed with thermocouples fitted (c) cast coreless stators (d) stators of 150W and 500W machines

5.3 Machining of the Shaft

The shaft is machined from stainless steel 306. Like the retaining rings, the material of the shaft is also chosen to be non-magnetic to avoid interference with the magnetic path. The shaft is designed such that the two rotor disks can be press fit onto it in such a way that they rest flush on shoulders on either side. The stator should fit in between the two disks without physical contact, since the stator will be stationary. Fabrication of the required shaft is done on a lathe by machining a round bar of stainless steel as per design detail and finally balancing it. Figure 5.5 shows the shaft on the lathe and the fabricated shaft of 150W machine.

Figure 5.5: Fabrication process and finished shaft of 150W machine.

5.4 Machine Containment Unit

The containment unit of the 500W machine was made mainly of steel for strength. The three main components in the construction of the containment unit include: a flat steel base, a cylindrical steel housing chamber and two flat steel end plates. Other components included bearings mounted on the end plates and seals to ensure that an air-tight containment is realised. Auxiliary equipment included a vacuum pump and a water chiller unit, which was set up for use in case of severe testing where currents grossly exceeded rated values. Figure 5.6 illustrates the several components of the containment unit with the flywheel in situ.

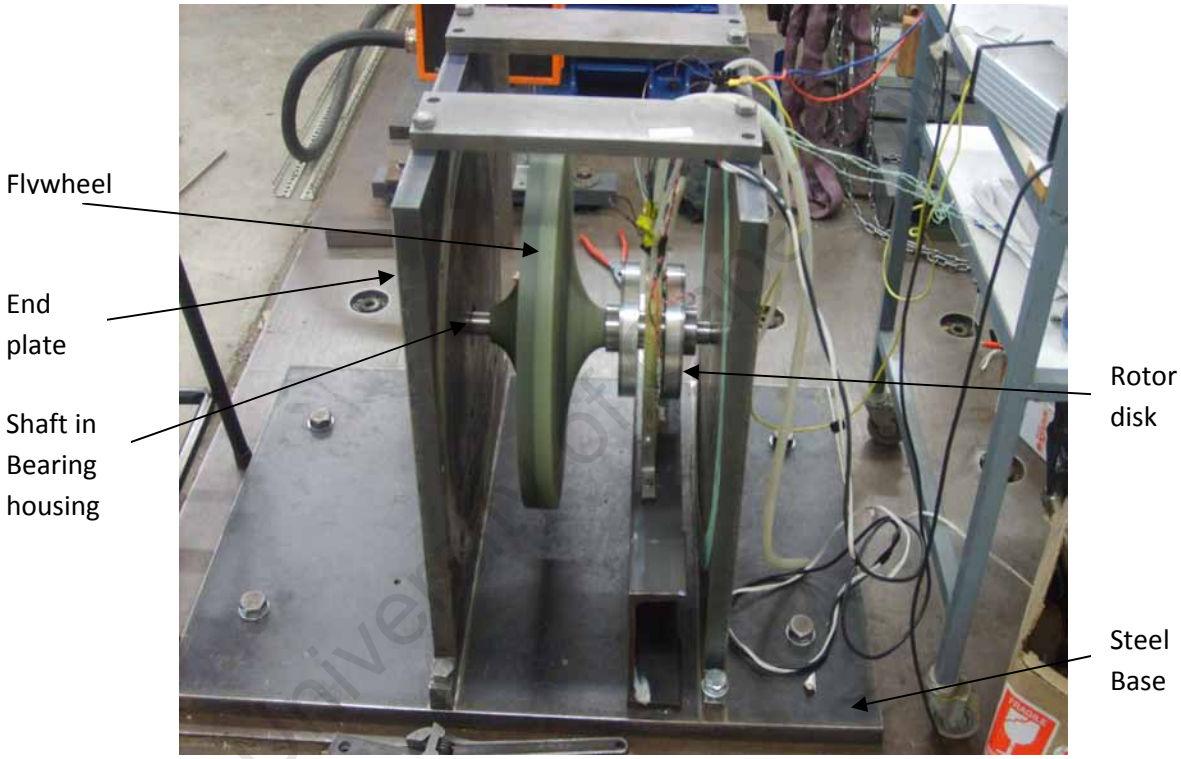

(a) Illustration of housed components.

(b) Cylindrical chamber with drilled access holes.

(c) Cylindrical chamber with stator mounting.

Figure 5.6: (a) Main components of containment unit with flywheel in situ. (b) Cylindrical chamber with drilled access holes. (c) Cylindrical chamber with stator mounting

The cylindrical housing chamber had holes drilled into it to allow access to the machine's windings. The holes were fitted with o-ring seals to ensure the ability of the containment to sustain a vacuum. A base was also fitted in the chamber to mount the stator core.

5.5 Machine Assembly

The components discussed in the previous sections form the basic layout for both machines. As discussed earlier, the 500W machine is housed in a totally sealed containment and is integrated with the complete flywheel system. The smaller machine, meant for functional testing, is neither enclosed nor integrated with the flywheel system. In the smaller machine, the components were put together and mounted on a simple steel base.

The 150W machine mounting comprises a C-channel iron base and two 25mm thick flat bars that act as the housing for the high speed hybrid bearings. The shaft is extended to allow coupling to other machines/flywheel for testing. The assembly is shown in figure 5.7.

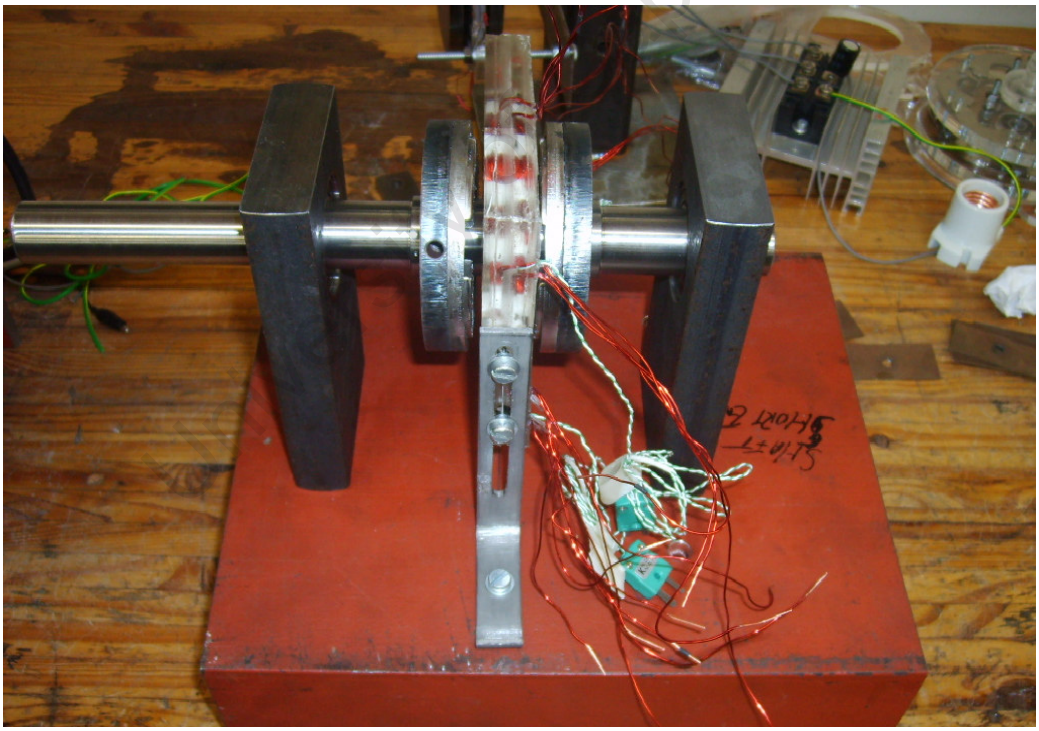

Figure 5.7: Assembly of 150W machine, with various designed components.

The assembly of the 500W machine was more elaborate as it involved the integration of heavier parts. The complete system assembly with the containment is shown in figure 5.8.

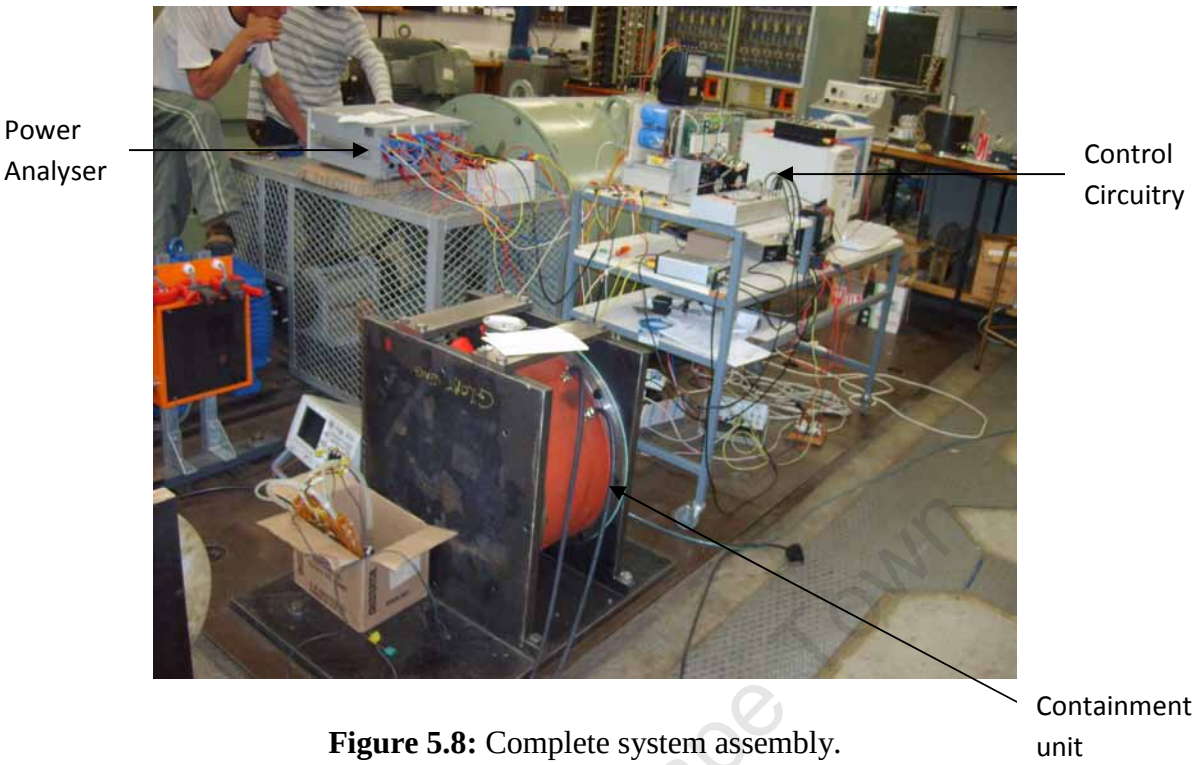

Figure 5.8: Complete system assembly.

Chapter 6

6 Measurements and Testing of Axial Flux Machine

The prototyped machines were tested in the laboratory. Firstly, machine functionality tests were carried out on the 150W machine in order to determine the characteristic quantities such as open circuit back emf, rotational losses, output power, efficiency and thermal characteristics of the machine. It is important to carry out separate functionality test in order to predict with reasonable accuracy how the machine will affect the flywheel system once integrated. Secondly, system functionality tests were carried out on the integrated system. Once the system is integrated, machine testing becomes a challenging task. Especially in high speed flywheel systems where it is desirable to operate in a vacuum. The use of a sealed chamber limits the use of conventional methods since they are intrusive and would consequently compromise the ability of the chamber to maintain a vacuum. The system tests carried out included run-up/run-down tests, back emf and input/output energy tests. The set up of the laboratory equipment for both tests is shown in figure 6.1.

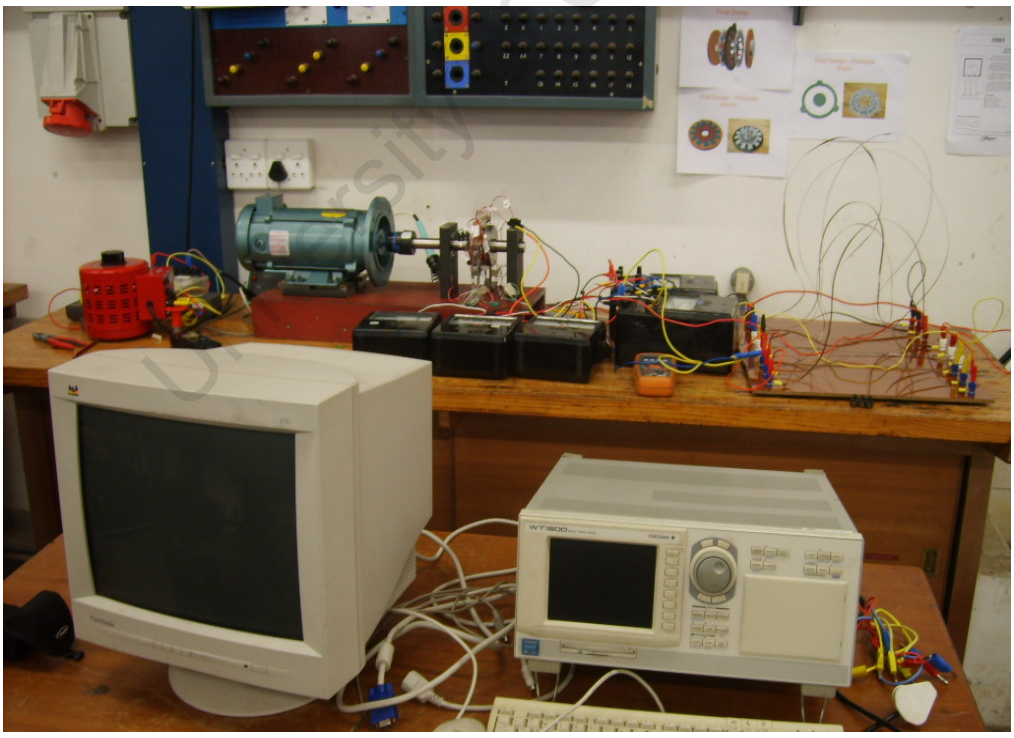

(a) Laboratory setup for machine functionality tests.

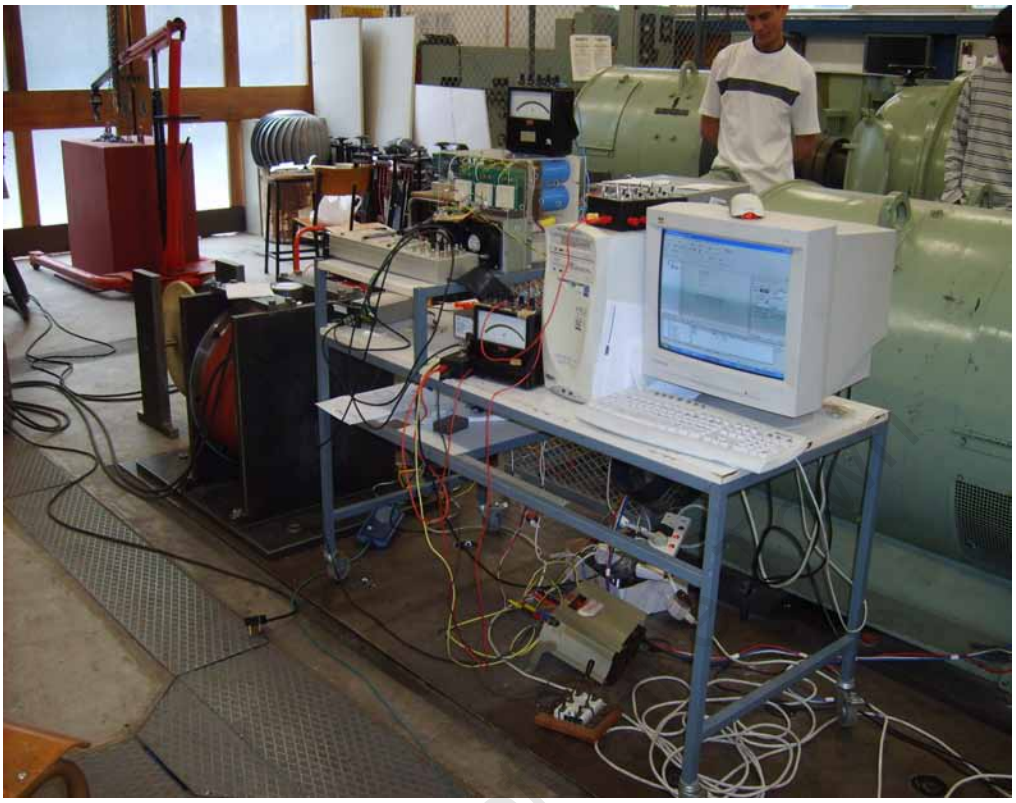

(b) Laboratory setup for integrated system tests.

Figure 6.1: Laboratory test setup for flywheel.

This section discusses the experimental results. The tests were carried out at relatively low speeds since the laboratory that was used was not adequately safe, at the time, to carry out high speed testing.

6.1 Machine Functionality Testing

Accurate measurement of the machine parameters was critical because of the low power rating of the machine.

6.1.1 Arrangement of stator coils

The stator phase windings are arranged as illustrated in Figure 6.2. A phase consists of four coils with two in parallel which are then connected in series to the other two connected in parallel.

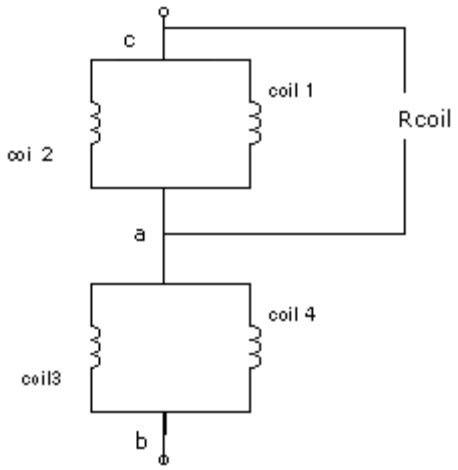

Figure 6.2: Arrangement of coils in one phase.

It is important to understand the arrangement of coils in order to verify measurements of the total phase resistance. The equivalent resistance arrangement for one phase is shown in figure 6.3.

The resistance between nodes a and c (see Fig. 6.2) is obtained using a Wheatstone bridge, and is denoted as R_{coil}. The resistance of the probes R_{probe} is determined and subtracted from the final reading to get the coil resistance. The probe resistance is measured as:

$R_{probe} = 83m\Omega$

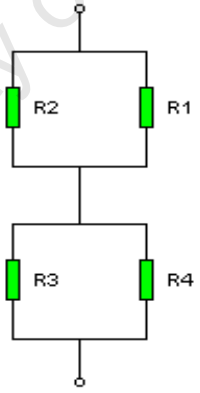

Figure 6.3: Equivalent phase resistance.

The resistances of all the coils are measured and a total resistance obtained. The calculated value is then compared with the resistance measured across b and c for verification. The phase resistances are measured as:

Phase A: 0.083Ω

Phase B: 0.083Ω

Phase C: 0.084Ω

6.1.2 Open Circuit Voltage

The coil, phase and line to line open circuit voltages of the machine were observed. The open circuit voltages of the individual coils placed in parallel are observed. This was done to check if the voltages induced the two parallel coils were in phase. Figure 6.4 shows captured wave forms of the coils.

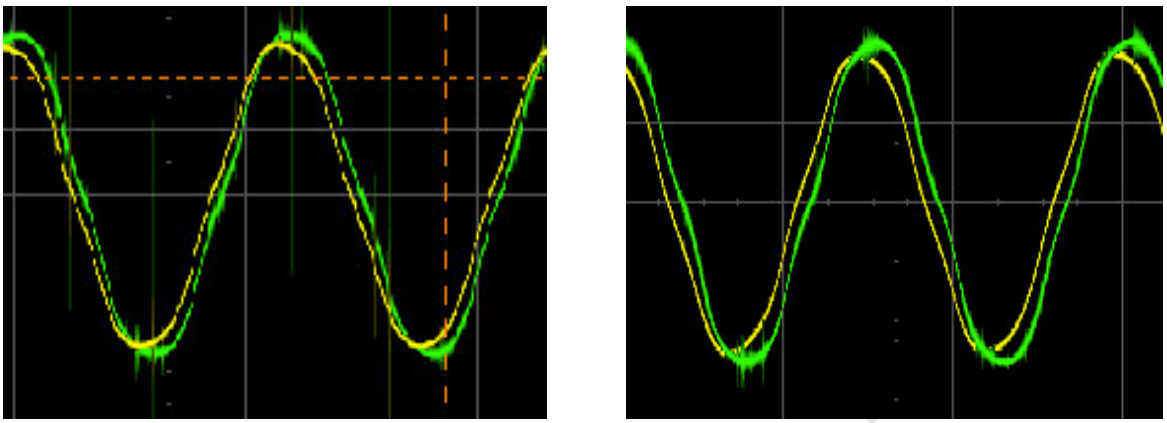

(a) Phase a

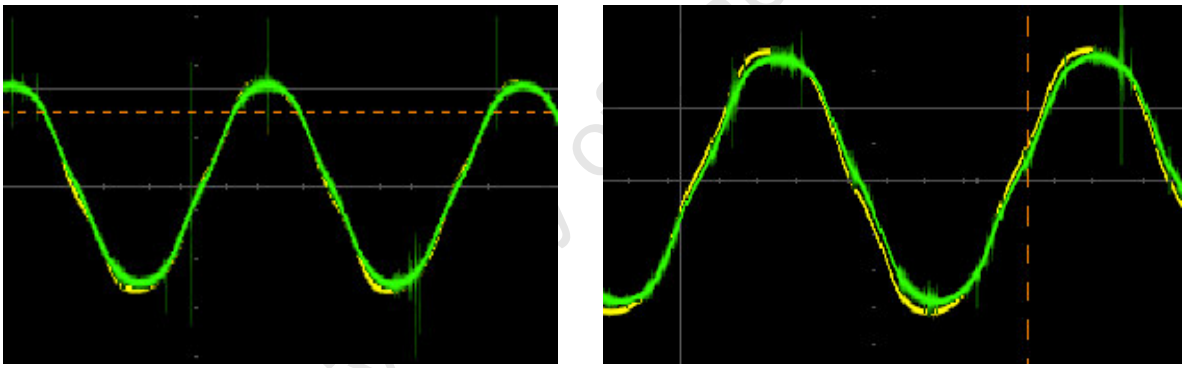

(b) Phase b

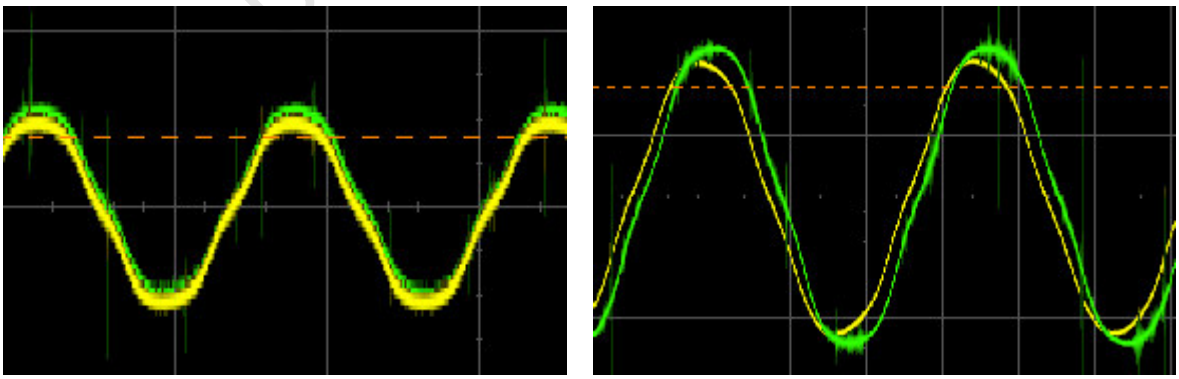

(c) Phase c

Figure 6.4: Open circuit voltage of individual coils.

As can be seen from figure 6.4, the voltages induced in the parallel coils are in phase with a slight phase shift. The phase shift is undesired because it results in circulating currents within each phase and thus causing increased losses in the machine. The coils were connected according to figure 6.2 to form the phase windings. The induced voltages in the phases were observed. Figure 5.4 shows the open circuit voltage of two phases at 300rpm.

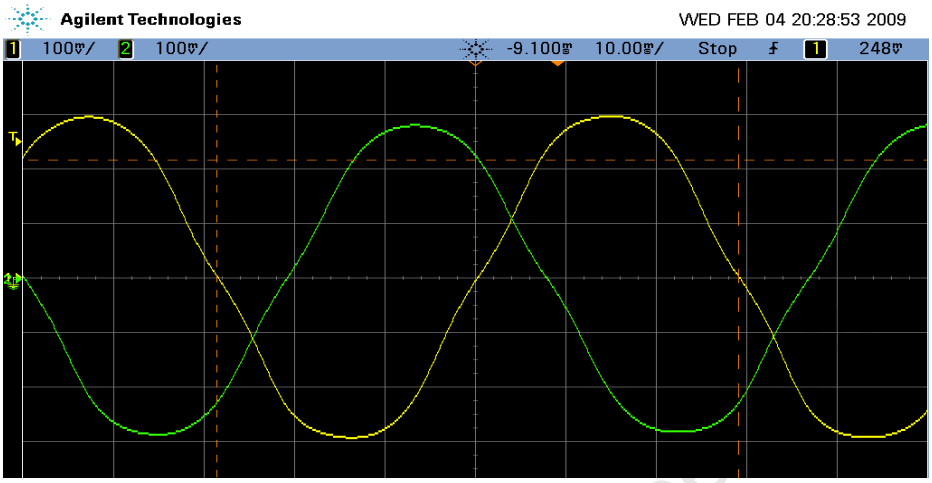

Figure 6.5: Open circuit voltage of two phases of the machine.

The variations of the phase and line-line voltage with shaft speed were plotted for the machine. Figures 6.6 and 6.7 show the variation of phase and line-line voltage with speed tested up to 1400rpm.

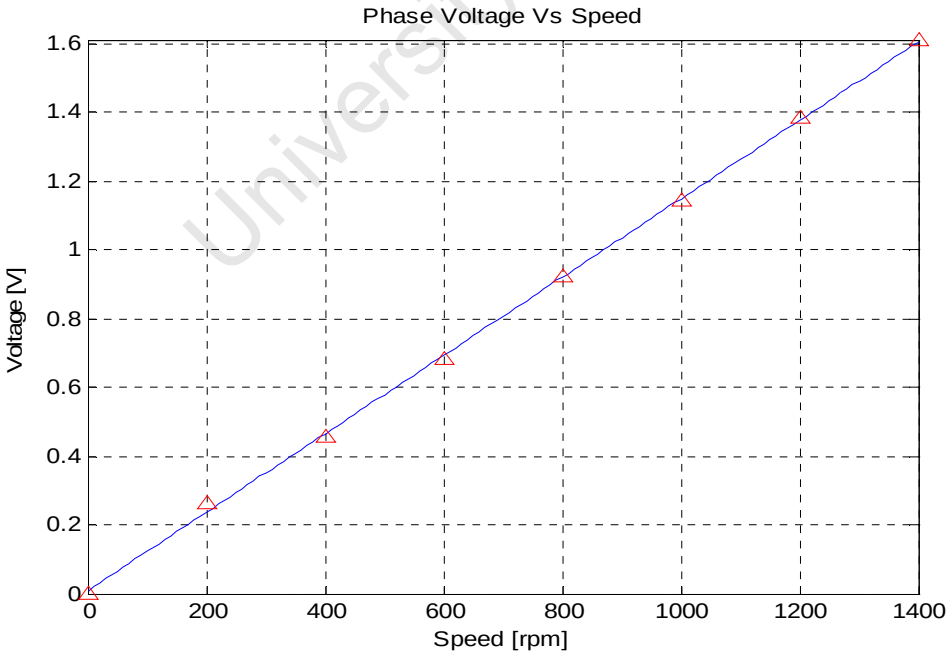

Figure 6.6: Open circuit phase voltage Vs speed.

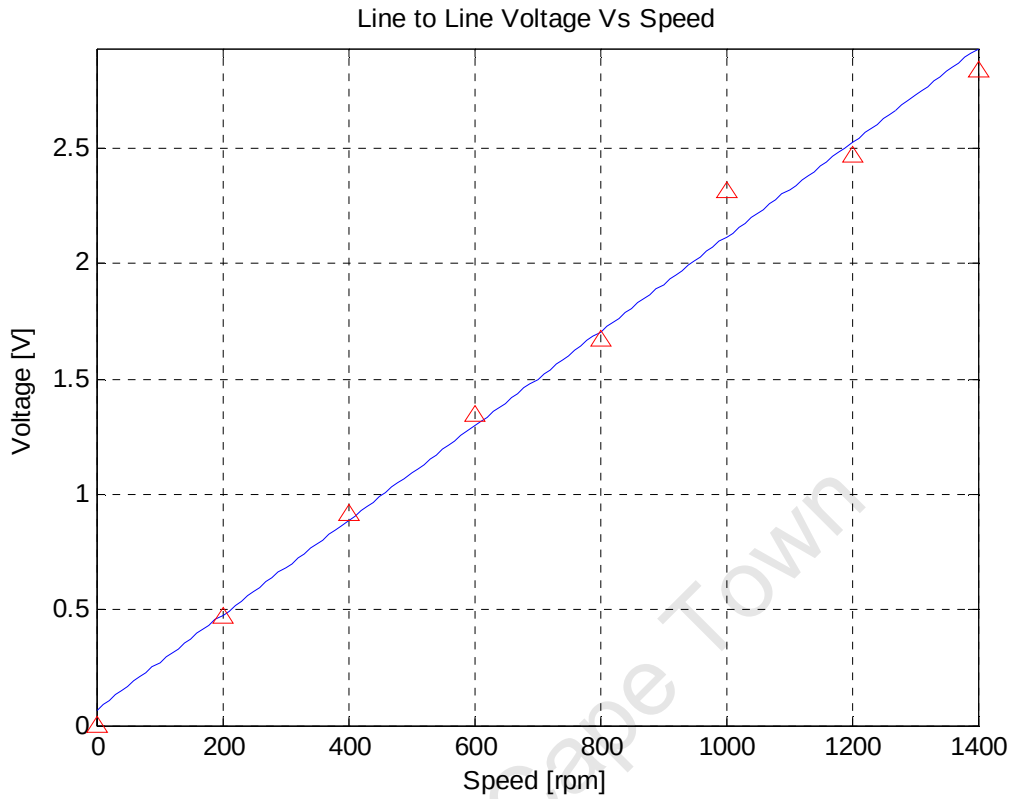

Figure 6.7: Open circuit line-line voltage Vs speed.

The flux linkage established by the PMs was estimated from the plot of phase voltage versus shaft speed shown in figure 6.6. The slope of the best fit curve is used and the value obtained (0.0076 Wb-turns) agrees with the calculated value of 0.0070 Wb-turns.

6.1.3 Rotational losses

The rotational losses are measured under no load conditions and they include friction, windage and stator eddy current losses. Eddy current losses are present in the stator winding due to the rapid variation of the flux density in the conductor. The eddy current losses are normally considerable where thick conductor is used for the stator. In the designed brushless dc machine, the stator winding is made from two strands of 0.5mm conductor. Eddy current losses are thus negligible. The separation of these losses is not easy to achieve and they are normally lumped together as rotational losses. However, there are analytical equations that can be used to model them in order to separate the different losses. Figure 6.8 shows measured rotational losses for the designed brushless dc machine.

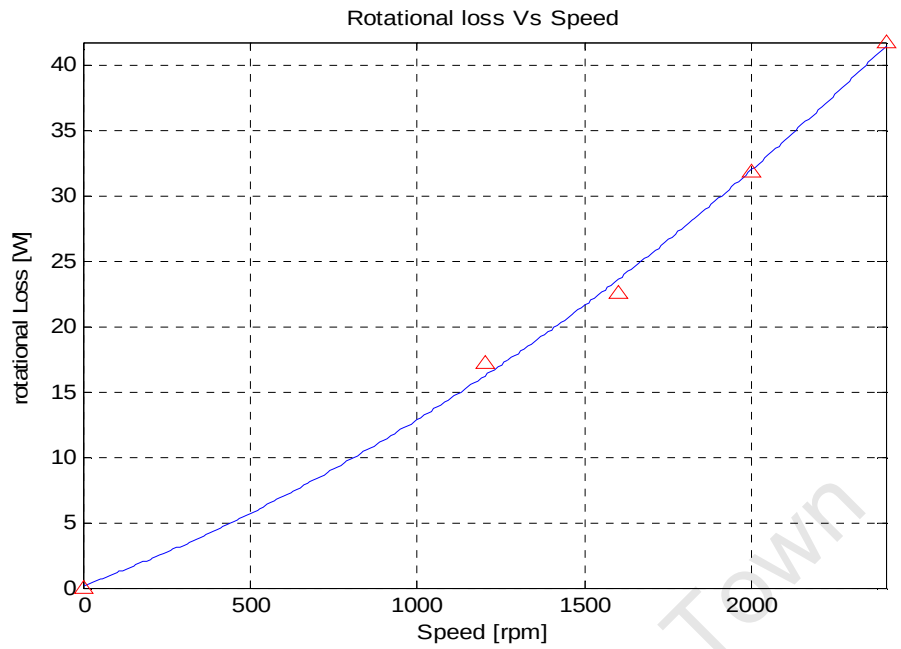

Figure 6.8: Rotational loss versus speed.

6.1.4 Output power

The output power of the prototyped machine was plotted against the shaft speed. The load was kept constant and the speed varied. Figure 6.9 shows how the output power of the machine varies with shaft speed.

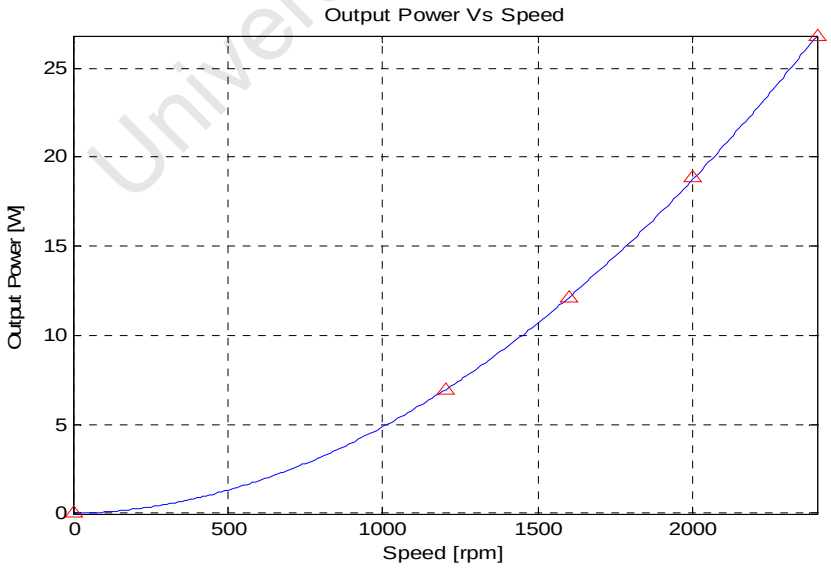

Figure 6.9: Output power versus shaft speed.

6.1.5 Efficiency

Due to the lack of a sufficiently safe containment at the time of testing, the machine's efficiency was measured at speeds considerably lower than the rated resulting in poor efficiencies being recorded. The efficiency of the machine was determined by computing the ratio of the output power to the input shaft power. The input shaft power is determined directly from the readings of the shaft torque and speed and it is given as:

$$P_{shaft} = T\omega \tag{5.1}$$

Where

T is the shaft torque

ω is the shaft speed

The efficiency is measured with varying load whilst the speed of the machine is kept constant. This procedure was repeated for four different speeds in order to observe whether the efficiency of the machine increases with speed. Figure 6.10 shows the variation of efficiency with load. The figure also illustrates the effect on efficiency of increasing the shaft speed.

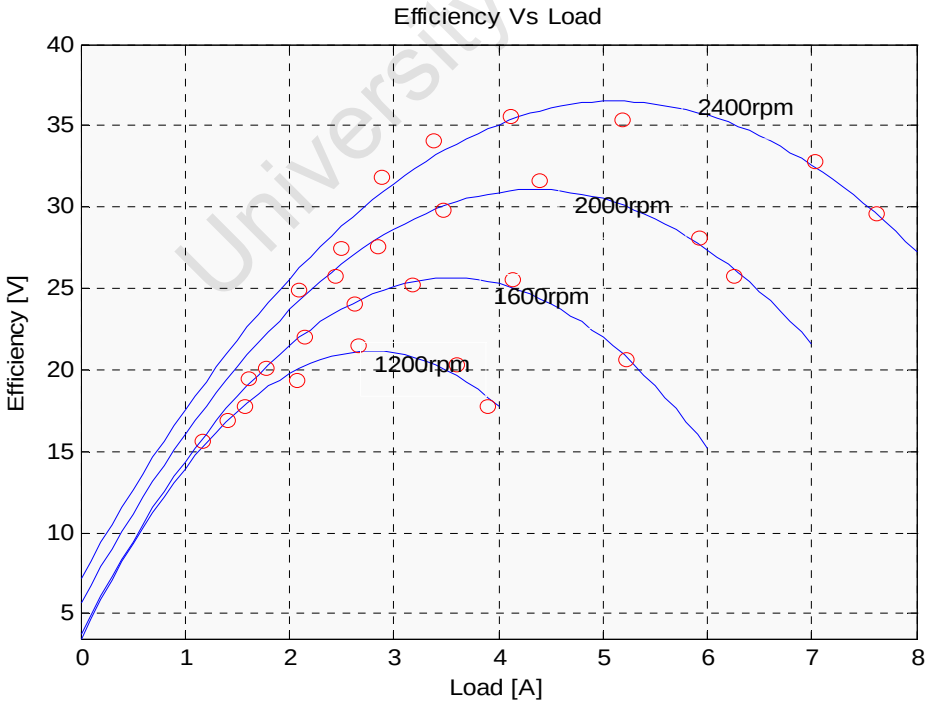

Figure 6.10: Efficiency versus load at different shaft speeds.

It can be seen from the figure that the maximum efficiency of the machine increases. This trend would be observed as the rated speed is approached. There is thus better utilisation of the machine's input power at rated conditions with respect to load and speed.

6.1.6 Temperature tests

The machine was run in generator mode at a constant speed. A determined resistive load was then connected to the machine in order to load the stator winding with rated current. The temperature was monitored on the stator winding as it will suffer the most thermal effects. Thermocouples were place at different points on the winding i.e. the inner and outer diameter end windings. Figure 6.11 shows the rise in stator winding temperature when loaded with rated current.

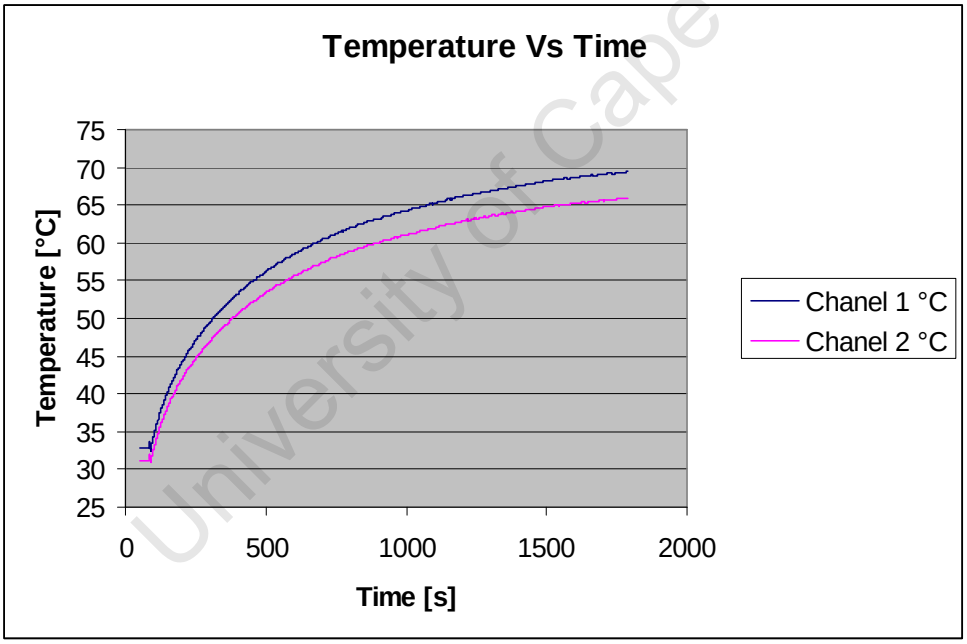

Figure 6.11: Temperature rise at rated current.

It can be seen that the higher temperature is measured at the inner diameter end winding, represented by channel 1. This is expected in an axial flux machine since the inner diameter end winding is less exposed.

6.2 Integrated System Functionality Testing

Non intrusive system tests were carried out on the integrated system. The system is treated as a "mechanical battery" where the charging process is operating the machine in motor mode. The machine is allowed to ramp up in speed upto about 2500rpm. A load is then connected to the terminals of the "battery" thus allowing it to discharge. Figure 6.12 shows the variation of speed over one cycle.

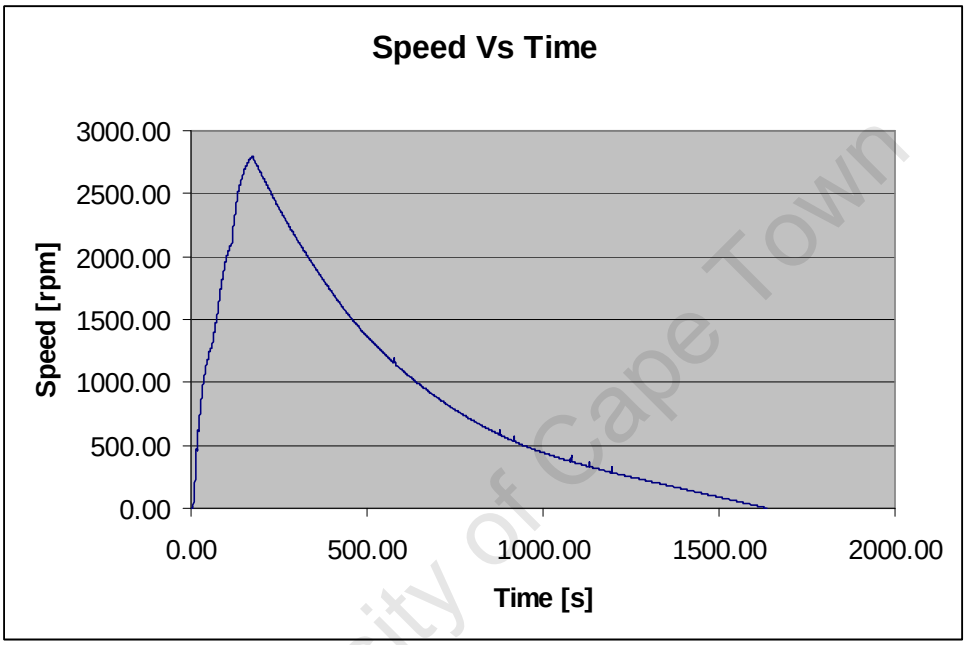

Figure 6.12: Variation of speed with time over a charge-discharge cycle.

The back emf was plotted versus speed for the charging period. The graph is consistent with the design requirements to develop a back emf of 150V at 25000rpm as shown from the equation of the best feet line. The actual back emf curve increases non-linearly in the beginning. This is due to the inertia of the flywheel. However as the flywheel sets in motion, the curve increases linearly with speed which is characteristic for machines as shown in figure 6.13.

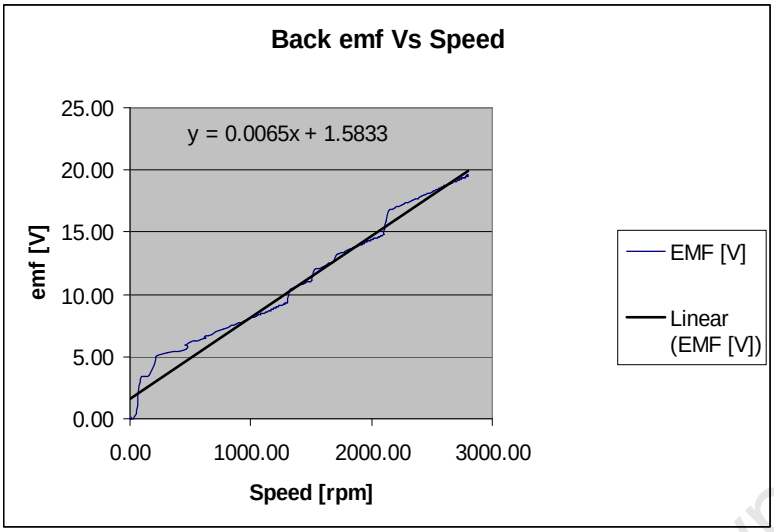

Figure 6.13: Variation back emf with speed during the charge period.

The input power was also measured over the charging period and the output power is measured over the discharge period. Integrating over the respective time, the input and output energies could be determined and thus the round trip energy efficiency. Figure 6.14 shows a round trip power curve.

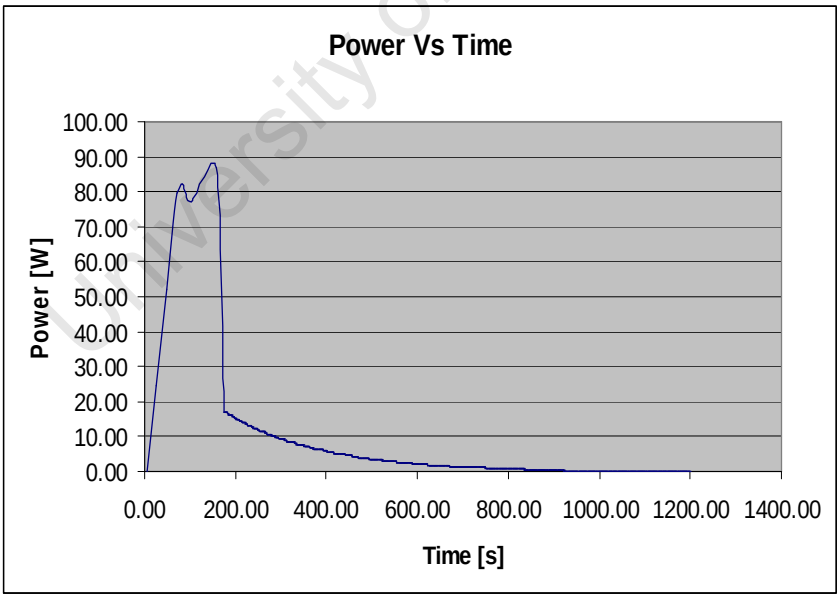

Figure 6.14: Variation back emf with speed during the charge period.

The areas under the charge and discharge curve were determined in order to obtain the input and out put energy. The round trip energy efficiency was calculated using equation 6.1.

$$\eta_e = \frac{Area_{charge}}{Area_{discharge}} \tag{6.1}$$

The round trip efficiency with a 12W load connected was determined as 41%. The low efficiency was mainly as a result of operating the machine considerably below it rated speed and load. The bearings that were mounted were also quite stiff and resulted in further losses. In addition, stray losses also contributed to the poor efficiencies.

Chapter 7

7 Conclusions and Recommendations

7.1 Conclusions

In this dissertation, a study of several PM machine topologies is carried out to determine which topology is best suited in the design of a high speed flywheel. Based on the findings of the study, the following conclusions are drawn:

7.1.1 A comparison is made for a number of PM machine topologies, including several variations of radial and axial flux PM machines. Axial flux PM machines have a better performance in high speed flywheel applications. This is due to their higher power/torque densities. Their geometry minimises the containment size which in turn reduces material costs as well costs of auxiliary equipment such as vacuum pumps. In particular, the axial flux BLDC machine topology is found to be more suitable for the high speed flywheel application than the axial flux BLAC machine topology due to its simpler control circuitry.

7.1.2 Analytical models are formulated for the radial flux Halbach array and axial flux PM machines. Validation was provided by numerical modeling using a 2D finite element analysis package. A lumped parameter thermal model is also formulated for the designed axial flux PM machine. Experimental results are provided for the electromagnetic and thermal performance of the designed axial flux BLDC machine.

7.1.3 This dissertation outlined a system approach to sizing and designing of a PM machine for high speed flywheels. The design procedure places emphasis on electro-magnetic performance as well as mechanical integrity of the machine. Using this design procedure, a BLDC axial flux machine is constructed that will use the power supplied by PV panel over a period of 4 hours to fully charge the flywheel energy storage. Two machines are prototyped and tested. Due to safety concerns, the tests are performed at a relatively low speed of 2500rpm. The first machine is a 150W machine and is tested for electromagnetic functionality. The electromagnetic was satisfactory and the results obtained wrt to flux density, flux linkage and back emf closely matched the designed values. The machine

gives a low efficiency of 35%. This due to tests being performed at very low speed of 2500rpm relative to the rated speed of 25000rpm. Increased friction losses are also experienced by the machine due to the stiffness of the high speed bearing. A BLDC machine with a rated power of 500W is prototyped, integrated with the flywheel and tested. The machine has a higher power rating to provide enough torque to overcome the increased bearing losses as well as windage and losses on the flywheel. Charge/discharge tests are performed on the integrated system. The round trip efficiency is 41%. Similar to the 150W machine, the efficiency is low because the tests are performed at relatively low speed.

7.1.4 An in-house prototyping procedure is outlined for a coreless axial flux BLDC machine. Prototyping techniques to counteract centrifugal forces experienced by the rotor magnets are also provided. Also outlined in this dissertation is the process of prototyping of an axial flux PM machine for high speed flywheel integration.

7.2 Recommendations

Based on the findings of this dissertation, the following recommendations are made:

7.2.1 In order to improve the efficiency of the machine, optimisation code should be used in the PM machine sizing procedure. The optimisation procedure can further be extended to the sizing of the flywheel in order to design and optimised overall flywheel energy storage system.

7.2.2 Different rotor magnet and stator winding configurations should be studied to determine the optimal configurations for high speed flywheel applications. This is an especially important consideration in the design of coreless high speed BLDC machines where the shape of flux density and back emf waveforms are critical to the efficiency of the entire flywheel energy storage system.

7.2.3 Redesign of the containment should be carried out allow sensors and other condition monitoring equipment to be mounted without interfering with moving parts. Further

consideration must also be given to the stator support structure in order to increase robustness of the system.

7.2.4 To avoid vibrations during operation of the flywheel energy storage system, balancing should be carried out separately on the machine and flywheel. Further balancing should also be carried out on the integrated system. The acoustic noise and losses can be reduced, thus increasing the efficiency of the flywheel energy storage.

References

[1] B.M. Bolund, H. Bernhoff and M. Leijon, "Flywheel energy and power storage systems," *Elservier*, 2005.

[2] H. Liu and J. Jiang, "Flywheel energy storage – An upswing technology for energy sustainability," *Elsevier*, 2007.

[3] C. R. Wagner, R. D. Boyle and D. Kent, "Commercialization of flywheel energy storage technology on the international space station," *Proceedings of the Intersociety Energy Conversion Engineering Conference*, pp. 146-150, July, 2002.

[4] R. F. Post, "A New Look at an Old Idea, The Electromechanical Battery," *Science and Technology Review*, April, 1996.

[5] F. Delattre, "Flywheel Clean Energy storage," *Data Users Conference*, 2006.

[6] J. Gonzales, "Power on the Fly," Engineering and Technology, March 2008.

[7] J. Lahteenmaki, "Design and Voltage Supply of High-Speed Induction Machines," *PhD Thesis*, Helsinki University of Technology, 2002.

[8] P. C. Sen, "Principles of Electric Machines and Power Electronics," 2nd Edition, Wiley, 1996.

[9] J. Pyrhonen, "The High Speed Induction Motor: Calculating the Effects of Solid Rotor Material on Machine Characteristics," Thesis, *Lapeenranta University of Technology*, 1991.

[10] M. A. Khan, "Design of a Universal Drive for Brushless PM Machines," *MSc Thesis*, University of Cape Town, 2002.

[11] H. Zhou and F. Wang, "Comparative Study on High speed Induction Machine with Different Rotor Structures," *Proceeding of International Conference on Electrical Machines and Systems*, pp. 8-11, October, 2007.

[12] J. Saari, "Thermal Analysis of High Speed Induction Machines," *PhD Thesis*, Helsinki University of Technology, 1998.

[13] J. E. Vrancik, "Prediction of Windage Power Loss in Alternators," *Lewis Research Center*, 1968.

[14] Y. Suzuki, A. Koyanagi, M. Kobayashi and R. Shimada, "Novel applications of the flywheel energy storage system," *Elsevier*, 2004.

[15] F. Gieras and Wings, "Permanent Magnet Motor Technology," *Marcel Dekker Inc.*, 1997.

[16] R. Nicolsky, Y. Gorelov and A. S. Pereira, "Superconducting Axial Bearing for Induction Machines with Active Radial Magnetic Bearings," IEEE Transactions on Applied Superconductivity, Vol. 9, No. 2, June, 1999.

[17] K. Murakami, M. Komori, H. Mitsuda and A. Inoue, "Design of an energy storage flywheel system using permanent magnet bearing (PMB) and superconducting magnetic bearing (SMB)," *Elsevier*, 2007.

[18] N. Koshizuka, "R&D of superconducting bearing technologies for flywheel energy storage systems," ***Elsevier***, 2006.

[19] M. A. Khan, "Contributions to Permanent Magnet Wind Generator Design Including the Application of Soft Magnetic Composites," ***PhD Thesis***, University of Cape Town, 2006.

[20] Y. Cheng, P. Pillay and M. A. Khan, "PM Wind Generator Topologies," ***IEEE Trans Ind. Appl.***, Vol. 41, No. 6, December, 2005.

[21] R. Qu, M. Aydin and T. A. Lipo, "Performance Comparison of Dual Rotor Radial Flux and Axial Flux Permanent Magnet BLDC Machines."

[22] G. Mwaba, M. A. Khan and P. Pillay, "Modeling of a Radial Flux Halbach Array Machine for High Speed Flywheels," ***Saupec Machines and Drives***, January, 2008.

[23] D. Johnson, "Design Considerations and Implementation of an Electromechanical Battery System," ***PhD Thesis***, University of Cape Town, 2008.

[24] Cavagnino, M. Lazzari, F. Profumo and A. Tenconi, "A Comparison between the Axial Flux and the Radial Flux Structures for PM Synchronous Motors," ***IEEE Trans Ind. Appl.***, Vol. 38, No. 6, December, 2002.

[25] R. Qu, M. Aydin, and T. A Lipo, "Dual-Rotor, Radial-Flux, Toroidally Wound, Permanent-Magnet Machines," ***IEEE Trans Ind. Appl.***, Vol. 39, No. 6, December, 2002.

[26] K. Halbach, "Design of Permanent Multipole Magnets with Oriented Rare Earth Cobalt Material," ***Nuclear Instruments and Methods***, Vol. 169, 1980.

[27] F. Shanin, "Design and Development of a High Speed Axial Flux Permanent Magnet Machine," ***PhD Thesis***, Endhoven Uuniversity, 2001.

[28] M. R. Dubois, H. Polinder and J. A. Ferreira, "Comparison of Generator Topologies for Direct Drive Wind Turbines."

[29] M. Aydin, M. S. Huang and T. A. Lipo, "Axial Flux Permanent Magnet Disk Machines," ***WEMPEC Review***, University of Wisconsin-Madison, 2004.

[30] K. Sitapati and R. Krishnan, "Performance Comparisons of Radial and Axial Field, Permanent-Magnet, Brushless Machines," ***IEEE Trans Ind. Appl.***, Vol. 37, No. 5, October, 2001.

[31] J. R. Hull and L. R. Turner, "Magnetomechanics of internal-Dipole Halbach Array Motor/Generators," ***Magnetics***, Vol. 36, No. 4, 2000

[32] B. T. Merritt, R. F. Post, G. R. Dreifuerst and D. A. Bender, "Halbach Array Motor/Generator A Novel Generalized Electric Machine", Halbach Festschrift Symposium, 1995.

[33] P. C. Sen, "Principles of Electric Machines and Power Electronics," ***J. Wiley***, 1997.

[34] S. Jang, S. Joeng, D. Ryu and S. Choyi, "Design and Analysis of High Speed Slotless PM Machine with Halbach Array," ***Magnetics***, Vol. 37, No. 4, 2001.

[35] S. M. Hosseini, M. Agha-Mirsalim and M. Mirzaei, "Design, Prototyping, and Analysis of a Low Cost Axial-Flux Coreless Permanent-Magnet Generator," ***IEEE Trans. Magn***, Vol. 44, No. 1, January, 2008.

[36] M. Comanescu, A. Keyhani and M. Dai, "Design and Analysis of 42-V Permanent-Magnet Generator for Automotive Applications," *IEEE Trans. Energy Conversion*, Vol. 18, No. 1, March, 2003.

[37] J. F. Gieras, R. Wang and M. J. Kamper, "Axial Flux Permanent Magnet Brushless Machines," Dordrecht, *Kluwer Academic Publishers*, 2004.

[38] E. Vrancik, "Prediction of Windage Power Loss in Alternators," *NASA*, 1968.

[39] R. Wang and J. Kamper, "Calculation of Eddy Current Loss in Axial Field Permanent Magnet Machine with coreless Stator," *Energy Conversion,* Vol. 19, No. 3, 2000.

[40] G. Swift, T. S. Molinski and W. Lehn, "A Fundamental Approach to Transformer Thermal Modeling—Part I: Theory and Equivalent Circuit," *IEEE Trans. Power Delivery*, Vol. 16, No. 2, April, 2001.

[41] C. C. Chan, "Axial-Field Electrical Machines – Design and Applications." *IEEE Trans. Energy Conversion*, Vol. EC-2, No. 2, pp. 294-300, June, 1987.

[42] J. Braid, A. van Zyl and C. Landy, "Design Analysis and Development of a Multistage Axial Flux Permanent Magnet Synchronous Machine," *IEEE Africon*, pp. 675-680, 2002.

[43] F. Gieras and M. Wing, "Permanent Magnet Motor Technology: Design and Applications," 2nd Edition, New York: Marcel Dekker, 2002.

[44] J. Saari, "Thermal Analysis of High Speed Induction Machines," *PhD thesis*, Helsinki University of Technology, 1998.

[45] D. Meeker, "Finite Element Method Magnetics Users Manual," Version 4.2., September, 2002.

Appendix A

DC/DC Converter Design

The DC-to-DC converter provides the necessary speed control of the machine by regulating the machine terminal voltage, while also ensuring a constant voltage at the consumer end. In this section, various topologies will be presented, whereby the most suitable converter is selected. The selection process attempts to meet the objectives set out at the beginning of the project, i.e. a simple, low cost and rugged topology.

DC-DC Converter Topologies

A buck converter works in such a way that the average output voltage is lower than the input voltage.

The average output voltage is given by (Mohan, 2003):

$$\frac{V_{out}}{V_{in}} = D \qquad \text{(A.1)}$$

Where,

V_{in} – is the input voltage to the converter

V_{out} – is the output voltage from the converter

D – is duty ratio

This topology, as shown in Fig A1, works by varying the ratio of the time that the switch is on to the time that the switch is off (the duty cycle/ratio). The inductor and the capacitor at the output stage act as current and voltage filters respectively. This converter is a linear converter as the output voltage varies linearly with respect to changes in the duty cycle.

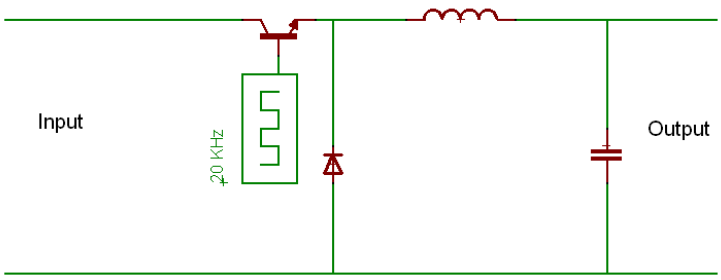

Figure A1: Buck Converter.

This converter topology acts as a fundamental building block in numerous DC-DC converter topologies. The second topology examined is that of a boost converter, as shown in Fig. A2. A boost converter works in such a way that the average output voltage is higher than the average input voltage. When the switch is turned on, the input supplies energy to the inductor as the diode is reverse biased and the output stage is isolated. When the switch is turned off, the energy stored in the inductor flows to the output stage. Additionally energy flows from the input stage to the output stage. This energy stored in the inductor boosts the output voltage above the input voltage.

The average output voltage is given by (Mohan,2003):

$$\frac{V_{out}}{V_{in}} = \frac{1}{1-D} \qquad \text{(A.2)}$$

Where,

V_{in} – is the input voltage to the converter

V_{out} – is the output voltage from the converter

D – is duty ratio

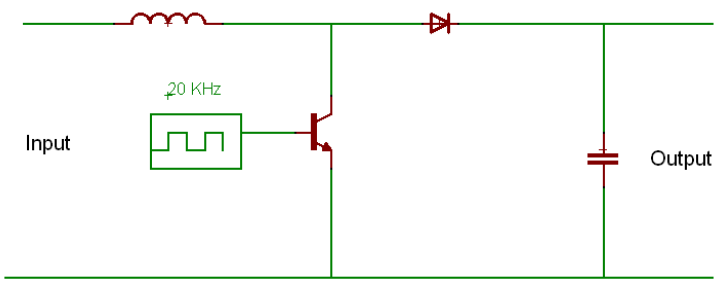

Figure A2: Boost Converter.

The ideal gain of 1/(1-D) is not realizable as the duty ratio gets close to 1. This is because of the parasitic losses associated with the inductor, the capacitor and the diode. These losses put an upper bound on the step up ratio that a boost stage can achieve. This drop off in the available gain is shown in Fig. A3.

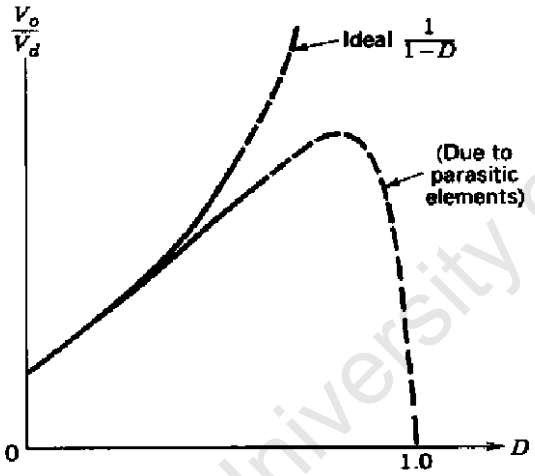

Figure A3: Voltage gain curve for boost converter.

The third topology is a combination of the buck and boost converter, known as a buck-boost converter. There are numerous circuit configurations available in the literature for the buck-boost converter topology. A number of these converters are analysed below.

The tapped inductor converter is one which uses a tapped inductor (auto transformer) to increase the input to output gain ratios. The proposed converter is shown in Fig. A4. The converter is both bi-directional and can either buck or boost the input voltage depending on the requirements. The

advantage of this configuration is that it only consists of 2 switching devices, resulting in fewer components and a simplified control circuit.

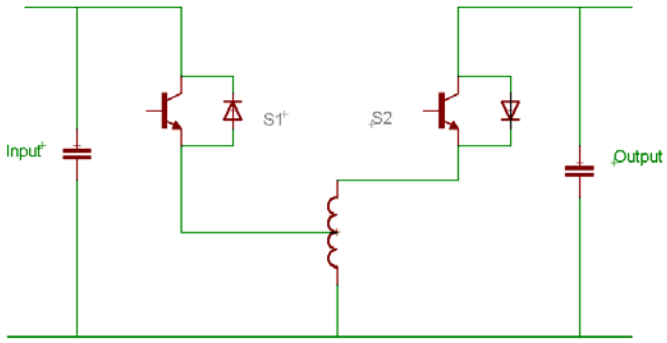

Figure A4: Tapped inductor converter.

The voltage transfer ratio for the tapped inductor converter is given by the following equation:

$$M = \frac{U_2}{U_1} = \frac{D.n}{(1-D)} \qquad \text{(A.3)}$$

$$n = \frac{N_1 + N_2}{N_2} \qquad \text{(A.4)}$$

Where:

N_1 and N_2 are the number of windings on the first half and second half of the tapped inductor respectively.

Fig. A5 shows how the gain achievable by the converter. The gain may be varied by changing the value of n, the ratio of turns on the tapped inductor.

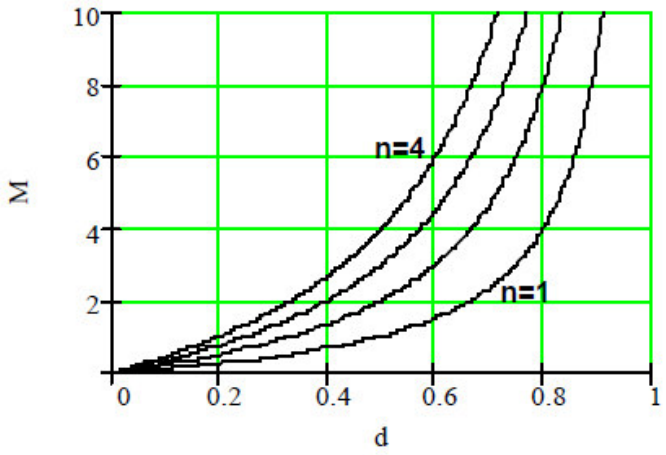

Figure A5: Voltage gain curves for tapped inductor converter.

This converter is controlled by varying both the switching frequency and the duty cycle of switches. The frequency is varied to prevent an oscillation of energy between the two sides of the converter at low loads. The two switches are driven in push-pull mode.

The following converter topology is based on the buck and boost converter topologies, as discussed earlier. It consists of two synchronous converters in tandem sharing a single inductor. The converter is designed to use four switches to allow bi-directional power flow and the ability to operate in both buck and boost modes. The design schematic is shown in Fig. A6. The various states of the switches required for the converter to operate in the four different modes of operation are shown in Table A1.

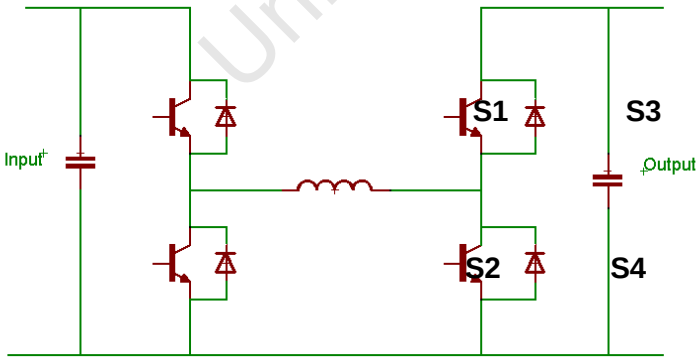

Figure A6: Bidirectional synchronous buck-boost converter.

Table A1: Various switch states for operation of the synchronous converter in the four different modes of operation

Power flow direction	Mode of operation	S1	S2	S3	S4
Left to right	Step Up	ON	OFF	OFF	SW
Left to right	Step Down	SW	OFF	OFF	OFF
Right to left	Step Up	OFF	SW	ON	OFF
Right to left	Step Down	OFF	OFF	SW	OFF

An addition to the above synchronous converter is suggested by (Freepatentsonline, 2008), as shown in Fig.7.8. Across each diode and switch, a resonant capacitor is placed which enables soft switching of the switching devices. This soft switching could result in the reduction of switching losses in the converter by thirty percent. A thorough analysis of the operation of the converter topology in Fig. A7 is presented by (Freepatentsonline, 2008) and will not be repeated here.

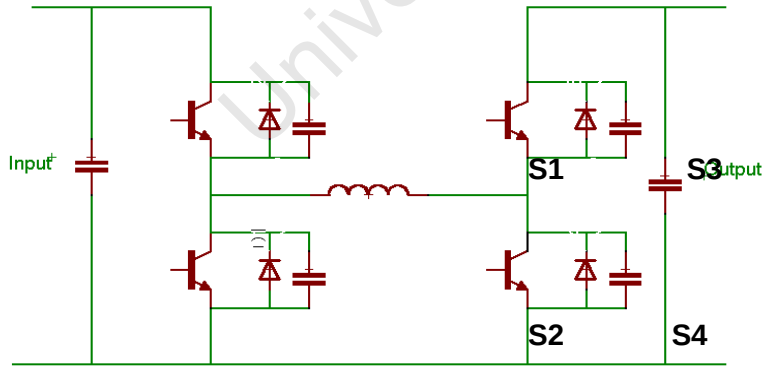

Figure A7: Bidirectional synchronous DC-DC converter with resonant capacitors.

Sizing of components

For the sizing of the components, the buck and boost stages were sized separately, after which these are combined for the bi-directional buck-boost converter. The design of the boost component of the converter will now be discussed.

The maximum boosting required is stepping up the input voltage by 3 times. This will occur when the motor is accelerating up to its maximum operating speed of 24 000rpm. At this speed the back EMF is approximately 34V and therefore the applied voltage will need to be 36V. The minimum voltage required is 12V. Therefore if the converter is to be kept in the continuous region, the range of duty cycle required is from 0% to 66%.

From (Mohan, 2003) and (Kilgenstein, 1989) the following equations were used to determine the inductance and capacitance required:

$$L = 0.074\frac{T_{s\times} \times V_o}{I_o} \qquad \text{(A.5)}$$

$$C = \frac{I_{om} \times D \times T_s}{\Delta V_o} \qquad \text{(A.6)}$$

Where,

L – is the inductance (H)

T_s – is the switching period (s)

V_o – is the output voltage (V)

I_o – is the minimum output current (A)

C – is the capacitance (F)

I_{om} – is the maximum output current (A)

D – is the duty Cycle

ΔV_o – is the percentage voltage ripple

The specifications of the boost converter and its component sizes are summarised in Table A2.

Table A2: Boost converter specifications and component sizes

	Value
T_s	1/f=0.00005s
V_o	36V
D	0.66
ΔV_0	0.05
I_o	1A
I_{om}	10A
L	0.1mH
C	7mF

The maximum bucking required for generator mode of operation is 3:1. This will occur when the flywheel is at its maximum speed and the back EMF is 36V. The minimum bucking that the converter will be required to perform is when the flywheel is spinning at 8000RPM and the back EMF is 12V. At this time no bucking will be required from the converter. Therefore if the converter is kept in the continuous conduction region the range of duty cycles required is from 33% to 100%. From (Kilgenstein, 1989), the components of the buck converter can be selected as follows:

$$L \geq \frac{(1 - D_{\min})V_o}{\Delta I_L f} \qquad \text{(A.7)}$$

$$C_o = \frac{\Delta I_L}{\Delta V_o \times 8 \times f} \qquad \text{(A.8)}$$

Where,

L – is the inductance (H)

V_o – is the output voltage (V)

D_{min} – is the minimum duty cycle

ΔI_L – is the inductor current ripple (A)

f – is the switching frequency (Hz)

C_o – is the output capacitance (F)

ΔV_o – is the output voltage ripple (V)

The specifications of the buck converter and its component sizes are summarised in Table A3.

Table A3: Buck converter specifications and component sizes

Parameter	Value
V_o	12V
D_{min}	0.33
ΔI_L	2A
f	20 000Hz
ΔV_o	5%
L	0.2mH
C	19uF

The component sizes for the two converters were of a similar nature. The larger of the two options were chosen in each case to enable the converter to buck and boost effectively. The inductor was over-rated to ensure that the output current is as smooth as possible to prevent torque pulsations in the motor. The final component sizes are as follows:

Input capacitance: 7mF

Output capacitance: 7mF

Inductor size: 0.4mH

The inductor was designed from first principles. The core used was the Ferroxcube E 55/28/21 core with grade 3C90 material. This core was used due to its availability.

The starting point in inductor design is the product: $I_{L\max}^2 \times L$. This is used to determine the core size and the corresponding relative permeability. This is done using the DC magnetisation curve.

$I_{L\max} = 10A$ (the maximum rated motor current), L=0.4mH

$I_{L\max}^2 \times L = 40A^2 mH$

From the magnetisation curve, μ_e is found to be ≈33. Using the following formula from (Kilgenstein, 1989) and the data from the Feroxcube data sheet:

$$A_L = (H)\frac{\mu_e \mu_o}{l/A} \qquad \text{(A.9)}$$

Where:

A_L – is the inductance rating

μ_e – is the relative permeability of the magnetic core

μ_o – is the permeability of free space = $4\pi \times 10^{-7}$ H/m

l/A – is the core factor

A_L was found to be 119nH.

From the Feroxcube data sheet the airgap required was found to be 5mm. Finally the number of turns required was found to be 58 turns using the formula below from (Kilgenstein, 1989):

$$\text{Required turns} = \left[\frac{DesiredL(nH)}{A_L\left(\frac{nH}{N^2}\right)} \right]^{1/2} \qquad \text{(A.10)}$$

The size of the wire used was as large as possible, to limit the resistance of the inductor, while still allowing the correct number of turns to fit on the core. The wire size chosen was copper wire with a diameter of 0.315mm

The converter was controlled using PWM control. The switching frequency was 20kHz.

The driver circuit used to switch the Mosfets is shown in Fig. A8. The input driver signals are sourced from a dSpace controller card. All control is performed by the controller card, which allows for rapid control prototyping. The MOSFETs were mounted on a heat sink to dissipate the heat generated.

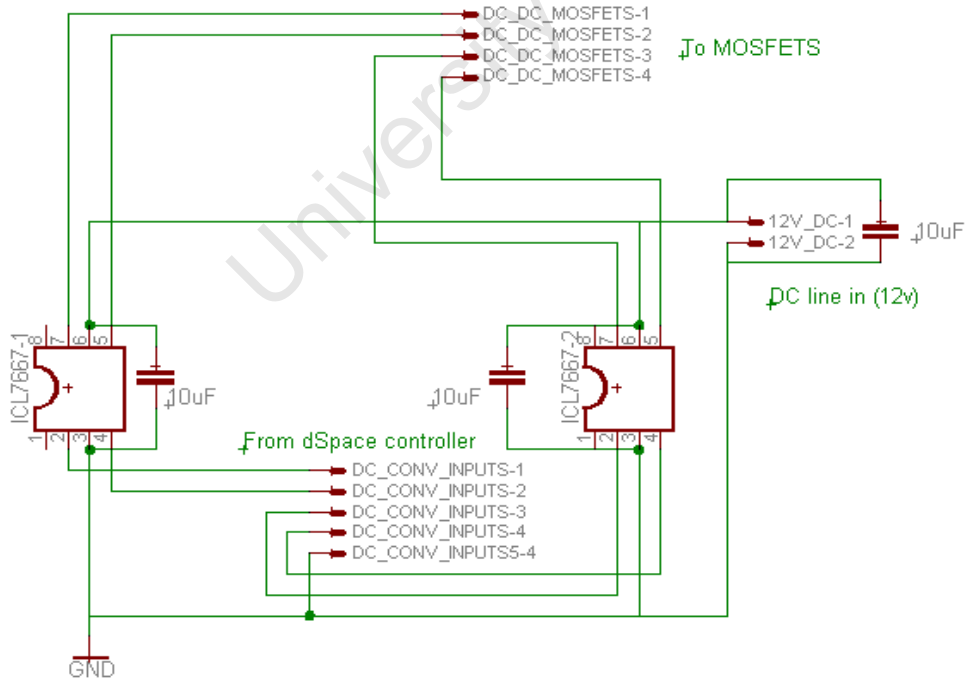

Figure A8: MOSFET driver circuit for DC-DC converter.

Commutation

Due to the lack of brushes, commutation cannot occur naturally but forced commutation is required. This commutation is controlled by electronics. The purpose of the commutation strategy is to ensure the commutation of the stator windings corresponds to the correct position of the rotor. In order for this to occur, the controller needs to know the position of the rotor. However a precise determination of the rotor position is not necessary, as it is only required that the position of the rotor is known at the commutation points (Dixon, 2002). Two methods for detecting the rotor position will be presented and discussed below.

To control the stator windings for commutation, an inverter consisting of 3 half bridges is used. Fig. A9 shows the standard schematic of a BLDC inverter.

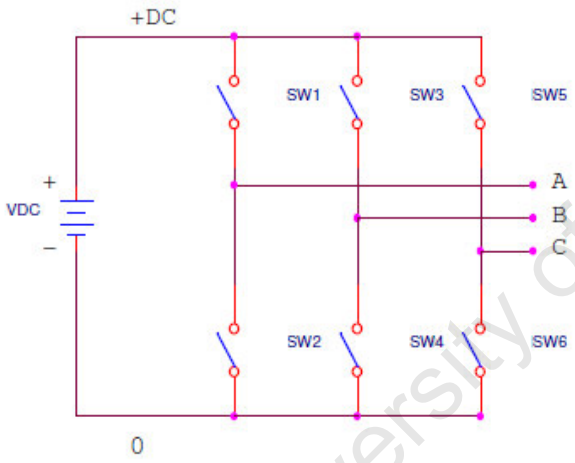

Figure A9: BLDC Inverter.

In order to control the motor, only two of the windings are supplied at any one time. This is achieved by connecting the terminal of one phase to the positive terminal of the supply and one end of another phase to the negative terminal. This switching strategy results in currents of a trapezoidal shape flowing through the stator windings.

The table below gives the switches that are required to be on for each of the 6 possible commutation segments.

Table A4: Switch Commutation for CW Rotation

Hall Sensors value (CBA)	Phase	Switches
101	A-B	SW1;SW4
001	A-C	SW1;SW6
011	B-C	SW3;SW6
010	B-A	SW3;SW2
110	C-A	SW5;SW2
100	C-B	SW5;SW4

If the number of magnetic poles on the rotor is increased, the commutation strategy does not change (Dixon, 2002), however the conversion between electrical and mechanical revolutions would need to be compensated for.

Rotor Position Measurement Using Hall Sensors

Three Hall-effect sensors are placed 120 degrees apart within the stator. With the sensors placed in these positions, there are six different possible outputs from the sensors. With every change in hall sensor output, commutation occurs.

The advantages of using Hall sensors to determine the position of the rotor are:

- Simplified signal processing as the hall sensor output is not greatly affected by electrical noise.
- Simplified signal processing as commutation sequence is easily obtained from Hall sensor outputs.

The disadvantages of using Hall sensors to determine the position of the rotor are:

- Increased cost of machine
- Rotor Position Using Back EMF Sensing

The direct Back-EMF method of sensorless position determination is the most popular method used (Siostrzonek, 2006). This method involves sensing the back EMF in the phase that is not being fed by the motor inverter. The instant of commutation is reached when the slope of the back EMF changes from a positive or negative value to zero (Dixon, 2002), as shown in Fig. A10.

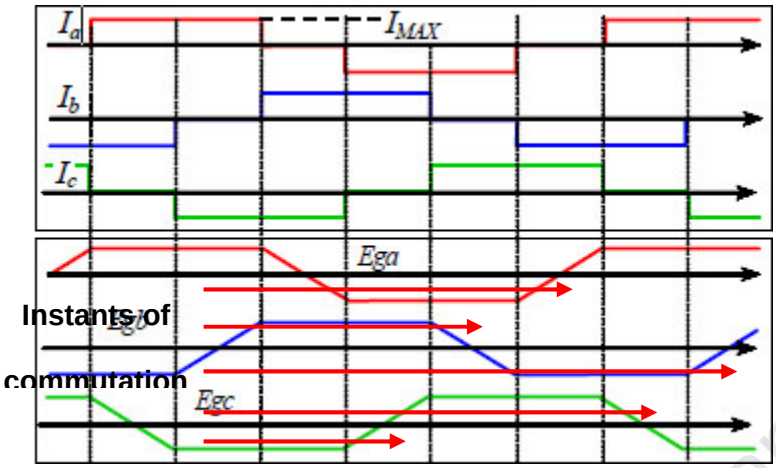

Figure A10: Current waveforms and phase to neutral voltages.

The problem of sensing these commutation points is made extremely difficult due to the large amount of electrical noise that is present at any stage (Dixon, 2002). Significant processing power or additional circuitry is required to filter out this noise so that a clear reading of the back EMF can be obtained.

A significant disadvantage of the sensorless approach to driving a BLDC motor is the complicated start up procedure required (Dixon, 2002). A start up procedure is required since the rotor is is at standstill, therefore no back EMF is present. This makes estimation of the rotor position from the back EMF impossible at start up. The following start up procedure is proposed by H.C. Chen and C.M Liaw in (Chen, 2002):

Step 1:

The rotor is aligned with a specific phase by applying a constant current to two of the stator phases.

Step 2:

The BLDC motor is started as a synchronous motor fed by a six phase inverter. With correct current control and the correct ramping of the applied frequency, the motor will smoothly and stably speed up.

Step 3:

Once the speed of the rotor is sufficient to generate back EMF's that can measured for sensorless operation of the machine, the machine is switched over into sensorless mode of operation.

Therefore, sensorless rotor position sensing has the following advantages:

- Low cost due to no need for external device to measure rotor position
- High reliability due to lack of external components

And the following disadvantages:

- Complex signal processing needed to determine commutation instants
- Noise reduction techniques must be employed to filter voltage signal
- Separate start up procedure required

For this high speed application, the hall sensors provide a more reliable and simplistic means of rotor position detection, therefore these were selected.